MAGNETIC SUSCEPTIBILITY OBSERVATION OF A SPIN-REORIENTATION TRANSITION IN Fe/2 ML Ni(111)/W(110) FILMS

By

C. S. ARNOLD, M.Sc.

A Thesis

Submitted to the School of Graduate Studies

in Partial Fulfilment of the Requirements

for the Degree

Doctor of Philosophy

McMaster University

OBSERVATION OF A SPIN-REORIENTATION TRANSITION

DOCTOR OF PHILOSOPHY (1997)
(Physics)

McMaster University
Hamilton, Ontario

TITLE: Magnetic susceptibility observation of a spin-reorientation transition in Fe/2 ML Ni(111)/W(110) FILMS

AUTHOR: C. S. Arnold, M.Sc. (Dalhousie University)

SUPERVISOR: Professor D. Venus

NUMBER OF PAGES: viii, 182

ABSTRACT

One of the most important topics in ultrathin film magnetism is perpendicular ferromagnetism, in which the orientation of the film magnetization is perpendicular to the film plane. A perpendicular orientation is surprising because of the very strong dipolar field produced by the film as a whole which prefers that the film moment be in-plane. In the limit of atomic thicknesses, magnetic anisotropies are occasionally strong enough to overcome the dipolar field and establish a perpendicular orientation of the moment. In such films, the moment exhibits a *spin-reorientation transition*, reorienting from perpendicular to in-plane with increasing coverage or temperature. Another phenomenon associated with a perpendicular preference is a disintegration of the film into domain structures that are expected to closely resemble liquid crystals. Ultrathin fcc Fe, grown on a 2 atomic layer fcc Ni(111) buffer, is ferromagnetic and exhibits the spin-reorientation transition. Through refinements of an existing technique, the surface magneto-optical Kerr effect (SMOKE), extremely high resolution magnetic susceptibility measurements were made of this system. The magnitudes and temperature-dependencies of the experimental susceptibilities are found to be consistent with theories of the domain structure. A temperature-coverage phase diagram is constructed and reveals structure closer the multicritical point of the transition, where reorientation and order-disorder boundaries meet, than in any previous experimental study. In that part of the phase diagram where the transition to disorder proceeds directly from the perpendicularly magnetized state, no evidence of a Curie temperature is observed.

ACKNOWLEDGMENTS

Many people contributed to my work in a variety of ways and I wish to express my sincere appreciation to them. My supervisor, David Venus, provided energetic, conscientious, and very competent guidance throughout my stay at McMaster. I have him to thank for maintaining the quality in this thesis. The standing members of my committee, Bruce Gaulin and John Preston, offered useful advice which I have tried to incorporate into this thesis. I also benefitted tremendously from sharing the lab with Hamish Johnston. We learned the fine arts of MBE and UHV technology together and it was he who first encouraged me to look at the Fe/Ni system. Stephen Cool and Mike Dunlavy were also very helpful. Our group technician, Marek Kiela, was absolutely invaluable. Without his work, our work would grind to a standstill. Although I depended on many of the excellent resources at McMaster, Adam Hitchcock's group and his research assistant Tolec Tylisczak were especially helpful, as was Venice Perno in the student machine shop, Evert Cairns, and the entire administrative and secretarial staff, who run a very tight ship. Outside McMaster, I had important conversations with Jeff Anderson, Keith De'Bell and Bret Heinrich. I received scholarships and bursaries from NSERC, the OGS program, McMaster University and the Anglican Church Diocese of Nova Scotia. The computer on which this thesis was prepared, and on which all of the analysis was done, was donated by my father (in-law) R. K. Bhatnagar of ABM computers, Halifax. Our very nice apartment in Stoney Creek, which has provided very happy living, was also provided by our parents Rajendra and Gopi Bhatnagar. Our friends and family were supportive and understanding throughout my education. I especially wish to thank my kind and loving parents Fev and Joyce Arnold, who always supported my interests (providing the equipment for my first laboratories!), and my parents-by-marriage Rajendra and Gopi Bhatnagar, who were instrumental in both of my graduate degrees. My greatest debt is owed to my wife Anjali, who has sacrificed much, supported me in all possible ways, and who is an excellent second-supervisor. I dedicate my thesis *To Anjali*, who deserves this credit and more.

TABLE OF CONTENTS

LIST OF ACRONYMS AND ABBREVIATIONS

Å	Angstrom (10^{-10} m)
AES	Auger Electron Spectroscopy
AFM	Antiferromagnet
ARAES	Angle-Resolved AES
bcc	body-centered cubic
CP	Close Packed
fcc	face-centered cubic
FWHM	Full-Width Half-Maximum
FV	Franck-Van der Merwe (growth mode)
hcp	hexagonal close-packed
HWHM	Half-Width Half-Maximum
IMFP	Inelastic Mean-Free-Path
LEED	Low Energy Electron Diffraction
MBE	Molecular Beam Epitaxy
ML	monolayer
PM	Paramagnetic
PMA	Perpendicular Magnetic Anisotropy
PS	Pseudomorphic
RHEED	Reflection High Energy Electron Diffraction
RT	Room Temperature
SK	Stranskii - Krastonov (growth mode)
SMOKE	Surface Magneto-Optic Kerr Effect
S/N	Signal-to-Noise Ratio
STM	Scanning Tunneling Microscopy
TPD	Thermally Programmed Desorption
UHV	Ultra-High Vacuum
VW	Volmer-Weber (growth mode)
3-D	three-dimensional
3d	atomic orbital notation

1. INTRODUCTION

Magnetism in materials like Fe is a very old subject. A non-physicist would probably be surprised to learn that much more is to be learned about this field of condensed matter physics. Progress in magnetism has been slow, primarily because the subject is complicated. The magnetic field is an intrinsically relativistic quantity, related to the electric field through Maxwell's equations or equivalently, through the Lorentz transformations. Magnetic sources in materials are electrons, whose magnetic moments arise through quantum-mechanical spin. The theoretical problem is therefore a many-body, quantum-relativistic one, further complicated for the 3d transition metals like Fe where the magnetic electrons are conduction electrons free to move in the sample. Over the years many useful, simplifying approximations have provided considerable insight to magnetism in these materials, but the first-principles, finite temperature calculation of the magnetic state of Fe remains an unsolved problem.

In recent years, considerable progress in the field has resulted from two developments. The growth of computing power has permitted simulations and calculations that are fair approximations of real systems. On the experimental side, improvements in ultra high vacuum technology, and the development of molecular beam epitaxy have permitted the engineering of *ultrathin magnetic films*, mostly of Fe, Co or Ni. Ultrathin films are typically a few to several atoms in thickness. Studying ultrathin films, rather than bulk magnets, is advantageous primarily because of the ability to fabricate metastable materials. These materials do not occur naturally and have not been

possible to prepare in bulk materials. In this way, the experimentalist can tailor magnetic structures to test the predictions of theorists. Ultrathin films are, however, different from thicker films or bulk samples in a few important ways. These differences lead to phenomena that are specific to ultrathin films and engineered, layered materials. A few important ultrathin film phenomena are *giant magnetoresistance* and *oscillatory exchange coupling*.

One major difference between thin films and ultrathin films is the spatial dimensionality. At film thicknesses of a few atoms or less, the magnetic properties of the film cannot change over the thickness of the film, due to a strong local interaction that locks together the magnetic moments comprising the film. Thus, magnetic ultrathin films are two-dimensional. The thermodynamic properties of two-dimensional magnets are very different from three-dimensional ones. Before growing such thin films was possible, many speculated that they could only be magnetic at very low temperatures. The predictions were based on a famous result most often attributed to Mermin and Wagner. Their theorem proves that two-dimensional, isotropic magnets can only have non-zero magnetization at absolute zero. Isotropic magnets have no orientational preference of their magnetization. A corollary, however, is that very weak anisotropic interactions involving the moments stabilize magnetism at finite temperatures. All such interactions that have orientational preference are called *magnetic anisotropies*.

Luckily, another factor that is characteristic of ultrathin films is strong *perpendicular magnetic anisotropy*, meaning an increased preference of the magnetization to lie in the plane or perpendicular to it. In cubic materials, the increase occurs because of a reduction of symmetry from cubic at an interface or surface. In thin (rather than ultrathin) films, the magnetization always lies in the plane because of the interaction of the

magnetization with the field it generates. This field is called the *dipolar* or *demagnetization* field, although the two terms have slightly different meanings. In ultrathin films the magnetic anisotropy may overcome the interaction of the magnetization with the dipolar field, producing perpendicular magnetization. The existence of ultrathin magnets with their magnetization perpendicular to the film is important physically and technologically.

The nature of the magnetized state is very different for perpendicularly magnetized films than for in-plane films. Many films with in-plane magnetization posses the properties of simple, idealized models. Magnetic properties in perpendicular magnets are profoundly influenced by the dipolar field, favoring, for example, a fragmentation of the film into small domains with alternating orientations of the moments up and down.

A very interesting situation arises if the perpendicular magnetic anisotropy favors the magnetization out-of-plane and is about as strong as the dipolar field. If the anisotropy is stronger than the dipolar interaction, then the moment is perpendicular. If the dipolar interaction is stronger, then the moment is in-plane. At the point of precise compensation the film is nearly isotropic. By varying the film thickness (or temperature) the relative strengths of the two terms can be varied, resulting in a change in orientation of the magnetization. This phenomenon is called the *spin-reorientation transition* and its investigation is the principal theme of this thesis.

The experiments reported in this thesis are a natural and necessary extension of previous studies of the spin-reorientation transition. Previous investigations of the phenomena relied on measurements of the static magnetization. These revealed a domain structure resulting in a net magnetization of zero as the compensation point is approached from the perpendicular phase. Theory predicts that the domain structure should be very

sensitive to an applied field. Magnetic susceptibility measurements, which probe the linear response of a magnet to an applied field, are therefore an ideal technique to study the domain structure. For the first time, these experiments examine the portion of the spin-reorientation phase diagram closest to the transition. This allows an investigation of some theoretical predictions regarding the topology of the temperature-thickness phase diagram. The study includes, also for the first time, measurements very near the multicritical point of the system, where the reorientation boundary meets the order/disorder boundary. Another important result is that the loss of magnetic order, when it proceeds directly from the perpendicular phase without reorientation, is fundamentally different than for in-plane magnets.

The organization of the thesis is as follows. Chapter 2 contains an introduction to the basic concepts in magnetism with a special emphasis on magnetism in the 3d transition metals. Ultrathin film magnetism is described in more detail than above and the literature regarding the spin-reorientation transition is reviewed. Experimental methods are described in chapter 3 in two main sections reflecting the parallel efforts required in experimental ultrathin film magnetism. Surface science and the technologies employed in the sample growth and structural determination are outlined in the first section. Magnetic measurements were made with the surface magneto-optic Kerr effect (SMOKE). It is described in the second part together with innovations that dramatically increase its sensitivity. SMOKE susceptibility measurement is a new and extremely sensitive technique. It is described with an emphasis on how noise levels are minimized. Finally, the observation of a spin-reorientation transition is presented and discussed in chapter 4 and the main conclusions are summarized in chapter 5.

2. THE SPIN-REORIENTATION TRANSITION

2.1 Basic concepts in magnetism

2.1.1 Magnetic fields and magnetic moments

Magnetic fields interact with electric charges in two ways. The Lorentz force describes the force $\underline{F}$ on a charge q moving with velocity $\underline{v}$ through a magnetic field $\underline{B}$.

$$\underline{F} = q\,\underline{v} \times \underline{B}\,. \tag{2.1}$$

A time-varying field also interacts with electric charges through Faraday's law of induction which relates the time rate-of-change of $\underline{B}$ to the electric field

$$\nabla \times \underline{E} = \partial \underline{B}/\partial t\,, \tag{2.2}$$

and the charge experiences a force $\underline{F} = q\,\underline{E}$.

Magnetic fields themselves originate from the movement of charge or, on macroscopic scales, from the flow of electric currents. A natural starting point for a description of magnetic materials is the description of current loops and magnetic dipoles. Equation (2.3) gives the magnetic field $\underline{B}$ generated at a point $\underline{r}$, θ by a circular current loop with area A and current I.

$$\underline{B}(r, \theta) = \frac{\mu_o I A\,(2\cos(\theta)\,\hat{r} - \sin(\theta)\,\hat{\theta})}{4\pi r^3} \tag{2.3}$$

The origin of the (spherical) coordinate system coincides with the center of the loop and $\pi r^2 >> A$. Fig. 2.1 is a sketch of the field produced by a current loop.

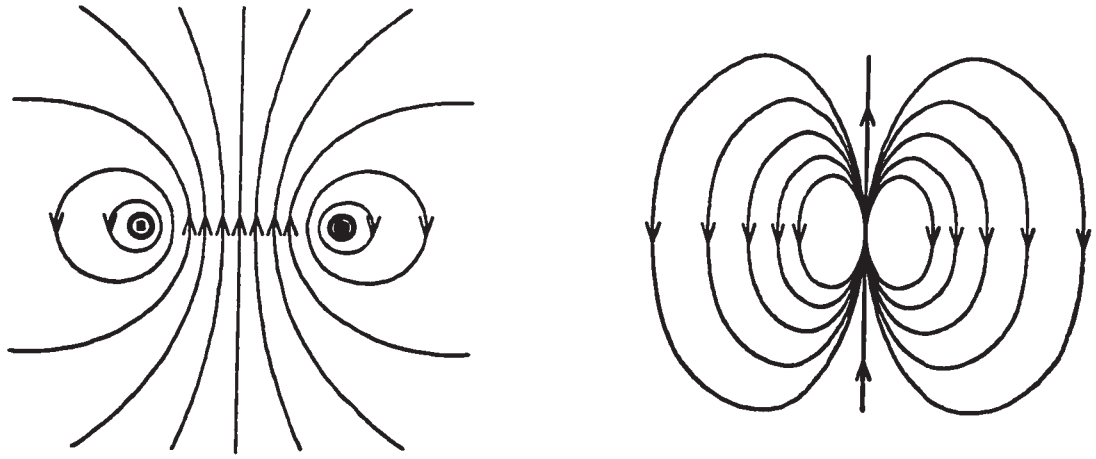

Fig. 2.1 - The magnetic field of a current loop in cross-section approaches that of a magnetic dipole in the far field, although it differs near the loop.

Identifying the magnetic dipole moment

$$\underline{m} = IA\,\hat{n} \tag{2.4}$$

where $\hat{n}$ is the unit normal to the loop, equation (2.3) is rewritten

$$\underline{B} = \frac{\mu_o (3\underline{r}(\underline{m}\cdot\underline{r}) - r^2\underline{m})}{4\pi r^5} \tag{2.5}$$

Returning to microscopic scales by reducing the number of electrons in the loop until only one electron with charge $-e$ and mass m_e remains, (2.4) rewritten in terms of the orbital angular momentum $\underline{L}$ of the electron is

$$\underline{m} = \frac{-e\,\underline{L}}{2m_e} \tag{2.6}$$

Electrons also have a spin with angular momentum $\hbar/2$. Including a relativistic correction $g \approx 2$, the gyromagnetic ratio, the spin part of the angular momentum is

$$\underline{m} = g \frac{-e\underline{S}}{2m_e} \tag{2.7}$$

With the definition $\mu_B = e\hbar/2m_e$, $m_s \approx \pm\mu_B$. The numerical value is $\mu_B = 0.93 \times 10^{-23}$ A·m^2

An isolated atom has electronic levels with quantized angular momentum states {s, p, d ...}. The total magnetic moment $\underline{J} = \underline{L} + \underline{S}$ is then a sum over all atomic electrons of the spin and orbital angular momenta. In the case of the 3d transition metal solids Fe, Co, and Ni, the 3d levels contain conduction electrons and have significant interatomic overlap. The resultant splitting of the 3d level has the effect of reducing or *quenching* the orbital part. To a good approximation then, $\underline{J} \approx \underline{S}$ in the 3d transition metal solids. Although $\underline{L}$ is dramatically reduced, it is not completely eradicated, and spin-orbit coupling effects are important, as will be discussed later in relation to magnetic anisotropies and magneto-optics. Calculated and measured values of S and $L_{||}$ (parallel to S) are presented in table 2.1. For comparison, the rare earth ion Gd^{3+}, whose f-shell ($4f^7$) contributes, has a total J of approximately $8\mu_B$.

	Experimental S	L	Calculated S	L
Fe	2.13	0.09	2.16	0.048
Co	1.59	0.16	1.57	0.079
Ni	0.56	0.05	0.60	0.051

Table 2.1 Experimental and theoretical values of S and L were obtained from reference 1 for bulk materials. Values are quoted in units of Bohr magnetons μ_B.

In an applied magnetic field, a magnetic moment experiences a torque which tends to align it with the field. Connecting with the concept of the current loop, this torque arises from the Lorentz force (2.1) on the moving charges in the loop. The magnetostatic energy of a moment $\underline{m}$ in a magnetic field $\underline{B}$ is

$$E = -\underline{m} \cdot \underline{B} , \tag{2.8}$$

Thus, using (2.8) and (2.5) the energy of interaction between two dipoles is obtained. This is the dipole-dipole interaction.

2.1.2 The macroscopic magnetization and the magnetic susceptibility

The macroscopic magnetization is a material property, defined as the net magnetic moment per unit volume

$$\underline{M} = \frac{1}{V}\sum_{i=1}^{N} \underline{m}_i \quad , \tag{2.9}$$

where a representative volume V contains N moments m_i. If all the moments are equivalent and aligned, as in the case of a single domain in a ferromagnet at T = 0, the sum is just $\underline{M} = N\underline{m}/V$. If the moments are randomly oriented, $\underline{M}$ may be zero. The magnetic field $\underline{B}$ is given by

$$\underline{B} = \mu_o (\underline{H} + \underline{M}) , \tag{2.10}$$

where $\mu_o = 4\pi \times 10^{-7}$ is the permeability of free space and the field $\underline{H}$ is related to the free current in a current loop C by Ampère's circuit law

$$\oint_C \underline{H} \cdot d\underline{l} = I_{free} \tag{2.11}$$

A common misconception is that Eq. (2.10) separates B into an H-field due to currents, and a magnetization M due to microscopic moments. While this is often a useful working understanding, H also contains contributions from the spatial distribution of M. In a uniformly magnetized object, these correspond to the boundary conditions.

The magnetic susceptibility χ measures the linear magnetization response $\delta\underline{M}$ to a small applied field $\delta\underline{H}$. Since $\underline{M}$ and $\underline{H}$ are both vectors, χ is necessarily a tensor property. The relationship which defines χ is therefore

$$\delta M_i = \chi_{ij}\, \delta H_j \quad \text{or} \qquad \chi_{ij} = \frac{\partial M_i}{\partial H_j} \quad . \tag{2.12}$$

Most often $\delta\underline{M}$ and $\delta\underline{H}$ are parallel so that only the diagonal elements of χ are measured. For convenience then, a single subscript is employed to refer to the elements of χ in all that follows. The measurement of χ is described in chapter 3 in more detail.

2.1.3 Magnetic interactions and ordering

A central problem of magnetism is *magnetic ordering*. This phrase refers to the spatial arrangement of the moments in a material which can, for example lead to a non-zero M. Magnetic ordering is dependent on a number of mechanisms. One aspect of the arrangement is the relative orientation of neighboring moments. In a metal, the short ranged interaction responsible for this is the *exchange interaction* and is much stronger than the dipole-dipole interaction between the moments. This interaction is due to electron-electron *electrostatic* interactions modified by Pauli exclusion, rather than magnetostatic interactions. Electrons of adjacent atoms interact via their electric fields.

Pauli exclusion imposes constraints on the spatial and spin parts of the wavefunction so that the total wavefunction is antisymmetric under the exchange of any two electrons. By flipping the spin of one electron, the spatial part necessarily changes. The electrostatic interaction between two electrons is sensitive to this spatial arrangement, resulting in a difference in energy dependent only on the relative orientation of the spins. The interaction between two atomic moments is expressed as

$$E_{ex} = J\underline{s}_1 \cdot \underline{s}_2 , \tag{2.13}$$

where J is the exchange constant and $\underline{s}_1$ and $\underline{s}_2$ are the atomic spins. J may be positive, favoring antiparallel alignment of the moments, or negative, favouring a parallel alignment. A typical exchange energy between nearest neighbors is 10meV. A lattice of spins with negative nearest-neighbor exchange, will tend to align as the temperature is lowered. The state in which there is a net alignment of the moments, leading to a nonzero sum for $\underline{M}$ in (2.8), is known as *ferromagnetic*.

Another aspect of magnetic ordering is the set of directions that the atomic moments are constrained to lie along. These directions are determined by the magnetic anisotropy, whose origins are in spin-orbit coupling. This is the magnetic dipole-dipole interaction between the atomic spin and orbital angular momenta. Although spin-orbit coupling is a much weaker interaction than the exchange interaction, especially since $\underline{L}$ is often partially quenched, exchange does not play a role in the relative orientation of $\underline{S}$ and $\underline{L}$. Because the crystalline environment is anisotropic, some orientations of $\underline{L}$ are favored over others. An axis which is favored by magnetic anisotropy, is termed an *easy axis*, while an unfavoured axis is called a *hard axis*. Typical fields required to pull a moment

from an easy axis to a hard axis are of the order of 0.1 Tesla (a moderately big field) in a 3d transition metal ferromagnet.

Arrangements of magnetic moments on a lattice are usually modeled by treating the effective exchange interactions between adjacent moments. A general Hamiltonian for a lattice of spins with nearest-neighbor exchange J in an applied field $\underline{h}$ is

$$H = \sum_{<ij>} J s_i \cdot s_j + \sum_i h \cdot s_i \qquad (2.14)$$

where the double sum is over nearest-neighbor pairs $<ij>$. Imposing no further restrictions, 2.12 is the isotropic Hamiltonian of the *Heisenberg model.* The effect of strong magnetic anisotropies is included by restricting the possible orientations of the local moments. Constraining the moment to a plane, the *planar* or *XY model* is obtained. Now constraining the moment to a line, with the two possible values of +/- m for the local moment, eq. (2.12) is the famous *Ising* Hamiltonian. The generalization of the Ising model to p distinct moment directions is known as the p-state Potts model. Fig. 2.2

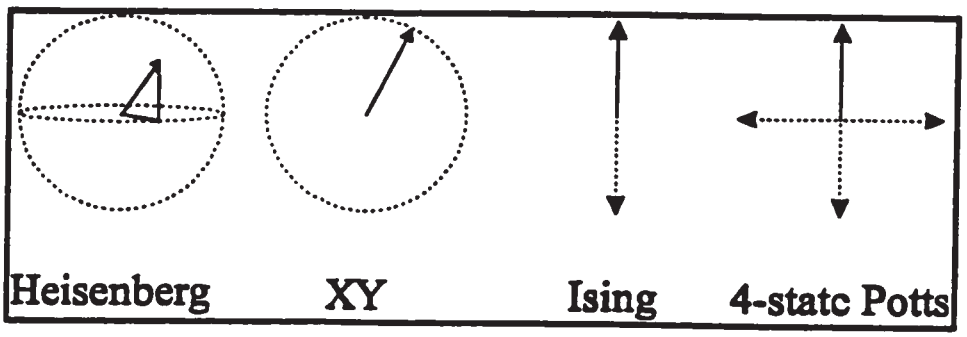

Fig. 2.2 - The exchange interaction of eq. (2.12) is usually considered with constraints imposed on the possible orientations of the moments. In real systems, the magnetic anisotropy plays this role.

summarizes the possible orientations of the local moment in these models. These models are cornerstones of the physics of magnetic systems. Obviously, a negative J produces a ferromagnetic ground state in all of these models. A positive J produces an antiferromagnetic ground state in most cases.

Magnetic order at finite temperatures is investigated (theoretically) by enumerating the excited states of a magnetic lattice, subject to constraints like the ones discussed above, and employing statistical mechanics to distribute the energy among the modes. The various models described above do not exhibit the same finite temperature behavior. Within a given magnetic model, spatial dimensionality also plays a role. A linear chain of spins is 1D, a plane of spins is 2D and a cube is 3D. Fluctuations prevent long range order at any finite temperature in the 2-D Heisenberg model, a result famous as the *Mermin-Wagner theorem.*[2] In 1-D, the Ising model is similarly disordered at finite temperatures. Also in 2-D, the XY model exhibits the *Kosterlitz-Thouless* transition, in which spin vortices produce $M = 0$ in an infinite system. 2-D Ising systems, which are common in ultrathin magnetic films due to strong uniaxial anisotropies,[3] do exhibit ferromagnetic order at finite temperature, below a temperature known as the Curie temperature T_C, $M > 0$. Above this temperature, the lattice is disordered and *paramagnetic*, which means that M is proportional to an applied field. The transition between ferromagnetic and paramagnetic states is a continuous or second-order phase transition. In all that follows, this transition will simply be referred to as the *order-disorder* transition.

The order-disorder transition at T_C does have some common features within the various model Hamiltonians. These features are also common to many non-magnetic

systems, due to *universality*. In the approach to the critical temperature, T_C in a magnet, rapid fluctuations in the *order-parameter* (i.e. M) become larger in spatial extent. In a magnet, these fluctuations are called *spin-blocks*. At T_C, individual spin-blocks produced by a microscopic fluctuation grow to infinite extent in an infinite system. The characteristic size (in a rather loose definition) is the *correlation length* ξ. A sort of averaging occurs at T_C, which is responsible for the universal behavior of macroscopic systems which may be microscopically quite different. Without further digression into universal physics, two important results relevant to magnetism are stated here:

$$M(T) \propto (T_C - T)^{\beta}, \qquad T < T_C \tag{2.15}$$

$$\chi(T) \propto (T - T_C)^{-\gamma}, \qquad T > T_C .$$

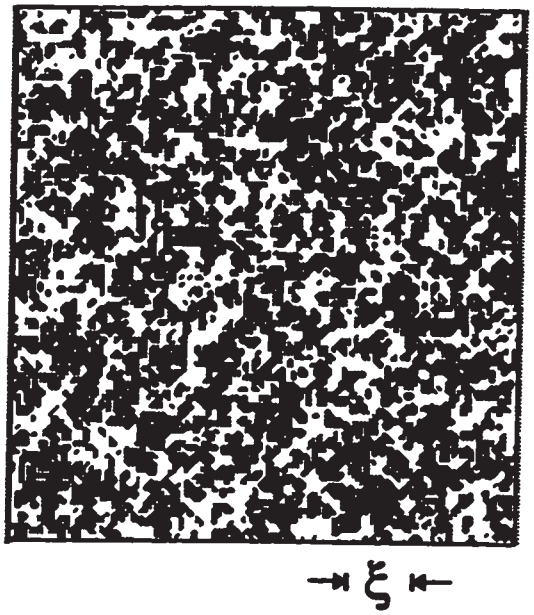

Fig. 2.3 - Blocking of spins near T_C in a snapshot of an Ising system. White areas are spin-up and dark areas are spin-down. This result was obtained from a Monte Carlo simulation on a 128 x 128 lattice in a calculation performed by the author. The correlation length is approximately the average extent of the spin blocks. At T_C, spin blocks engulf the entire magnet.

Note the divergence of χ as $T \to T_c^+$. This is expected, since arbitrarily small fluctuations produce infinite spin-blocks and an external field has a similar effect in aligning spins. Of course, an infinite χ does not occur in real systems. χ reaches a maximum value as ξ approaches the extent of the lattice, or rather, when spin blocks engulf a finite magnet. Fig. 2.4 illustrates the idealized behaviors of M(T) and χ(T). A small tail of M above T_c (not shown) is also a finite size effect. Table 2.2 gives the values of β and γ for common model Hamiltonians.

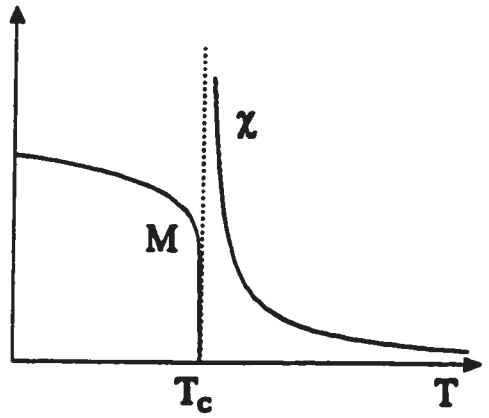

Fig. 2.4 - The behavior of the magnetization M and the magnetic susceptibility χ near the order-disorder transition. M goes to zero at T_c, while χ diverges. In most cases, both exhibit universal behavior.

Model	β	γ
2-D Ising	1/8	7/4
3-D Ising	5/16	5/4
3-D Heisenberg	0.367	1.43[4]
3-D XY	0.345	1.316

Table 2.2 - Some values of the critical exponents β and γ for common models.

2.1.4 Metallic magnets

Magnetic ultrathin films are usually composed of the 3d magnetic elements Fe, Co and Ni, which are *itinerant* magnets. Magnetism arises in these materials from an asymmetry in the spin-up and spin-down band structures. Fig. 2.5 shows pictorially the relationship between the spin-up and spin-down bands for the outermost shells of the 3d metals, which are the 4s and 3d bands. The horizontal axis is the density-of-states and the vertical axis is the energy. Because the outermost 4s conduction electrons experience the anisotropic crystalline environment more than the 3d electrons, the 4s band is much broader than the 3d and has a correspondingly smaller density-of-states. In the Stoner, or band theory of itinerant magnetism, Pauli exclusion may result in a spontaneous band splitting of the spin-up and spin-down bands as shown in the figure. The *Stoner criterion*[7] states that this happens if the density of states is sufficiently localized in energy near the fermi level. Shifting a narrow band, like the 3d, a given amount on the energy axis results in a large decrease in band energy since the filled states 3d are lowered in energy and the other spin band is largely unoccupied. ΔE_{ex}, the *exchange splitting* of the bands, is ~1.8 eV for Fe and 0.5 eV for Ni.[5] In the cases of Fe, Ni and Co, band-filling leads to a ferromagnetic state because the fermi level ε_F lies within the exchange-split levels. For the situation in Fig. 2.5, there are more spin-down(↓) than spin-up(↑) electrons. Band theory explains the fractional moments (in units of μ_B) observed in 3d transition metals. The theoretical moment values of table 2.1 were calculated within a first-principles band model.

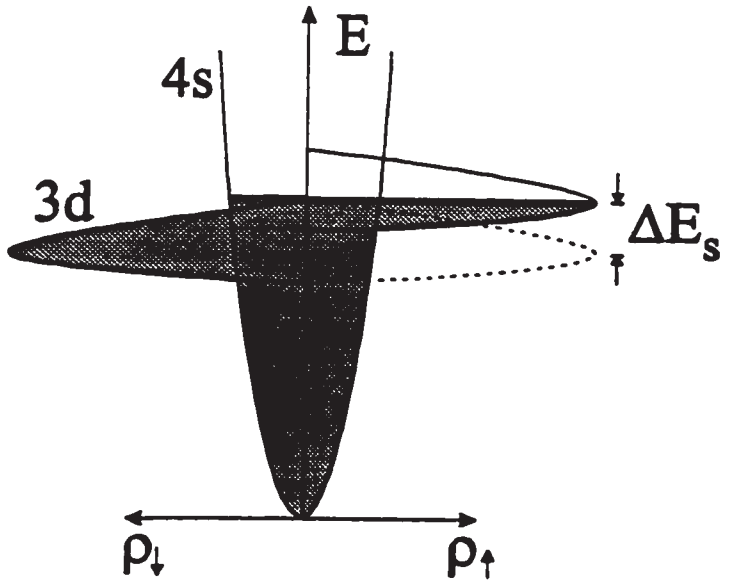

Fig. 2.5 - Itinerant magnets acquire their magnetization by a splitting of the spin-up and spin-down bands, which are shown here pictorially.

The nature of magnetic ordering and of the high temperature behavior in an itinerant magnet is not obvious. Given that Fe, Ni, and Co all appear to be classic itinerant magnets spectroscopically, these behaviors may be surprising. The macroscopic magnetic quantities behave as if there were local moments associated with the atomic sites,[6] although with fractional strengths, all interacting with their nearest neighbors according to eq. (2.11). In the paramagnetic phase, the 3d magnets still exhibit an exchange splitting of the 3d bands. Purely itinerant models do not adequately describe the behavior of these magnets.

Rather than discuss the sophisticated models which combine band and local magnetism descriptions, the following simplification is offered. The 3d band experiences an exchange splitting due to the Stoner mechanism, associating each atomic 3d orbital with a net magnetic moment. A magnetic interaction of the form (2.11) occurs

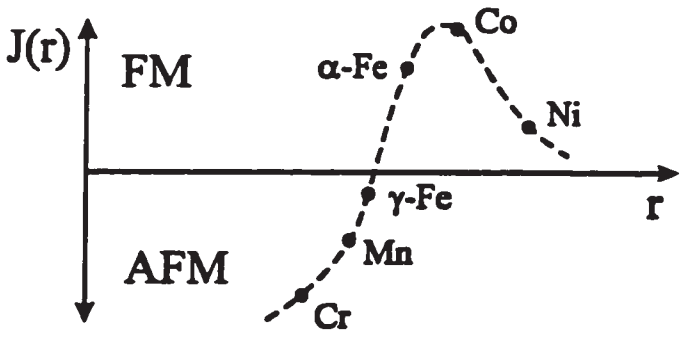

Fig 2.6 - The Bethe-Slater curve shows the dependence of the exchange coupling on the interatomic separation in the transition metal elements. A positive J corresponds to ferromagnetic (FM) and a negative J to antiferromagnetic (AFM). Fe has two structural phases.

via *direct exchange*. This exchange interaction arises from the overlap of the 3d wavefunctions of adjacent atoms. A famous calculation based on this simple physical picture is reproduced schematically in Fig. 2.6 and is known as the *Bethe-Slater curve.*[8] The sign and magnitude of the coupling J varies with the atomic separation r. Negative J values correspond to antiferromagnetic coupling, and positives ones to ferromagnetic coupling. Fe is a particularly interesting case. As one moves from Mn to Fe, a zero-crossing in J occurs. Fe has two structurally distinct phases, α- and γ-Fe, which have different atomic separations. α-Fe is bcc and exists at low to moderate temperatures. At higher temperatures a transformation to the fcc γ-Fe phase occurs. The fcc γ-Fe phase has a smaller interatomic separation, small enough to place it on the antiferromagnetic side of the Bethe-Slater curve. The bulk T_C of α-Fe is below the structural transition temperature to γ-Fe. Since Néel temperatures (which demarcate antiferromagnetic and paramagnetic phases) are generally less than ferromagnetic temperatures, no ordered magnetism is observed in γ-Fe. Magnets similar to γ-Fe, but existing as ultrathin films at

much more accessible temperatures, will be investigated in chapter 4. Those structures are ferromagnetic.

2.1.5 Magnetic Anisotropy

Magnetic anisotropy plays an important role in ultrathin film magnetism. These concepts are introduced in reference to bulk magnets since many of the concepts applied to ultrathin films are borrowed from the bulk. In zero applied field, the moments of a magnetic solid are aligned along an easy axis. By applying a suitably strong field along a hard axis, the moment is aligned with that hard axis. The effect of the magnetic anisotropy is described phenomenologically by a power series expansion in sines or cosines of the angles made with the crystalline axes. A *uniaxial anisotropy* is common among hexagonal closed-packed (HCP) materials where the c-axis is the easy axis. It is customary to expand the uniaxial anisotropy energy as:

$$E_u = K_{u1} \sin^2(\phi) + K_{u2} \sin^4(\phi) + \ldots \qquad (2.16)$$

where ϕ is the angle made with the easy axis and the K_u's are the uniaxial anisotropy constants.[9] Crystals with cubic symmetry have slightly more complicated expressions, due to the presence of three equivalent, mutually perpendicular axes. Bulk anisotropy constants are typically of the order of 10^5 -10^6 J/m^3,[9] or 10-100 μeV/atom. The equilibrium orientation of the moment in an applied field is determined by the minimum of the total energy, eq. (2.16) and eq. (2.8). Considering the first order anisotropy only, the field required to saturate the magnetization along a hard axis is

$$H_s = 2K_{u1}/M. \qquad (2.17)$$

For a magnetization M ~ 10^6 A/m, typical of Fe, Ni or Co, a field of the order of 1 T is required to align M along a hard axis. Anisotropy constants are measured by observing the rotation of M in response to an applied field. Fig. 2.7 is a hard axis magnetization curve, showing the rotation of the moment away from an easy axis in response to an applied field.

Anisotropy constants have been calculated from first principles in a few cases with some success. The first step is a spin polarized band structure calculation in which the spin-orbit coupling term of the Hamiltonian is neglected. Spin-orbit coupling is then treated in perturbation theory with the spin oriented along the hard and easy axes. The difference in the ground state energy is essentially the anisotropy energy.

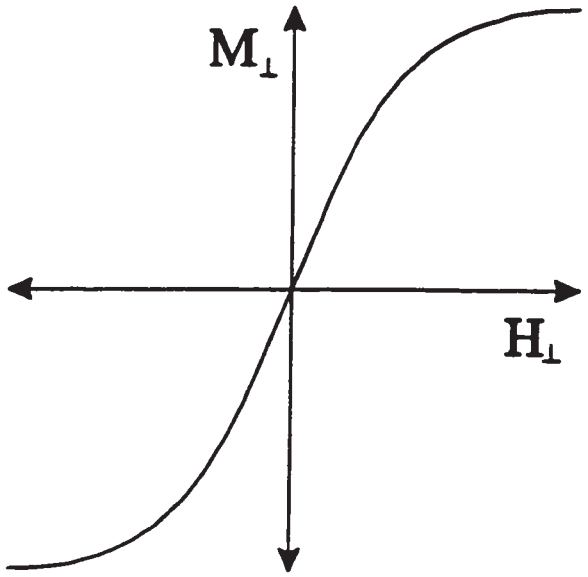

Fig. 2.7 - The response of the magnetization to a magnetic field applied along a hard axis. Most magnets require a field $H_\perp$ ~ 1 T for alignment along the hard axis.

2.1.6 Demagnetization (shape) factors

Although the dipolar field is weak in comparison to exchange energies, it is usually much stronger than the fields produced by laboratory magnets. Because it is a long-ranged force, the dipolar field is determined by the shape of the magnet (i.e. its boundaries) and the magnetization alone. In the calculation of the magnetostatic self-energy of a distribution of magnetic moments, the H-field is usually employed, rather than the B-field. The magnetostatic self energy may be written:

$$E = -\frac{1}{2}\int_V d^3x\, \underline{M}\cdot\underline{B}\cdot \qquad (2.18)$$

$$E = -\frac{1}{2}\int_V d^3x\, \underline{M}\cdot\underline{H} \; - \; \frac{V M^2}{2} \quad ,$$

where $\underline{M}$ was assumed uniform. At a given temperature, only the first term changes so the second term is usually excluded.

$\underline{H}$ is separated into a part produced by macroscopic current sources, and another part due to the magnet boundaries. The first part satisfies the differential form of eq. (2.11), $\nabla\times\underline{H}_J = J_{free}$, where J_{free} is the free current density at a point, while the second part has $\nabla\times\underline{H}_d = 0$. In analogy to the electrostatic field, a zero curl allows the definition of a magnetic scalar potential and the concept of *magnetic charge*. Also in analogy with electrostatics, the magnetic charge density at a point on a magnet's bounding surface is $\sigma = \underline{M}\cdot\hat{n}$, where $\hat{n}$ is the surface normal and $\sigma = Q/A$ is the charge per unit area. A particularly simple example calculation is the demagnetization factor of an infinite, magnetic parallel plate capacitor (in analogy to electrostatics) . If $\underline{M}$ is perpendicular to

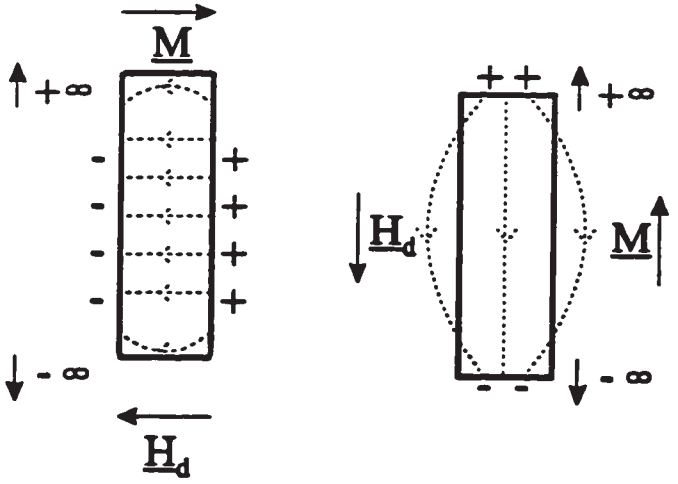

Fig. 2.8 - The demagnetizing field for an infinite plate is equal to the magnetization if M is normal to the plane, or zero if M is in the plane.

the plane of the plate, Gauss' Law over a test area A away from the edges at $\pm\infty$

$$\int d\underline{A}\cdot\underline{H}_d = Q = \underline{M}\cdot\hat{n}A \qquad (2.19)$$

then gives $\underline{H}_d = -\underline{M}$. The minus sign indicates that $\underline{H}_d$ opposes this orientation of the moments. This situation is shown in figure 2.8 on the left. Dashed lines are the magnetic H-field lines, which indicate the direction of force on a positive magnetic test charge. Because magnetic charges only appear in neutral pairs, it is more useful to note that the force due to $\underline{H}_d$ on a magnetic dipole tends to rotate it away from an orientation perpendicular to the plane. By rotating $\underline{M}$ into the plane of the plate as in the right side of the figure, charge appears on the thin edges. $\underline{H}_d$ is no longer uniform between the plates, and in the limit that the plate edges tend to $\pm\infty$, the field line spacing tends to infinity and $H_d = 0$.

In magnets of general shape, $\underline{H}_d$ varies over the volume of the sample even if $\underline{M}$ is uniform, but its average value always opposes $\underline{M}$. The only finite shapes which give uniform demagnetizing fields (for uniform $\underline{M}$) are ellipsoids.[10] The opposition to $\underline{M}$ is the same physics which produces a magnet's fragmentation into domains. For this reason $\underline{H}_d$ is called the *demagnetization field.* Defining the *demagnetization factor* N implicitly as

$$\underline{H}_d = -N\underline{M}\,, \tag{2.20}$$

the parallel-plate examples above give demagnetization factors $N_\perp = 1$ and $N_\parallel = 0$ respectively. These correspond to the extreme values of N for continuous, uniformly magnetized systems.

2.1.7 Domains

Although the dipolar interaction is much weaker than the exchange interaction, it has a profound effect on the large scale structure of a magnet at temperatures much less than T_C. This is possible because the exchange interaction is very short ranged, as the nearest neighbor treatments attest, whereas the dipolar fields of a magnetic solid produce a macroscopic field via eq. (2.5). Flipping all the moments of a solid on one side of a planar boundary to another easy axis reduces the dipolar energy substantially, while increasing the total exchange energy only marginally. The equilibrium, large scale structure of a magnet of general shape, therefore consists of a number of such regions. Homogeneous volumes between the planes are called *domains*, and the planes are called *domain walls.*

Domain walls are not perfectly abrupt, but rather have a finite thickness. This is because the exchange energy of adjacent spins depends on the difference in their

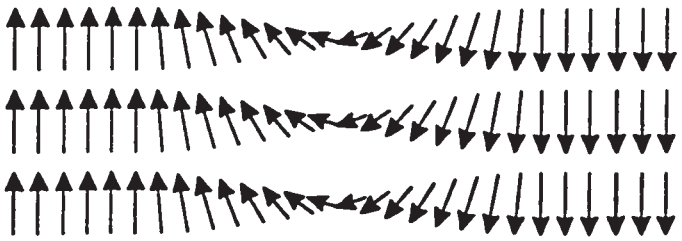

Fig. 2.9 - A cross-section of a domain wall shows how the reversal of the moment is gradual. The gradual rotation reduces the exchange energy of the wall. The wall is limited to a finite thickness by the anisotropy energy associated with a rotation away from the easy axis. Domain walls are typically a few hundred atomic spacings in width.

orientations ϕ as $e_{ex} \propto \phi^2$ ($\cos^2\phi$ for small ϕ). The exchange energy γ_{ex} in a domain wall which rotates uniformly from its original orientation to the opposite direction over N lattice constants a in steps of π/N, as in Fig. 2.9, then goes as 1/N:

$$\gamma_{ex} = Js^2\pi^2/a^2N \text{ .}^9 \qquad (2.21)$$

where s is the local moment. This would suggest that the domain wall thickness is infinite. Domain walls are not infinitely thick, because there is a cost in anisotropy energy at all orientations away from an easy axis. This contribution to the domain-wall energy is therefore proportional to the wall thickness, and is approximately

$$\gamma_K = KNa \text{ ,} \qquad (2.22)$$

where a is the lattice constant and K is a first order uniaxial anisotropy. The domain-wall thickness is determined by minimizing $\gamma_{ex} + \gamma_K$, resulting in a thickness t = Na of

$$t = \sqrt{\frac{Js^2\pi^2}{Ka}} \text{ .}^9 \qquad (2.23)$$

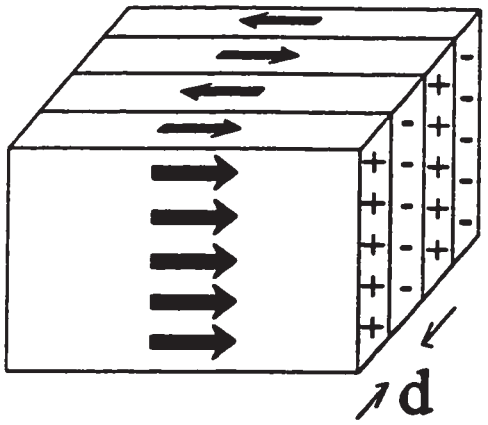

Fig. 2.10 - Stripe domains in a thin slab magnet are energetically favoured over a single domain state, because of a substantial reduction in magnetostatic energy. The domain density is limited by the energy stored in the walls.

Minimization of the total domain-wall energy, $\gamma_{ex} + \gamma_K$ summed over all domain walls, plus the magneto-static energy determines the density of domains. As an example, a sheet domain structure in a uniaxial ferromagnet is shown in Fig. 2.10. The given magnetization results in magnetic charge on the left and right faces of the sheets. In bulk magnets the equilibrium domain width d is much less than the magnet thickness parallel to $\underline{M}$, as on the right side of Fig. 2.8. (Ultrathin films are very different in this respect.) Substantial fringing of $\underline{H}$ occurs within each sheet, and opposing fringing fields, largely from nearest neighbors, nearly cancel that field. The magnetostatic energy is dramatically reduced. A typical length scale of the domain structure in bulk magnets is many microns, and the total energy is reduced by at least a few orders of magnitude.[9]

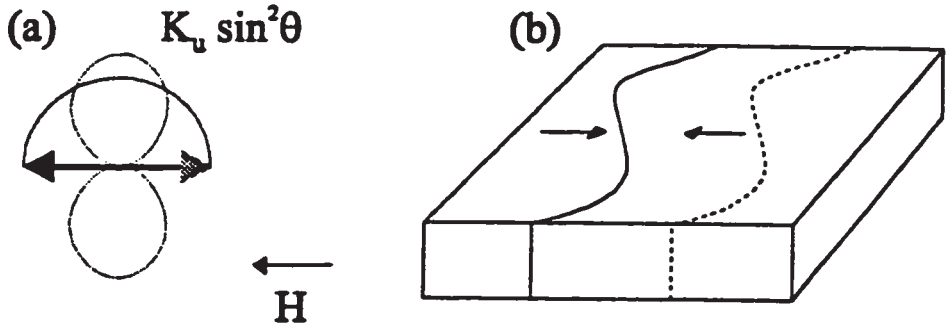

Fig. 2.11 - There are two mechanisms of magnetic reversal in response to a field H applied antiparallel to the original orientation of the moment. (a) Coherent rotation must overcome the magnetic anisotropy by pulling the moment away from an easy axis, through a hard direction to another easy axis. (b) Displacements of domain walls reduce the magnetostatic energy of the magnet as a whole. Domain-wall motion usually requires a smaller applied field and therefore plays a greater role in reversal than coherent rotation in most magnets.

2.1.8 Reversal of the magnetization

A 180° change of the magnetization of a magnet in response to an applied field is known as a *reversal*. Coherent rotation and domain-wall motion are the two mechanisms which produce a reversal. Fig. 2.11 illustrates each mechanism. Coherent rotation occurs when an applied field rotates the moment against the crystal anisotropy. If the applied field is antiparallel to the moment, then the moment will reverse discontinuously to align with H provided H exceeds a critical value called the coercive field. For a uniaxial ferromagnet this field is about 1 T, which is quite large. There is significant hysteresis, since reversal to the original orientation requires a field of the same strength in the direction opposite to the original applied field. In high quality metal crystals, domain-wall motion requires a far smaller field for reversal and is therefore the reversal mechanism in most magnets. Consider the energy stored in the domain wall of Fig. 2.9. The anisotropy

energy due to orientation away from the easy axis is symmetric. This would suggest that the energy of the domain wall is independent of its position, and so its position should be completely determined by the minimization of the magnetostatic energy. Local perturbations in the magnetic anisotropy are abundant in real magnets, however, and they tend to pin domain walls in their vicinity. These perturbations may be due to local strains which change the local anisotropy by an effect known as *inverse magnetostriction*, or by impurity atoms which posses different intrinsic magnetic anisotropies. In any case, the applied field must be strong enough to overcome the barriers presented by the local perturbations in order to reverse the magnetization. In most metallic magnets, the domain-wall motion coercive field is usually at least a factor 10^{-2} of the coherent rotation coercive field.

A plot of M vs. H over the reversal cycle, as in Fig. 2.12 is known as a hysteresis loop. In the case shown, H is applied parallel to the easy axis, and the component of M parallel to the easy axis is obtained. The maximum value of M is called the *saturation magnetization*. Both coherent rotation and domain-wall motion can produce a discontinuous reversal similar to the one shown. A 'square loop' like this one is not the only possible result. The shape of the loop can differ for quite a number of reasons, particularly in magnets of complicated composition and/or microstructure.

The demagnetization factor may have a profound effect on magnetic reversal. Consider a wide, thin plate of Fe with a saturation magnetization of $\mu_o M = 2.2$ T. The total internal field is

$$H_{in} = - NM + H, \qquad (2.24)$$

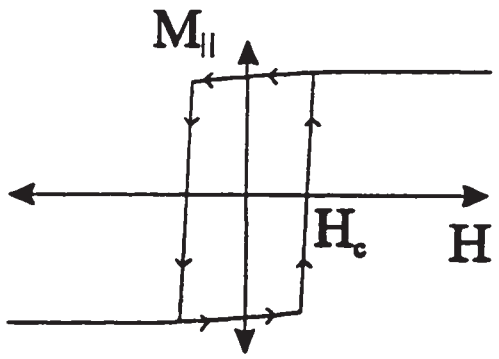

Fig. 2.12 - A hysteresis loop is a record of the reversal process described above. The shape may differ from this, but the hysteresis is a property common to ferromagnets.

where H is the applied field. If M is in the plane of the plate, then reversal requires an H of only a few hundred Oe (1 T = 10^4 Oe). If M is perpendicular to the plane, however, then H must exceed M! This result has profound implications for ultrathin films: ***large magnets are required to reverse the magnetization if it is oriented normal to the film plane***. The fields are big, but usually at least an order of magnitude less than Eq. (2.24) would suggest, due to the motion of domain walls. Demagnetization factors are also expected to have a profound effect on the measured magnetic susceptibility. These points will be central to the discussion of the spin-reorientation transition in chapter 4.

2.2 Magnetic ultrathin films

2.2.1 The strength of local moments

Until this decade, there was considerable confusion concerning the strengths of the moments of the 3d ferromagnets near the surfaces of bulk magnets and in films of only a few atoms thick. In particular, it was commonly believed that dead-layers, or layers with dramatically reduced moment strengths, were common.[11] This belief was based on experiments, since theory predicted an enhanced moment. An enhanced moment was expected because the crystal field, and hence the crystal field splitting of the 3d-band, was reduced at a surface. The reduced splitting results in an increased density-of-states, increasing the measure of the Stoner criterion and increasing the moment strength. It now appears that these early experiments suffered from poor surface cleanliness. Residual gases, primarily nitrogen and oxygen, had reacted with the surface atoms and destroyed the magnetic properties.

Improved surface science technologies and film preparation techniques, in conjunction with *ab initio* calculations, clarified the picture considerably. Moments are often enhanced at surfaces. Perhaps more interestingly, metals which marginally fail the Stoner criterion in the bulk can pass it with the increased band narrowing which occurs at a surface. Ultrathin V/Ag(001) and Pd/Ag(001) are ferromagnetic, for example, while bulk V is not.[12] Other film/substrate systems exhibit a diminished moment at the interface due to hybridization. Calculations of the Co/W(001) ML indicate that it should be non-magnetic.[13] In films which are nonmagnetic at an interface, bulk-like moments are usually present in the remainder of the film.

2.2.2 The stabilization of 2D magnetism

Two-dimensional, purely isotropic magnets are paramagnetic at all temperatures greater than absolute zero (the Mermin-Wagner theorem[2]). In the context of spin-wave theory, magnetic order in 2D is destroyed by low-energy, long-wavelength excitations.[14] Spin-waves are the excited states of a magnet and are sinusoidal modulations of the orientation of the local moment with position, similar to the rotation of the moments within a domain wall. Acoustic spin-wave energies increase with wavevector k (~1/wavelength) as k^2. For each mode occupied, the macroscopic moment is reduced by one local moment. The reduction of the magnetization at a given temperature is determined by the equipartition of thermal energy among the modes. In 3D the density-of states goes as k^2, leading to a reduction in temperature that increases as $T^{3/2}$.[15] This dependence holds for low to intermediate temperatures. In 2D, where the density-of-states goes as k, the reduction exhibits a logarithmic divergence near k = 0. Magnetic anisotropies, whether dipolar or magnetocrystalline in origin, introduce an energy gap so that the mode energy goes as $C + k^2$, where C is a constant depending on the strength of the anisotropy. The reduction in magnetization then goes as ln[kT/C].[16] Thus, magnetic anisotropies play a much greater role in 2D magnetism than in 3D.

2.2.3 Finite-size scaling of T_C and spatial dimensionality crossover

Ultrathin films are often referred to as two-dimensional systems. What then is the criterion for two-dimensionality? At what thickness does the crossover from two-dimensional to three-dimensional behaviour occur? The answer to these questions is

context dependent, and a few suggestions have been offered.[17,18] The suggestions have the common requirement that the magnetic properties be uniform throughout the film thickness. As long as films are less than a few hundred atoms thick, domain walls will not exist parallel to the surface. Even a 10-atom thick magnetic film will exhibit three-dimensional critical exponents, however. This is because the correlation length ξ, and therefore spin-block size, is less than 10 atoms at most temperatures away from T_c, and so the film behaves three-dimensionally. The temperature must be close to the bulk critical temperature before ξ is as big as 10 atomic diameters, and the crossover to two-dimensional behaviour occurs. A criterion based on the critical properties of the film is therefore thickness and temperature dependent.

At the point of crossover to 3D behaviour, the 3D order-disorder transition is preempted by the 2D one.[18] Since $\xi(T)$ is monotonically increasing for $T < T_c$, the dimensional crossover occurs at lower temperatures as the film thickness is decreased. T_c also decreases due to the decreasing average-coordination of thinner films. Finally, at a

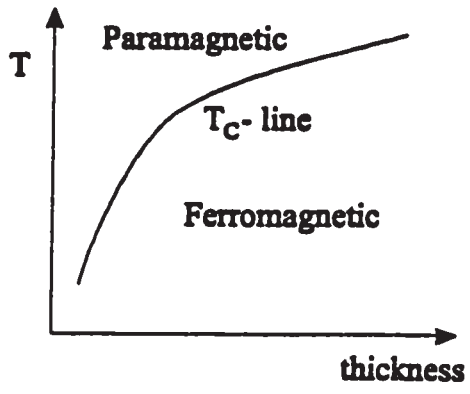

Fig. 2.13 - T_c of an ultrathin film scales monotonically with the film thickness. The greatest change occurs in the first few monolayers of growth.

thickness of 1 ML, an ξ thinner than the film has no meaning and the film is 2D at all temperatures. T_C of the 1 ML film is dramatically lower than for the 10 ML film. The finite-size scaling behavior obeys the trend:

$$(T_C - T_C(n))/T_C \propto n^{-\lambda} \quad ,^{19} \tag{2.25}$$

where T_C is the transition temperature of an infinitely thick film, n is the thickness of the film in ML, and λ is the shift exponent (typically near 1). The finite-scaling behaviour illustrated in fig. 2.13 has been observed by several authors. In a controversial experiment, Baberschke *et al.* tracked the crossover from 2D to 3D behaviour in critical exponents, finding a crossover n = 5 ML and a finite scaling trend resembling Eq. (2.25).[20] A convincing dimensional crossover in the exponent β was reported by Huang et al. for Ni and Co/Ni films on Ag(001). As the film thickness is reduced below 1 ML, a similar transition from 2D to 1D behavior ($T_C \to 0$) may occur providing that percolation is not lost. The 2D to 1D transition was observed by Gradmann et al., in a truly beautiful experiment.[21]

2.2.4 Magnetic anisotropies in ultrathin films

Magnetic anisotropies in ultrathin films have three origins. Based on bulk magnetizations and bulk magnetocrystalline anisotropies, one would expect that the demagnetizing field in an ultrathin film would be strong enough to confine the moment to the plane. Indeed, the demagnetizing field does strongly favor an in-plane moment and is therefore called *the shape anisotropy*. The shape anisotropy does not always prevail, however. Néel first predicted that the broken symmetry at the surface could lead to much

stronger magnetocrystalline anisotropy than in the bulk, at least in the case of cubic crystals.[22] Néel was correct and so this contribution bears his name. The last source of anisotropy is the interface. Near an interface, a magnetic material may be considerably strained from its bulk state. Strain influences the charge distribution in the crystal, and hence the magnetocrystalline anisotropy. Note that this effect may be regarded as inverse magnetostriction. It is called the *magnetoelastic anisotropy*. Hybridization at the interface may also be a factor. This contribution is rather difficult to discuss or anticipate outside of first principles calculations.

All three contributions combine to determine the easy axis in an ultrathin film. Néel first made his prediction in 1954 and the first ultrathin film magnet with a perpendicular moment was observed in 1968.[23] Even now, films with perpendicular moments create some excitement. Those films which exhibit a perpendicular moment, do so in a limited range of coverage, usually crossing over from perpendicular at low thicknesses to in-plane at higher ones. The crossover is appropriately called *the spin-reorientation transition*, although the phrase now encompasses a variety of associated phenomena. Reorientation occurs, in large part, because some of the anisotropy contributions are proportional to the film area, while others scale with the volume of the film. Since it is customary to express the total surface anisotropy in terms of the energy per unit volume, the surface terms scale inversely with the film thickness.

The demagnetization energy of a disk per unit volume is

$$E_D = -\frac{1}{2}\mu_o \mathbf{M}\cdot\mathbf{H}_D = \frac{\mu_o M^2}{2}(N_\parallel \alpha_\parallel^2 + N_\perp \alpha_\perp^2) \qquad (2.26)$$

where H_D is the demagnetizing field, the N's are demagnetization factors for a moment parallel or perpendicular to the plate, and the α's are direction cosines. In the limit that the plate is infinitely thin, $N_\perp = 1$ and $N_\parallel = 0$, giving the standard form of the demagnetizing field for an ultrathin film:

$$E_D = \frac{\mu_o M^2 \cos^2\theta}{2} \quad , \tag{2.27}$$

where θ is the angle made by M to the film plane.

In order to understand how magnetocrystalline anisotropies behave in ultrathin films, a more detailed view of its origins in the bulk is useful. There are two main types of anisotropy which arise from the spin-orbit interaction. One is the anisotropic exchange interaction. Spin-orbit coupling deforms the electron cloud surrounding an atom, in a distribution which is tied to the moment orientation. Rotation of the moment, due to the application of a field along a hard axis, also rotates the asymmetric charge distribution, as shown in fig. 2.13. The overlap of orbitals at adjacent atoms must also change. Each configuration is likely to have a different energy, producing magnetic anisotropy. Another type of anisotropy is the single-ion anisotropy. The crystal field lifts the degeneracy of atomic orbitals, and gives the electronic distribution the symmetry of the crystal. Eigenstates of angular momenta are then connected to the crystal geometry, and hence anisotropy arises in the spin-orbit interaction.

Fig. 2.13 - Spin-orbit coupling deforms the electronic distribution of the atom and ties it to the spin orientation. Adjacent atoms experience an *anisotropic exchange* interaction due to the difference in electronic overlap when the spins rotate.

Néel-type anisotropies arise due to broken symmetry at the surface in the case of cubic crystals. Anisotropies can be expressed in terms of a quickly-converging multipole-type expansion, starting with the dipole term which goes as α^2, a direction cosine. In cubic environments the dipole term averages to zero, leaving only higher order terms to contribute to the anisotropy energy. At a surface or interface, the symmetry of a cubic system is reduced and the dipole term, *typically stronger than the higher order terms*, no longer vanishes. Away from the surface or interface, the cubic environment continues to suppress this term. The dipole-like term, called the *Néel anisotropy*, is therefore a *surface anisotropy* since its contribution to the total anisotropy energy of a thin film is proportional to the film area. When the total film anisotropy energy is expressed per unit volume, surface terms scale inversely with the film thickness. A thin film has one plane of broken symmetry with the substrate and another with the vacuum. Each plane contributes a Néel-type surface anisotropy

$$E = K_s \cos^2\theta / t , \qquad (2.28)$$

where K_s is the surface anisotropy in J/m^2, t is the thickness of the film in meters and θ is the angle made between the magnetization and the surface normal.

Magneto-elastic effects arise from anisotropic exchange via inverse magnetostriction. Magnetostriction is strain induced during a rotation of the spin direction, due to the asymmetry of the electronic distribution tied to the spin. Similarly, epitaxial strain can cause a rotation of the spins, or at least produce a change in magnet anisotropy. This term usually has the form

$$E = 3/2\ \lambda_m\ c\varepsilon\ \cos^2\theta\ ,^{24} \qquad (2.29)$$

where λ_m is the magnetostriction constant, c is the elastic constant and ε is the strain. Depending on the nature of ε, this contribution may behave like a surface or volume term, or even in a more complicated way. Usually, it behaves like a volume term.

2.2.5 Magnetic domains in perpendicularly magnetized ultrathin films

Domains play a more subtle role in ultrathin film magnets with perpendicular magnetization than in bulk materials. Although an ultrathin film with a perpendicular easy-axis creates the largest possible demagnetization field for a given magnetization, domains have little effect in reducing the total film energy. Fig. 2.15 compares the domain structure of (a) a bulk magnetic plate to that of (b) an ultrathin film where the direction of $\underline{M}$ alternates as indicated. Stripe domains, infinite in length but finite in width w, are known to be the ground state of an ultrathin magnet with perpendicular magnetic orientation. For the purpose of these arguments, the domain widths w in the figure are chosen to be the same in both cases, of order 10 000 Å, or several thousand atomic diameters. With this choice, the film and plate contain the same fraction of atoms in their domain walls, so the domain wall energies per unit volume are the same. The

magnetostatic energy is much greater in the ultrathin film, however. In the thick, bulk plate, the domains are long in the direction parallel to M, and narrow in a direction perpendicular to M. In (a), w is If the plate has a thickness t ~ 1 cm, much greater than the domain width. H is small due to extreme fringing and cancellation as discussed in section 2.1.8. Domains of the same width in an ultrathin film (b) have a very large aspect ratio w/t because t ~ 1 Å. Fringing and cancellation are negligible. To substantially reduce H, a ratio w/t ~1 is required, resulting in an enormous cost in exchange energy. While the domain structure of the bulk plate reduces the total energy by about 1000 times,[25] the reduction in ultrathin films is a fraction of a percent.[26]

An interesting and important corollary is that the domain size is very sensitive to changes in anisotropy.[26] As in the bulk, the domain density is determined by the sum of magnetostatic and domain-wall energies. Magnetic anisotropy contributes to the domain-

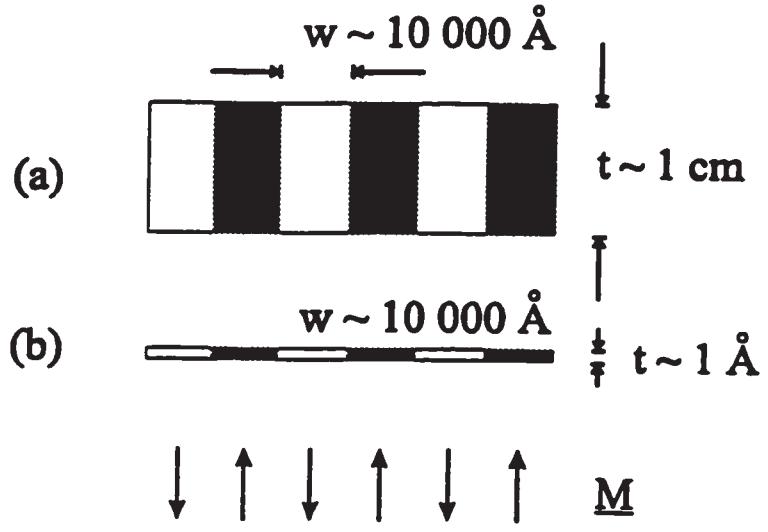

Fig. 2.15 - A comparison of (a) a thick plate to (b) an ultrathin film, shows why domains reduce the total energy substantially for bulk magnets, and only slightly for ultrathin films.

wall term. Since large changes in domain width w produce tiny changes in energy, the reciprocal statement is also true: *small changes in anisotropy energy produce large changes in the domain density 1/w.* This sensitivity has important implications in the approach to the spin-reorientation transition, where the leading terms of the magnetic anisotropy vanish.

2.3 The spin-reorientation transition

2.3.1 The spin-reorientation transition at constant temperature

Spin reorientation ordinarily proceeds from a perpendicular orientation of the moment at low thicknesses, to in-plane for thicker films. At T = 0, the angle θ between M and the film plane is determined by minimizing the total anisotropy plus magnetostatic energy. The net anisotropy energy per unit volume has surface K_s and volume K_v terms as described above, which are combined to give the total perpendicular magnetic anisotropy (PMA) in an applied field H

$$E(t) = -(2\,K_s/t + K_v)\cos^2\theta \; - M\cdot H \,, \qquad (2.30)$$

where K_s is the average contribution from interface and vacuum planes. $(2\,K_s/t + K_v)$ is usually called the effective PMA K_{eff}. A positive K_{eff} corresponds to (with H = 0) a

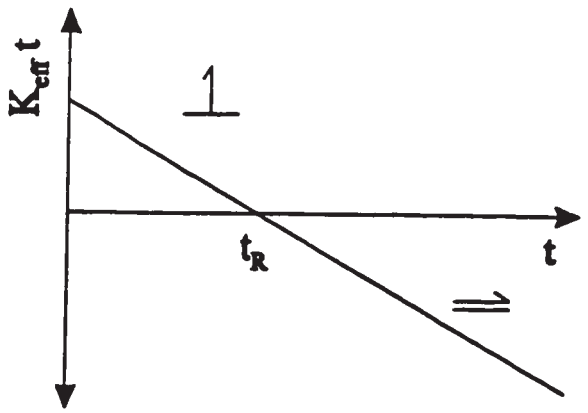

Fig. 2.15 - Surface and volume contributions to the effective perpendicular anisotropy K_{eff} are usually extracted from a study of the thickness dependence of K_{eff}. If the surface anisotropy favors a perpendicular orientation of the moment, then a transition from a perpendicular to in-plane moment occurs with increasing thickness. The thickness at which this occurs is t_R.

perpendicular orientation of the moment, and a negative value to an in-plane orientation. Because of the strong shape term, K_V always favors an in-plane orientation, even if magnetocrystalline contributions prefer perpendicular. In many cases, K_S prefers a perpendicular moment. At some low coverage t the moment will be perpendicular provided $2 K_S / t$ ML $> -K_V$. At greater thicknesses K_V dominates, pulling the moment in-plane. Experimental analyses usually utilize a plot of $K_{eff} \cdot t$ vs. t as shown in fig. 2.15. The point of reorientation from perpendicular to in-plane is $t_R = -K_V / 2 K_S$. Typical values are $K_V \sim 10^6$ J/m^3, $K_S \sim 10^{-3}$J/m^2 and hence $t_R \sim 10$Å.[27]

2.3.2 The Mermin-Wagner theorem

Experimental verification of the Mermin-Wagner theorem has been as widely anticipated as was Néel anisotropy, although less forthcoming. The discovery of spin reorientation caused a resurgence of expectation. It was clear by the late 1980s that magnetic order in ultrathin films was stabilized by magnetic anisotropies which could, for example, constrain the moments to Ising behaviour and finite-temperature magnetic order. Near the coverage t_R where reorientation occurs, the anisotropy was expected to vanish, producing the first 2D isotropic magnets. Calculations predicted that the Curie temperature should plummet near t_R, verifying the essence of the Mermin-Wagner theorem.[28] This behavior would certainly stand out against the usual finite-scaling behavior discussed above. To date, this result has not been reported.

There are two reasons why the T_C drop has not been observed. Firstly, only the leading $\cos^2\theta$ anisotropy terms vanish at t_R.[29] Order is then stabilized by the higher order

terms which are unlikely to vanish. A depression of T_C is possible, however, if the higher order terms are weak enough. The second reason that the T_C drop has not been conclusively observed, is that the thermal behavior of magnetic ultrathin films near t_R is dominated by the proliferation of domains. The crossover from perpendicular to in-plane orientation, as described above, is driven by a competition of surface and volume PMA. A similar crossover is driven by temperature, in which reorientation and domain condensation are excited states of the system, as is discussed below.

2.3.3 *The temperature-driven spin-reorientation*

Pescia and Pokrovsky[31] first predicted that a magnetic ultrathin film with perpendicular magnetization might reorient to an in-plane direction with increasing temperature. They included exchange Γ, *bare* anisotropy (i.e. no shape term) λ and dipolar (shape) strength Ω in a continuum hamiltonian

$$H = \frac{\Gamma}{2}\int \left[\nabla \cdot \underline{n}(\underline{x})\right]^2 d^2\underline{x} - \frac{\lambda}{a}\int n_z^2(\underline{x})\, d^2\underline{x} - \frac{\Omega}{4\pi a^4}\iint \frac{\underline{n}(\underline{x})\cdot\underline{n}(\underline{x}')}{|\underline{x}-\underline{x}'|^3} d^2\underline{x} d^2\underline{x}' \qquad (2.31)$$

where the spin field $\underline{n}(\underline{x})$ is the continuum analog of the discrete spin lattice $\underline{s}_i$ with lattice parameter a. The relative sizes of Γ, λ and Ω are 1000 K, 20 K and 2 K respectively. Because this is a 2D model, at finite temperatures $\underline{n}(\underline{x})$ experiences strong fluctuations away from the perpendicular ground state. The anisotropy λ limits the growth of correlated fluctuations of $\underline{n}(\underline{x})$ away from the perpendicular. Correlated fluctuations, as illustrated in fig. 2.16, cost a total exchange energy proportional to the perimeter length of the fluctuation, while the anisotropy energy grows with the fluctuation area. As a

fluctuation grows, the total anisotropy energy is initially much smaller than the exchange energy at the fluctuation boundary, but at a length scale L_o such that $\lambda L_o^2 \approx \Gamma$, the anisotropy energy equals the exchange. The total energy of the fluctuation then grows much faster as the fluctuation dimension increases.[32] Spontaneous fluctuations are therefore damped spatially over the length scale L_o. Setting λ (and Ω) to zero, the length scale L_o is infinite and long range order is lost according to the Mermin-Wagner theorem. Using a renormalization procedure originally owing to Polykov,[72] the spin field $\underline{n}(\underline{x})$ is separated into two parts $\underline{n}(\underline{x}) = \underline{n}_o(\underline{x}) + \underline{\phi}(\underline{x})$, where $\underline{n}_o(\underline{x})$ is the long ranged, smoothly varying part of $\underline{n}(\underline{x})$ and $\underline{\phi}(\underline{x})$ varies over length scales smaller than L_o. The Hamiltonian

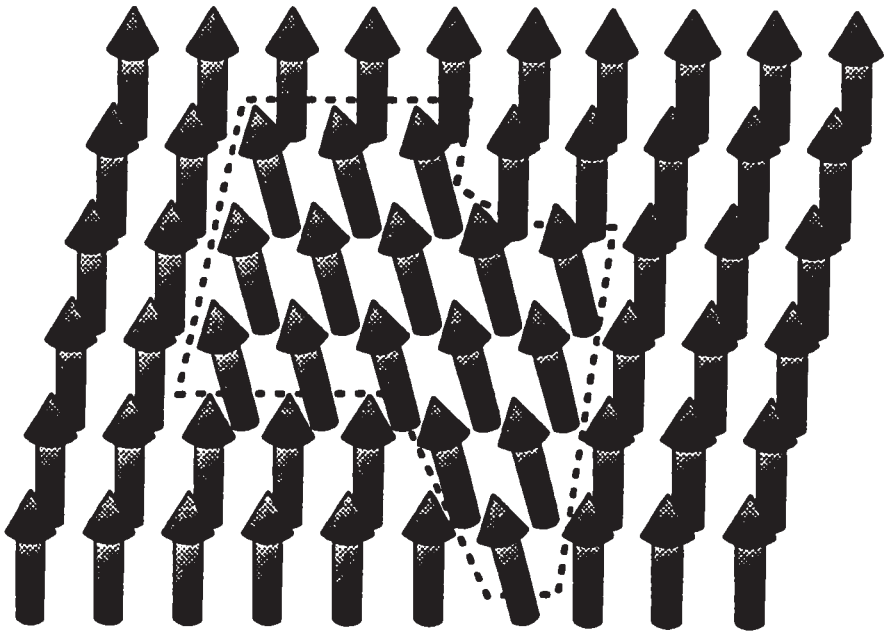

Fig. 2.16 - A correlated fluctuation of spins away from perpendicular in a discrete 2D magnet is outlined in the dotted line. The total exchange energy above the ground state is proportional to the number of nearest-neighbor spin pairs which are not parallel (or the length of the perimeter), while the total anisotropy energy is proportional to number of spins canted from the perpendicular (or the area of the fluctuation).

for $\underline{n}_o(\underline{x})$ is then found by the (classical) thermal average of (2.31) over the short ranged fluctuations. A Hamiltonian for $\underline{n}_o(\underline{x})$ of the same form as (2.31) is recovered, giving temperature renormalized expressions for Γ, λ and Ω:

$$\Gamma(T) = \Gamma Z(T), \qquad \Omega(T) = \Omega Z^2(T),$$

$$\lambda(t) = Z^3(T)\left(\lambda + \frac{3\Omega}{2a} \int_0^{\xi} \frac{e^{-\xi}}{Z^2(T)} \frac{dZ}{d\xi} d\xi \right) \tag{2.32}$$

where $Z(T) = 1 - \frac{T\xi}{2\pi\Gamma}$ and $\xi = \frac{1}{2}\ln\left(\frac{\Gamma}{\lambda a^2}\right)$. $\Omega(T)$ and $\lambda(T)$ renormalize differently with temperature. In particular, $\Omega(T)$ decreases more slowly with increasing temperature than $\lambda(T)$ and

$$\lambda_{eff}(T) = \lambda(T) - \Omega(T)/a \tag{2.33}$$

then vanishes at T_R and the moment reorients in-plane.

A case of interest occurs when $T = T_R$ and the effective, renormalized anisotropy vanishes. In some sense, the film is a 2D isotropic ferromagnet at T_R and a loss of long -range order occurs in the spirit of the Mermin-Wagner theorem. Mills *et al.* determined that M should vanish in a temperature interval $\Delta T_{gap} \sim 1K$.[28] It is possible that this result will never be measured in a laboratory, because of a phenomenon associated with the spin-reorientation transition which will here be called *domain condensation.*

Recent theoretical efforts have focused on the phase diagrams of spin-reorientation transition systems. Such diagrams show coverage and temperature driven transitions within a unified picture. An attempt based on the renormalization group approach by Politi *et al.* is depicted in fig. 2.18.[33] The authors considered films with positive K_s and

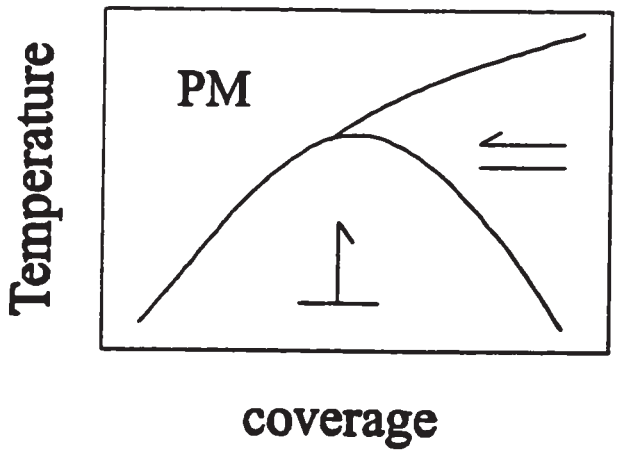

Fig. 2.18 - This phase diagram is a facsimile of a calculation by Politi *et al.* It shows the regions of perpendicular (⊥), paramagnetic (PM) and in-plane (⥤) magnetism for a film with positive K_s.

shape anisotropy, and then varied the film thickness. Ordered and paramagnetic (PM) phases are separated by a critical boundary, and the perpendicular and in-plane boundaries are separated by a reorientation boundary. The two boundaries coincide at the multicritical point of the system, confirming the importance of treating fluctuations carefully. One topological feature is noted for future reference: the boundary of the perpendicular phase has a maximum temperature at or near the multicritical point, where the two boundaries meet. Bader *et al.* have partially mapped the phase boundary of Fe/Ag(100). While their data does exclude the possibility of a maximum, it does not verify it because of the limited range of their measurements which omitted the region of the multicritical point.

2.4.4 Domain condensation

Domain-stripe widths in perpendicular ultrathin magnets are very sensitive to

changes in temperature. Recall from section 2.2.5, that the width is very sensitive to changes in energy, and from the previous section J(Γ), K (λ), and the dipolar field all renormalize strongly with temperature. The problem was investigated by Kashuba and Pokrovsky and by Abanov *et al.* using the same renormalization group formalism mentioned above. Their findings are that the domain-stripe widths are essentially infinite at coverages or temperatures far below the reorientation temperature T_R and that the density increases rapidly as the transition is approached, mimicking a phase transition. The domain density n(T) is predicted to increase as

$$n(T) \propto \exp\{-\pi(\Gamma(T)\lambda_{eff}(T))^{1/2}/\Omega(T)\} \quad .^{30} \qquad (2.34)$$

At sufficiently high temperatures, thermal fluctuations occur in the domain walls, which are less stable than the domain interiors.[35,36] This always happens below the reorientation temperature T_R. Once the fluctuation amplitude is comparable to the domain width, the stripes break into finite-length, but elongated domains which are disordered in position but may retain orientational preference. In analogy with liquid crystals, the low temperature phase possessing orientational and positional order is called *smectic* and the loss of positional order leads to the *nematic* phase. Alternatively, the melting smectic phase may lose positional and orientational order simultaneously, resulting in the *liquid* phase. If the liquid phase does not melt from the smectic, the nematic eventually melts to the liquid. At still higher temperatures, reorientation proceeds directly from this phase. Figure 2.19 illustrates the evolution of the domain topologies with increasing temperature. Abanov *et al.* comment that even if reorientation does not occur, as in the low coverage range of the phase diagram of fig. 2.18, this phase progression may occur.[35] In that case, the

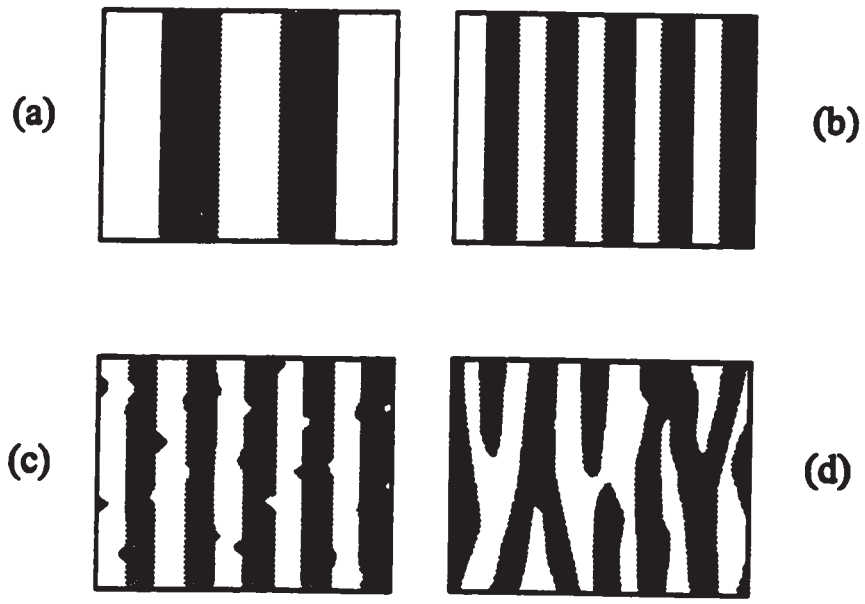

Fig. 2.19 - These stripe domain structures are viewed from above the film. As the spin-reorientation transition is approached from below T_R, the domain-wall and magnetostatic contributions to the energy scale with increasing temperature. At low temperatures, the film is single-domain. Domain stripes form as in the smectic phase of (a), and condense with increasing temperature (b). (c) Fluctuations in the domain walls cause a melting of the smectic phase and a loss of positional order. This phase, (d) is the nematic phase. Loss of orientational order as well gives the liquid phase (not shown).

order/disorder transition proceeds directly from the liquid phase.

Experiments have verified the existence of domains in ultrathin films with perpendicular magnetization. Domains were measured indirectly by Pappas and Hopster[37] and then by Qiu *et al.*[34] Direct observation of domains using polarized electron microscopy was accomplished by Allenspach and Bischoff.[73] They observed the condensation of a nematic domain phase, and eventually a reorientation of the moment. The structure at intermediate coverages was not clear. All of the above experiments measured the remanent (in zero applied field) magnetization.

Another prediction by Kashuba and Pokrovsky is that the domain structure should be very sensitive to an applied field. A domain-stripe structure with stripe-width L in zero applied field, becomes asymmetric in an applied field, with stripes parallel (antiparallel) to the applied field of width L + δ (L - δ) as in fig. 2.20. They calculate

$$\delta = \frac{2}{\pi n} \sin^{-1}\left(\frac{h}{h_c}\right) \qquad (2.35)$$

where $h_c = 4\Omega(T)n(T)$ is the field which converts the film to a single domain.[30] Berger and Hopster recently studied the non-linear behaviour of the magnetization of Fe/Ag(100) in response to fields near h_c.[38] The response near h_c was consistent with the form of eq. (2.35). Implicit in eq. (2.35) is that the magnetic susceptibility should exhibit a simple

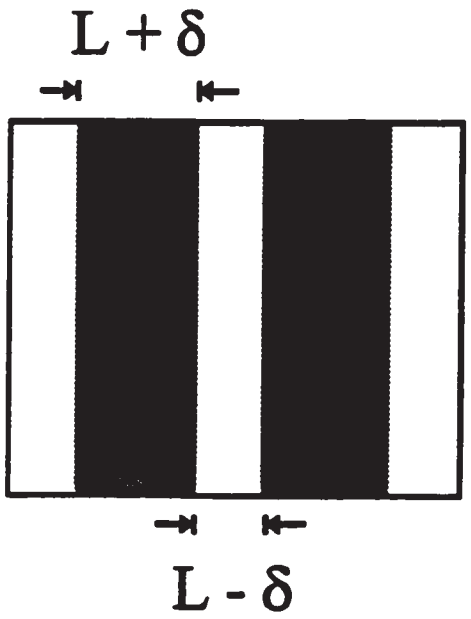

Fig. 2.20 - The domain-stripe structure is very sensitive to fields applied normal to the film plane. Applied fields cause stripes with their M parallel to the applied field to grow by an amount δ at the expense of the antiparallel M stripes.

exponential decay with increasing temperature. This prediction is tested and verified in chapter 4 for ultrathin Fe/Ni films.

3. EXPERIMENTAL METHODS

The experimental methods described in this chapter are naturally separated into two main areas: surface science technology and the surface magneto-optic Kerr effect (SMOKE). Surface science is a multidisciplinary field primarily concerned with free surfaces and films of only a few atoms in thickness. In these systems, problems of interest include atomic and electronic structure, surface morphology, chemistry, epitaxy and crystal growth to name a few.[39] In most ultrathin film magnetism experiments, the film must be prepared *in situ* immediately prior to the magnetic experiments, and those experiments must be carried out within a few hours because residual gases adsorb on the surface and change the film electronic and structural properties. In order to study magnetism in an ultrathin film, one must be an expert in the techniques of surface science. Furthermore, magnetism is highly structure dependent and the film structure is very sensitive to preparation conditions such as temperature and contamination. Useful magnetic results therefore require a careful correlation of film structure and growth conditions. Only with this information can magnetic results be placed in the proper context and so this step is essential.

The magnetic studies of spin-reorientation in Fe/2 ML Ni/W(110) presented in chapter 4 benefits from earlier growth and structure characterization studies. Details of the growth and structure of this system are reported by Johnston,[40] Johnston *et al.*[41] and D. Sander *et al.*[42] C.S. Arnold's contribution to that work was rather technical, and is beyond the scope of the surface science discussion presented in this thesis. Because the

structural results for this system were already available, and because the emphasis of the present work is on the magnetic behavior of this system, the surface science discussion presented here is rather brief. The discussion is intended to demonstrate the techniques which are important for growing ultrathin films and to give a flavor of the techniques used for the structural determination. It is also the author's hope that the surface science section is a useful introduction to future students. *Those readers who are only interested in the magnetic behavior of the Fe/2 ML Ni/W(110) system are encouraged to skip the surface science discussion and go directly to section 3.2 on page 74.* The results of the growth and structural studies are reviewed in section 4.1 without extensive references to the techniques employed.

Having prepared and characterized the structure of a magnetic ultrathin film, a new set of experimental problems arise, related to the measurement of the magnetic properties of utterly tiny samples. SMOKE is a particularly simple and sensitive method for studying magnetism in ultrathin films, and is discussed in detail in the second part of this chapter. The technical innovations and analyses described there are also important contributions of this thesis.

3.1 Surface science techniques

3.1.1 The UHV system

Because of the high reactivity of a clean surface, and because of the sensitivity of structural and magnetic properties to impurities, surface science experiments are normally conducted in ultrahigh vacuum (UHV). All references to the system used in this

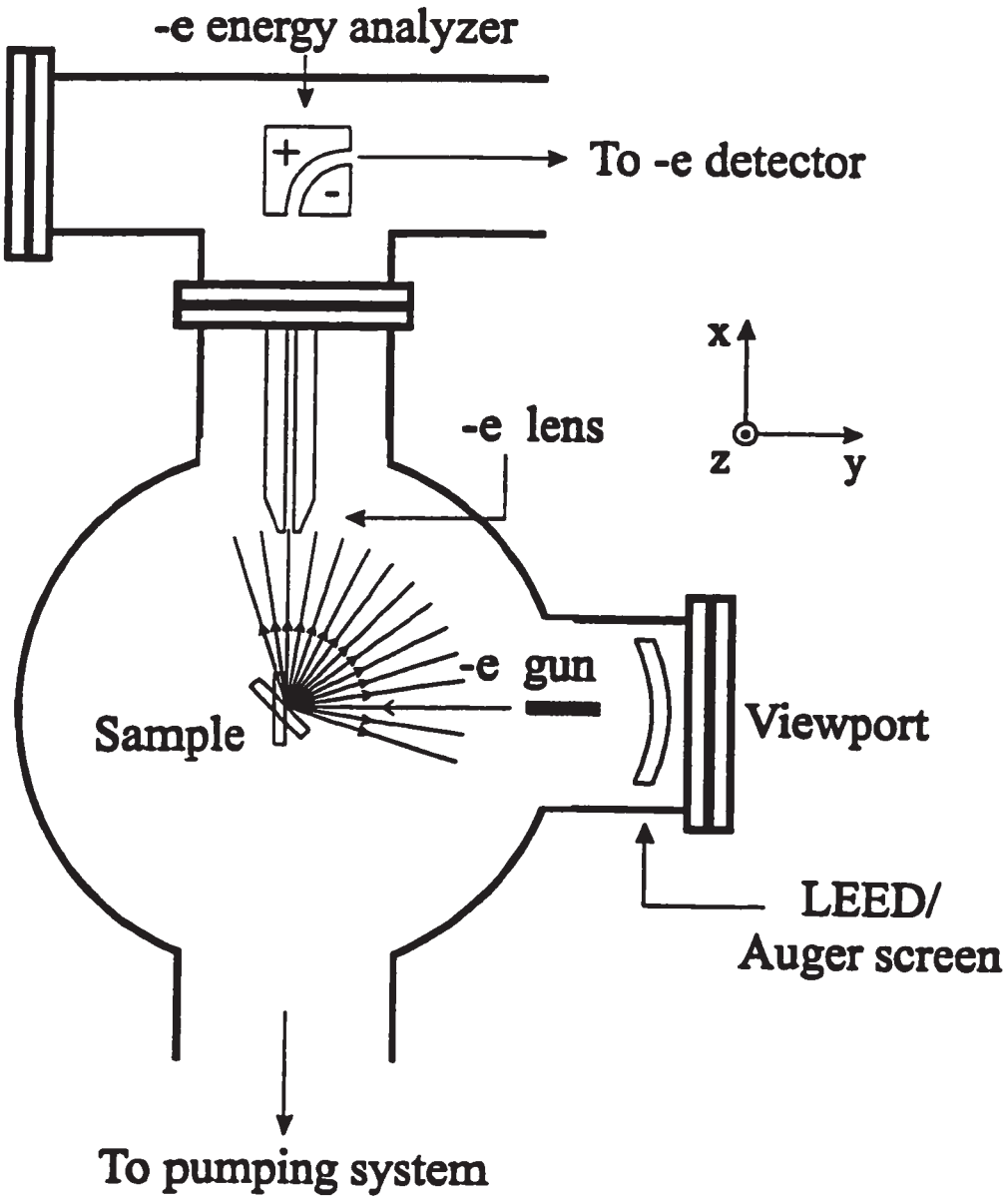

Fig. 3.1 - A greatly simplified view of the UHV system highlights the electronic probes used in the surface science experiments. The same electron gun is used in all measurements. The sample, usually an ultrathin film, grown *in situ* on a tungsten single crystal, faces the LEED/Auger screen for simple measurements. Observation of the electron diffraction pattern through the viewport to the right permits a simple check on ultrathin film structure. Auger electrons are collected on the same semi-spherical screen uopn which the diffraction patterns is projected and provide impurity and film thickness information. Using the electron lens and spherical-section energy analyzer at the top of the analyzer, the angular contrast of Auger electrons is investigated. An analysis of the spatial distribution gives valuable surface structural information.

research will simply be 'the UHV system'. The base pressure of the UHV system is about 10^{-10} torr, or about 10^{-13} atmospheres. At these pressures, residual gas atoms will form a monolayer of contamination on an initially clean surface in about 3 hours. Ideally, an experiment should be completed well within this time frame. In practice, experiments sometimes take longer. In these cases residual gas contamination may affect the results. Whether or not a given level of exposure is acceptable is situation dependent. Ni, for example, is less reactive than Fe and will stay clean longer. Magnetism in a monolayer of material is very sensitive to contamination whereas a thicker film more tolerant.

A greatly simplified rendition of the UHV system is presented in Fig. 3.1. A single crystal substrate is at the center of the spherical main chamber. A sample holder, which is shown in Fig. 3.2, manipulates the sample position and orientation within the main chamber. This view in Fig. 3.1 highlights the electronic probes which were used in the surface science experiments. An electron gun produces a narrow beam of coherent electrons, and focuses it on the center of the sample. The electrons are reflected or diffracted from the sample and analyzed at the LEED/Auger apparatus or, with the sample at an oblique angle, are collected by the electron lens at the top of the main chamber and manipulated by electron optics through a spherical-section energy analyzer.

Auger electron spectroscopy (AES) and low energy electron diffraction (LEED) experiments were conducted. At the moderate (a few keV) incident beam energies employed for AES, the reflected beam has a large elastic component, and fine structure on a large, broad continuum at other energies and angles. The fine structure, in both energy and spatial distributions, contains chemical and structural information specific to the

surface. The surface specificity arises from the shallow penetration depth of medium and low energy electrons, which is typically a few lattice spacings. At lower energies, the penetration depth is even smaller and the electronic wavelength becomes comparable to atomic dimensions. This is the regime of LEED. Electron waves diffract from the surface with a lateral coherence length extending over at least one hundred atomic diameters. Two dimensional Bragg conditions determine angles of constructive interference, connecting the electron diffraction pattern with the surface structure. Both of these techniques will be described in more detail shortly.

For most experiments, the sample was in the 'straight-back' position, with its surface normal aligned in the y-directionof Fig. 3.1, directly facing the LEED/Auger screen. A large viewport on the LEED/Auger flange provided a view of the LEED pattern. The same screen also functioned as a large-area integrating detector in the AES experiments. In angle resolved AES (ARAES) experiments, where the spatial dependence of the AES signal was used to infer structural information, the energy analyzer was used. The objective lens has an aperture of approximately 1° and the energy analyzer was typically tuned for a resolution of less than 1 eV. The spatial dependence was investigated by rotating the sample through a series of polar angles from the 'straight-back' position, to a position with the sample surface facing the electron lens of the energy analyzer (the x-direction).

Manipulation of the sample was facilitated by an elaborate sample holder, which is rendered in a much simplified view in Fig.3.2.[43] The W(110) substrate, about 1 cm x 0.5 cm in area, is supported by three tungsten support wires set firmly in holes on the sides of

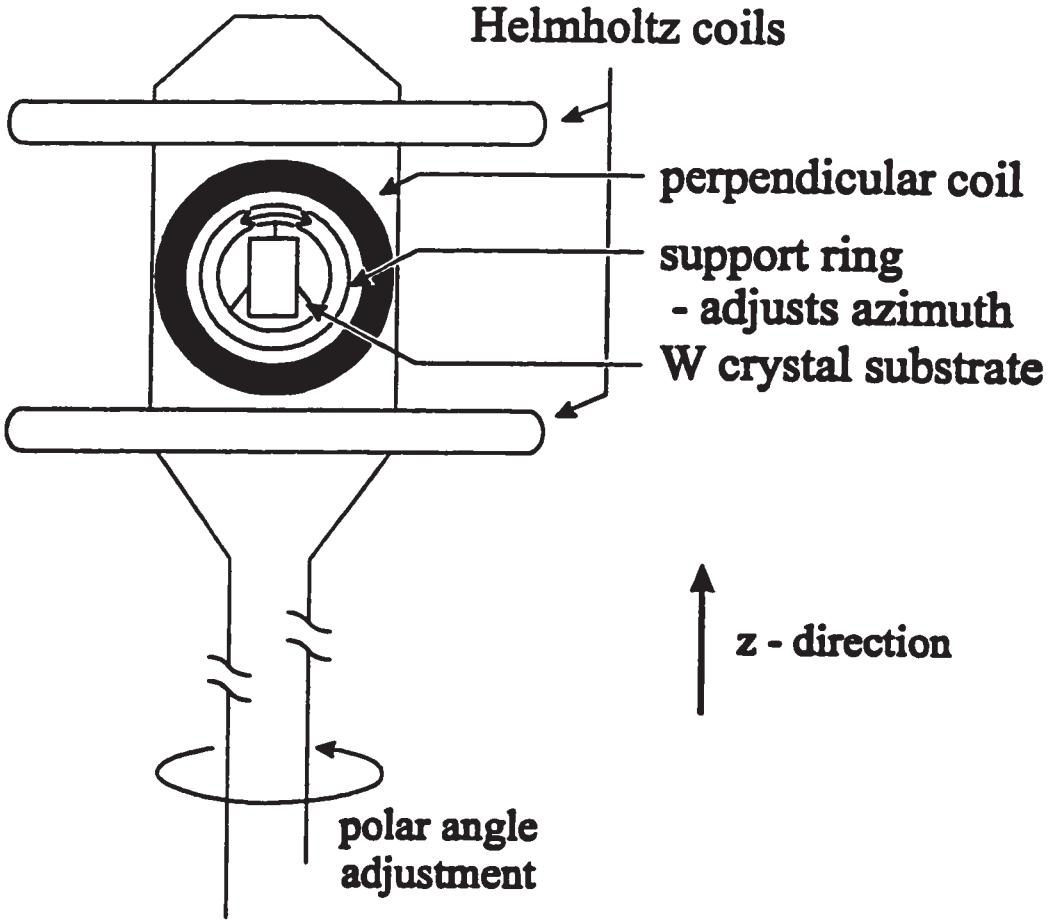

Fig. 3.2 - The sample-holder has its axis along the z-axis, perpendicular to the page of Fig. 3.1, supports and orients the W substrate. A filament behind the sample heats it by radiation or electron bombardment. A cooling attachment (not shown) is fixed to the ring supporting the sample. The holder has xyz translational motion as well as polar and azimuthal rotational freedom as shown. A pair of Helmholtz coils produce a magnetic field in the sample plane, and another coil produces a field perpendicular to the plane. Magnetic experiments are described in the second part of this chapter.

the sample and spot welded to a titanium support ring on the other side. A W-W/Re thermocouple is also in direct contact with the substrate, providing temperature measurement over a range of 200 K to 2500 K. Temperature control is provided by cooling the support ring with a copper braid extending to a liquid N_2 reservoir and heating by high energy electron bombardment of the substrate from a filament behind it. In cases

where less heating is required, radiation from the same filament is sufficient. The titanium support ring sits on a sapphire ball-bearing assembly, providing electrical isolation from the rest of the holder and allowing for azimuthal rotation of the sample in the plane of the figure. Rotation of the entire holder about the z-axis provides polar rotation. These two degrees of rotation allow the orientation of specific crystal axes within the scattering plane and different scattering angles with respect to the surface normal, as shown in Fig. 3.3. Note that this figure is from nearly the same perspective as Fig. 3.1 and perpendicular to Fig. 3.2. For reference in part 2 of this chapter, which focuses on magneto-optics, the light scattering plane is perpendicular to the electron scattering plane. The magnetic field produced by the Helmholtz coils of Fig. 3.2 is in the light scattering plane. A single coil in

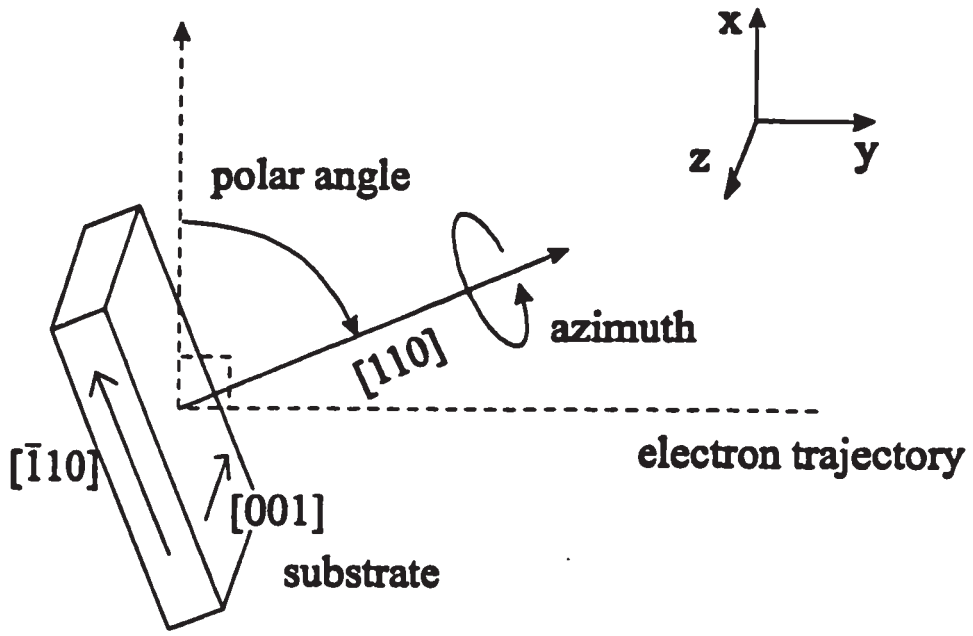

Fig. 3.3 - A viewing-perspective similar to that of Fig. 3.1, but highlighting the electron-scattering geometry with respect to the crystal axes. The polar and azimuthal rotations were accomplished by the sample holder of Fig. 3.2. The substrate is approximately 1.1 x 0.6 x 0.2 cm^3

the plane of the substrate produces a field perpendicular to the substrate. These coils were only used for magnetic measurements.

3.1.2 W(110) substrate

Tungsten (W) was chosen as a crystal substrate for a few reasons. Firstly, W is easy to clean in a UHV environment by electron bombardment. Secondly, it has a very high surface free energy, giving good wetting for at least the first monolayer of adsorbed material. Finally, [111] oriented FCC and HCP crystals of Co and Ni are known to grow well on the [110] face of W.

The W(110) substrate was cut from a W single crystal. Prior to cutting, the crystal was oriented in a Laue x-ray camera in a goniometer. In the same goniometer, the crystal was cut, leaving a surface nominally oriented along the W[110] direction. The piece was removed, trimmed to dimensions 1.1 x 0.6 x 0.2 cm^3, and placed in a special polishing goniometer. Mounting holes were spark cut in the sample sides under oil. The sample was oriented via Laue to within 0.1° of the [110] direction in this goniometer. Grinding with silicon carbide paper, followed by diamond paste(6 - 1 μm) and finally Al_2O_3 vibratory polishing (0.02 μm), gave a highly polished surface. A preliminary cleaning was performed by ultrasonic cleaning, followed by an acetone wash and vapor degreasing in a methanol atmosphere.

Once mounted on the titanium support ring, the crystal was cleaned and annealed in the UHV chamber in the same process. Heating to high temperature (flashing) is sufficient for annealing, but carbon contaminants bond very strongly to W,

and are not removed by flashing. Exposure to a partial pressure of 10^{-6} torr O_2 reacts surface carbon with O, forming CO. CO has a relatively low desorption temperature and is easily removed by flashing. The cleaning procedure was therefore a series of O_2 exposures followed by flashing to 2800 K. The carbon contamination was measured after each cycle by AES. The process continued until the C contamination was below measurable limits. After the initial cleaning, the sample received a daily cleaning for maintenance. Using the calibration of Kolaczkiewicz *et al.*,[50] 'clean' corresponded to an upper limit of a few tenths of a percent of C contamination near the surface.

3.1.3 Film deposition

Films of Fe, Ni and Co were grown onto a clean substrate by electron beam evaporation, a form of molecular beam epitaxy (MBE). The basic principle of this technology is illustrated in Fig. 3.4. A wire of the material to be evaporated (evaporant), 1-2 mm in diameter and initially 7 cm in length, is supported rigidly in an insulated support (not shown) in front of a hot W filament. The wire is raised a few kV above the filament potential, so that thermionically emitted electrons bombard the end of the evaporant wire. With sufficient delivered power (about 5 watts), evaporation takes place from the end of the wire. An aperture collimates the evaporant beam, to give a beam diameter of about 1 cm at the sample. A constant fraction of the evaporation beam is ionized, and this fraction provides a convenient means of maintaining calibration. By monitoring the current (~ 1 nA) on the second aperture, a signal proportional to the flux rate is obtained. The forward flux of the evaporator is extremely small, making a deposit of 1 *monolayer* (ML) in

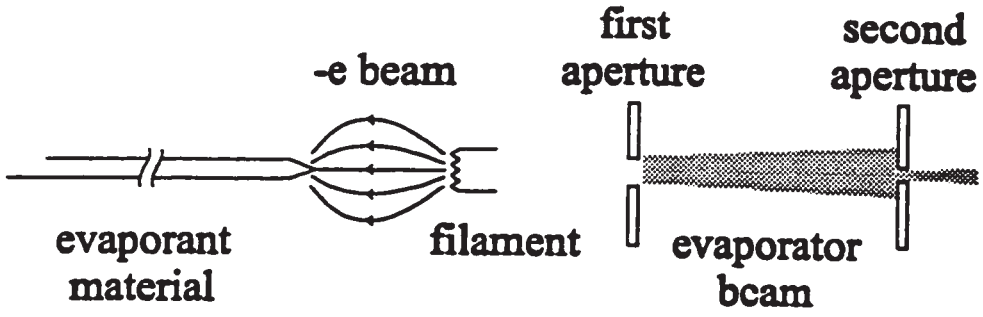

Fig. 3.4 - An illustration of the basic workings of an electron beam evaporator. Electrons are thermionically emitted from a filament and accelerated towards the end of the wire of material to be evaporated. The end of the wire becomes hot and evaporation occurs. The beam of evaporant is collimated by apertures. Forward flux rates are of the order of an atomic layer in 5 minutes.

approximately five minutes. A monolayer is one atomic layer. Fractional monolayers (i.e. 1.5 ML) correspond to incomplete layers. This slow evaporation rate permits controlled film growth on the scale of atomic thicknesses.

3.1.4 Film growth modes

The manner in which incoming atoms of a growing overlayer build up a film on a substrate is referred to as the *growth mode*. One could imagine, for example, that atoms might stick where they first impinge upon the surface. Another scenario could have adatoms (adsorbed atoms) diffusing by thermal activation until they find a deep energy well, as at the edge of an atomic step where the atom would have a relatively high coordination. Note that these barriers are at least an order of magnitude greater than the total magnetic energy per atom, so that magnetic forces are not strong.[44] These two scenarios are extremes: the first is a zero temperature limit, where diffusion is irrelevant and the second is a high temperature mode, where the equilibrium state is rapidly achieved. Textbook discussions of growth modes usually describe equilibrium growth

modes.

Equilibrium growth modes are of three varieties, the simplest being layer-by-layer or Franck-Van der Merwe (FV) growth. In this form of growth, growth of the n^{th} layer does not begin until the $(n-1)^{th}$ layer is complete. Obviously, this is the preferred mode of growth for ultrathin film engineering, since perfect interfaces can be made. Two other (more common, unfortunately) growth modes are Stranskii-Krastanov (SK) and Volmer-Weber (VW). In the SK mode, the 2^{nd} layer growth does not begin until the first is complete, but once the 2^{nd} layer starts growing, they form tall crystallites, usually with the bulk lattice parameters, on the smooth monolayer. This kind of crystallite growth is known as 3D growth. In the VW mode, 3D growth begins from the onset of growth on the clean substrate. The three equilibrium modes are shown in Fig. 3.5. SK and VW modes are obviously disadvantageous with respect to film engineering. Luckily, metastable growth modes approximating FV are often possible by reducing the substrate temperature during growth. Once a metastable layer is covered, its stability is enhanced since bulk diffusion is usually slower than surface diffusion.

3.1.5 Low energy electron diffraction (LEED)

LEED is now a highly developed technique, and is very well understood amongst surface science theorists. An excellent textbook by Van Hove treats the subject in great detail, both from qualitative and quantitative perspectives.[45] Since the qualitative use of LEED in ultrathin film science is rather more straightforward and well-documented, it is discussed only briefly here. Because of the wide use of diffraction techniques in

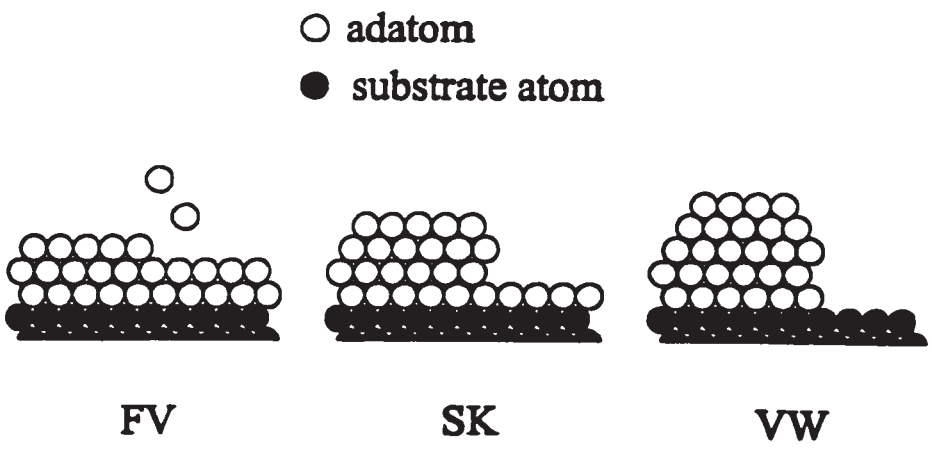

Fig. 3.5 - Three common equilibrium film-growth modes differ in how incoming adatoms are distributed among the layers. FV growth, also called layer-by-layer growth, produces smooth films and abrupt interfaces. The other two modes produce rough surfaces.

condensed matter physics and materials science, scientists from these fields have a good intuition for interpreting LEED patterns.

In principle, electron diffraction measurements of an ordered surface can be simulated to give the surface structure. Because of the very high scattering cross-section that low energy electrons have, multiple diffractions complicate the interpretation of the dependence of the diffracted intensities on direction and energy. Powerful and 'user-friendly' analysis packages are now available to experimentalists, and quantitative interpretation of LEED data is becoming a more popular option. This advance has yet to be implemented by the McMaster group. Luckily, the qualitative interpretation of the diffraction pattern as viewed on a LEED screen is relatively straightforward, since the orientations of diffraction maxima are unaffected by multiple scattering; rather the intensities are affected. This is because multiple diffractions translate points of the reciprocal lattice by a sum of reciprocal lattice vectors to another point in the reciprocal lattice, and not producing fractional spots. Fractional spots do occur, but are interpreted

in terms of an increase in the period of the direct-space surface net. It is at the qualitative level that LEED patterns were employed here. For the interpretation of LEED spots, one simply has to invert the 2D pattern to obtain direct space periodicities.

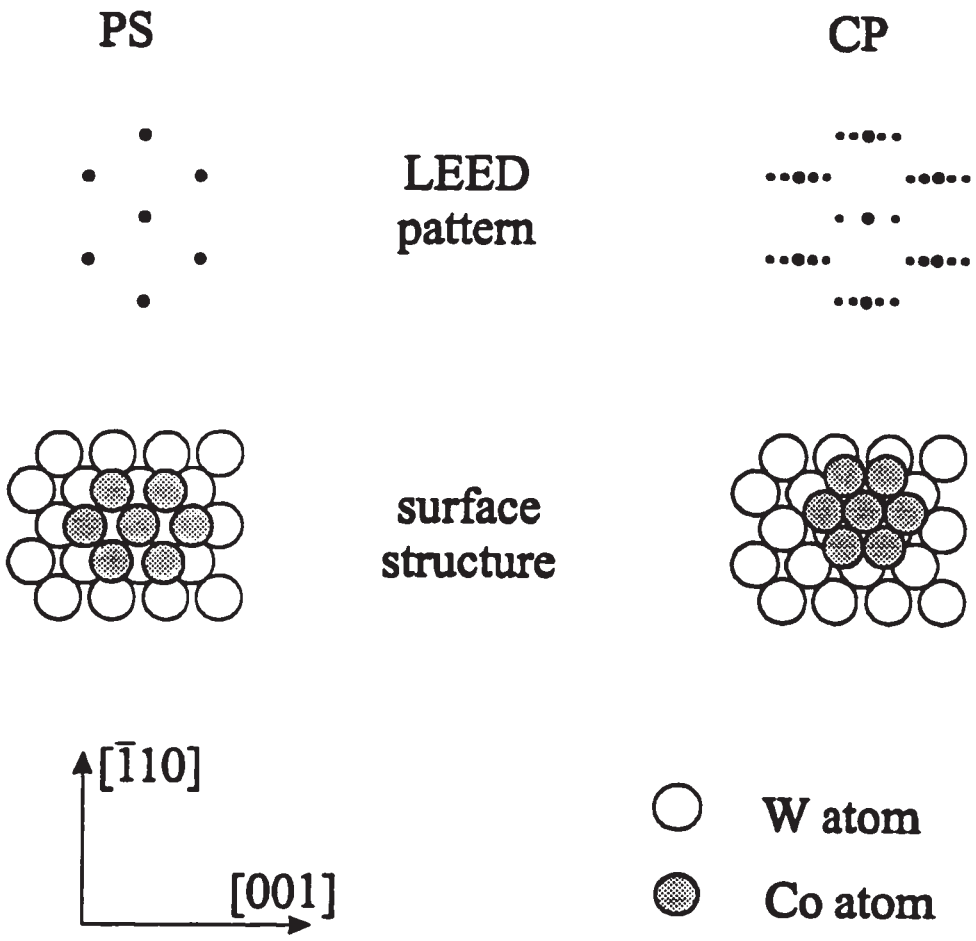

Fig. 3.6 - The LEED pattern is observed to undergo a transformation during the growth of the first ML of Co on W(110). The pattern on the left is the same as observed for clean W(110), indicating that the film is pseudomorphic (PS), which means it follows the substrate periodicity. A satellite pattern develops before the completion of 1 ML, with a spacing of 1/8th the PS pattern along W[001]. This indicates a transformation to a close-packed (CP) structure, which has nearly the same structure as the bulk Co (0001) plane.

Rather than giving a detailed description of qualitative LEED, the following example of Co/W(110), now well understood, is presented. This example is also useful, because of the similarity of Co/W(110) and Ni/W(110), which was utilized as a substrate in the magnetic studies of chapter 4. Fig. 3.6 shows the transformation observed in the LEED pattern of submonolayer Co/W(110). The correspondence between the LEED pattern and real space surface is as indicated in the figure. The LEED pattern on the left is observed for the bare W(110) and for low coverages of Co, indicating that Co initially grows *pseudomorphically* (PS) which means following the substrate structure. At higher coverages, the LEED pattern transforms to that shown on the right of the figure, to a satellite pattern with a spacing of 1/8 of the PS spots. Other experimental tools prove that this happens before any occupation of the second ML. In real space, it now takes 10 Co atoms per 8 W atoms for the structure to repeat itself along the [001] direction. The changing LEED pattern corresponds to a transformation from the PS structure to a close-packed (CP) structure which has nearly the same structure as the bulk Co (0001) plane.

3.1.6 Auger electron Spectroscopy (AES)

AES is one of the most popular techniques for monitoring surface cleanliness. Until recently, it was also the most widely used technique for the thickness calibration of ultrathin films. Its decline in popularity is due in part to the current interest in multilayer materials, which are more convenient to monitor by the technique of reflection high energy electron diffraction (RHEED). Another reason for its decline in popularity is that many surface scientists were disillusioned by problems of interpretation of AES attenuation and

buildup curves. Indeed much of the AES analysis in the literature is questionable. This section addresses these problems of interpretation and demonstrates analytical and experimental solutions. AES is still a valuable technique when applied to ultrathin films;[46] it is even more powerful than it was believed to be in the past, when properly applied.[47]

Auger processes occur when moderately high energy (~keV) electrons bombard a surface. At these energies the predominant scattering mechanism is scattering from valence electrons. The incident electrons typically scatter many times, producing a cascade of secondary electrons. The energy distribution of ejected secondary electrons is continuous, broad and smooth. Auger processes represent a smaller fraction of the total cross-section and appear as small features on the secondary electron background. An Auger process is shown in Fig. 3.7. Auger processes begin when radiation (usually primary or secondary electrons) scatter inelastically from a surface atom, ejecting a core electron and leaving an excited ion. An electron in a higher shell decays to fill the core state and the excess energy is carried away by another (outer shell) atomic electron. The kinetic energy of that final ejected electron is completely determined by the atomic properties of the atomic species in question. The final electron is a relatively low energy electron and therefore has a short mean-free-path. Only events which occur near the surface contribute to the total signal. Auger processes are labeled according to the three states involved, as in the KLL process of 3.7, and by the atomic species.

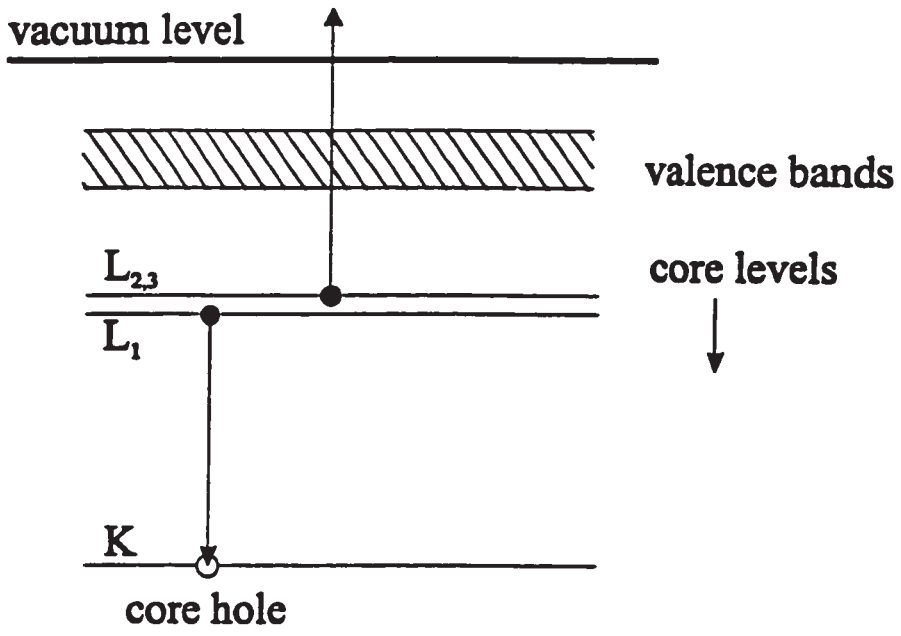

Fig. 3.7 - An Auger event is one in which a core hole, produced by high energy radiation, is filled by an atomic electron. Another atomic electron, known as an Auger electron, carries away excess energy. The energy of an Auger electron is therefore determined by the atomic properties.

The basic measurement technique is now described. With the sample in the 'straight-back' position of Fig. 3.1, ejected secondary and Auger electrons are collected by the semi-spherical LEED/Auger screen. A retarding grid placed between the sample and screen rejects all electrons below a selected energy. Since the AES signals are small features in a smooth secondary-electron background, they are extracted by a derivative measurement. This is achieved by a lock-in measurement with a sinusoidal modulation on the retardation grid. Since the current on the semi-spherical screen is an integral over energies from the retardation potential to the beam energy, the spectral derivative is the 2nd derivative of the screen current. The $2f$ component of the screen current is therefore measured. In a typical AES measurement, the retardation potential is varied over a narrow range of energy containing a spectral feature of the desired atomic species. Fig. 3.8

shows small AES features on a secondary electron background and the relation to the derivative. The secondary electron background is likely to be flat over the range, but probably has some slope which enters the derivative as an offset which is easily removed.

In a uniform ultrathin film, a specific Auger transition from a certain element, gives the following idealized intensity. Within a given layer, the AES signal is proportional to fraction of the layer which that element comprises. This may be less than 100% if the film is made of more than one element, or if the layer is on the top and is incomplete. The total signal from a given layer is attenuated exponentially according to the mean-free-path of electrons at the Auger energy and according to the depth of the layer within the film. Penetration depths are typically a few MLs for incident energies less than 100 eV.[48] All layer contributions are then summed to give the total AES signal.

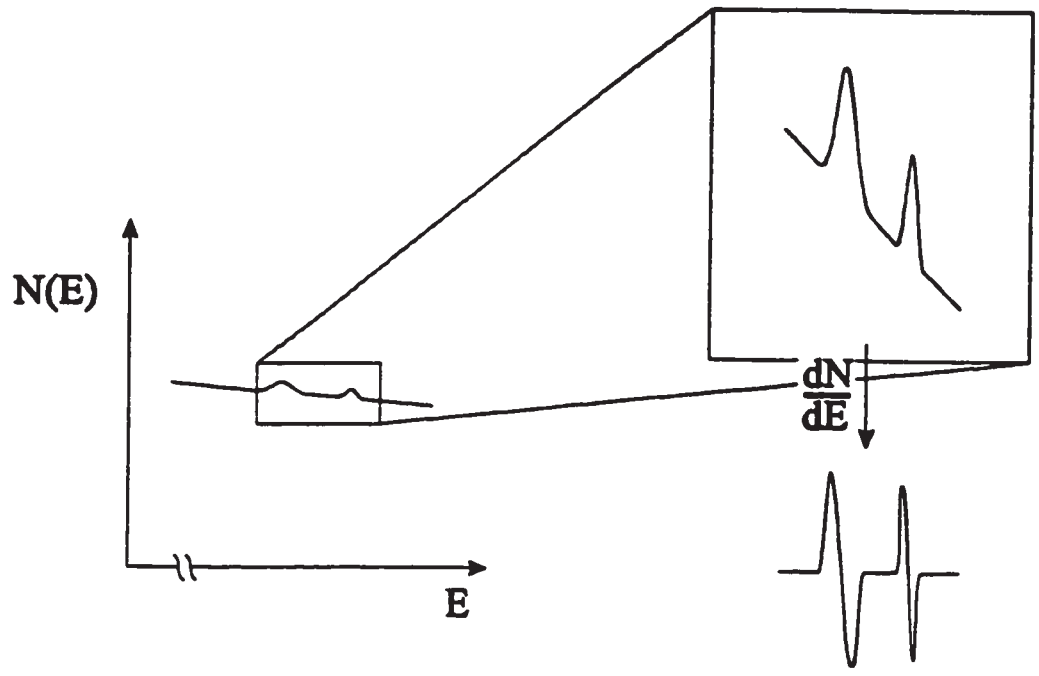

Fig. 3.8 - Auger events appear as small features on a large, but smooth secondary electron background. When the derivative is measured, the Auger contribution is enhanced relative to the background, which only produces a constant offset.

Ultrathin film growth modes are monitored and film thicknesses calibrated using these principles. If an AES transition of the overlayer material is monitored during film growth, the resulting AES intensity versus coverage relationship is commonly known as an AES *uptake curve*. The analogous attenuation characteristic of a substrate Auger transition is called an *attenuation curve*. Applying the above principles to the case of FV growth, these characteristics are expected to be linear during the growth of a particular layer. The intensities at consecutive layer completions will approach the bulk value or zero exponentially for the overlayer or substrate AES signals respectively. Since the overlayer and substrate signals are likely to have different energies, the mean-free-paths are likely to be different. Fig. 3.9 summarizes the idealized behavior of overlayer uptake

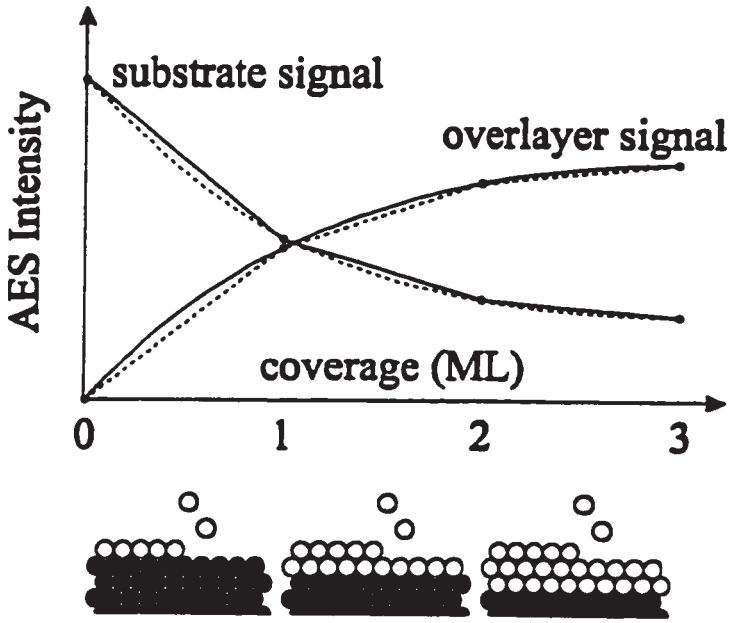

Fig. 3.9 - The Auger signal from the substrate (overlayer) decreases (increases) with increasing coverage. Changes in slope occur at layer completions and are called *breakpoints*.

and substrate attenuation AES curves for FV growth. Linear trends between layer completions are solid lines. Slope changes which occur at the completion of layers are called *breakpoints*. Since complete layers attenuate electrons exponentially, the exponential trends pass through the breakpoints.

Although it is possible to measure uptake and attenuation curves which have very low noise levels, even with very modest apparatus, poor results are common in the literature. Specialized, high sensitivity Auger units are capable of making very low noise measurements by simply measuring the difference between crest and trough in the dN/dE signal in single measurements. For a LEED/Auger apparatus like the one employed in the present system, this is not practical because of a higher noise level intrinsic to the retarding analyzer. The solution employed in our laboratory is to measure a series of points over the range of an AES feature and fit the amplitude to a standard spectrum, improving the statistics by using many points. This procedure produces results comparable to those obtained from far more sophisticated (and expensive) Auger analyzers. Another important experimental consideration is the choice of Auger transition. Most overlayers and substrates are at least moderate in atomic number, and possess transitions in a few energy ranges. Since electrons have a minimum in their inelastic mean-free-path (IMFP) in the 50 - 100 eV range, Auger electrons with these energies are the most surface sensitive, giving the strongest slope changes at breakpoints, for example.

Even after overcoming noise problems, experimental AES curves are often found to differ from the ideal behavior of Fig. 3.8 for a variety of reasons. Firstly, the growth mode is often not FV, and so breakpoints marking the completion of the $(n-1)^{th}$ layer and

the beginning of the n^{th} layer may not occur simultaneously. Other problems are due to complications in the spectra. AES features from overlayer and substrate sometimes overlap. Another spectral problem is that interfacial or alloyed atoms may experience chemical shifts in the transition energy and lineshape. Finally, changes in film structure change attenuation and may shift breakpoints due to changes in density.

Fig. 3.10 is an example of two AES uptake curves for the growth of Co/W(110). Co has a large AES feature in the 40-60 eV range, overlapping with a small W feature. In order to separate the two features, AES measurements were fit to a linear combination of two reference spectra: a clean W spectrum and one obtained from a thick (>8 ML) Co film. The weight of the Co reference is plotted versus coverage during two separate film growths. Previous studies which ignored the overlap are unreliable.[49] Room temperature (RT) growth produced the solid-line, while the second film was annealed to 700 K at a coverage of 6 with no additional heating at higher coverages. Comparing the observed LEED pattern to the literature (i.e. Fig. 3.6), the coverage range 0-6 corresponds to less than 1 ML. LEED patterns always indicated PS growth at coverages of 4 or less, with the satellite pattern of figure 3.6 appearing at higher coverages. For somewhat higher coverages, the PS pattern can be restored by annealing. Returning to the AES data, RT growth produces a weak breakpoint a 6, and no clear breakpoints at greater coverages. Annealing at 6 delays the breakpoint to 8 and results in a greater change in slope. This effect was explained by Kolaczkiewicz and Bauer for Ni/W(110),[50] and applies also to Co/W(110). The PS - close-packed (CP) transition,[51] which takes place in the first ML of growth, involves an activation energy. For RT growth, the transition is only partial

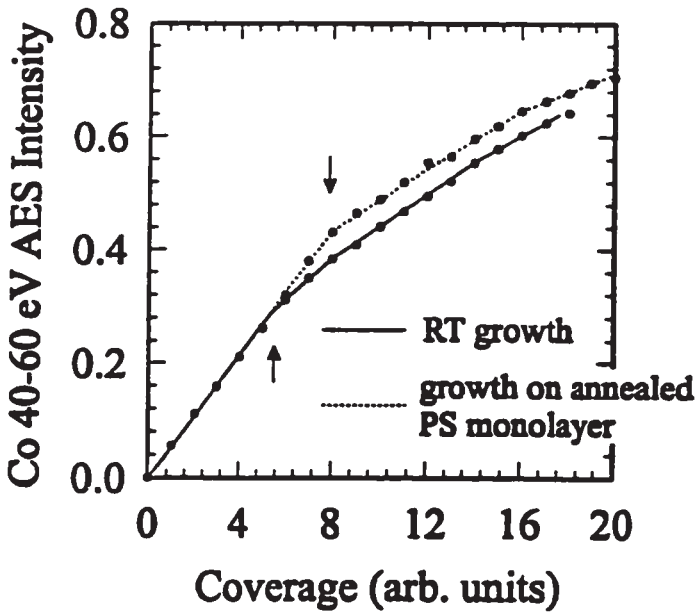

Fig. 3.10 - AES uptake curves for the growth of Co/W(110). The film grown at room temperature (RT) shows a weak breakpoint at 6 units of coverage, before the first ML is complete. The annealed film shows a strong breakpoint at 8 units, the completed first ML.

because of this barrier. Growth of the second layer then begins prematurely, freezing in an inhomogeneous first layer containing a high density of defects. By annealing the (nearly finished) first layer before growing the second, the PS → CP transition is complete, producing a more homogeneous, well-ordered first layer. The strong breakpoint at a coverage of 8 corresponds to a complete CP layer.

The second AES example is very relevant to the growth of Fe, Co and Ni films which have similar thermal stability characteristics on W(110). It is well-known that all of these metals on W(110)have an SK equilibrium growth mode. Although the first layer grows best if the substrate is heated, second and subsequent layers grow best if the sample is maintained at a lower temperature. One hopes to achieve a pseudo-FV growth mode in this manner. It turns out that there is a critical temperature, above which the metastable, relatively smooth film, gradually transforms to the stable, 3D islanded form. Fig. 3.11 is

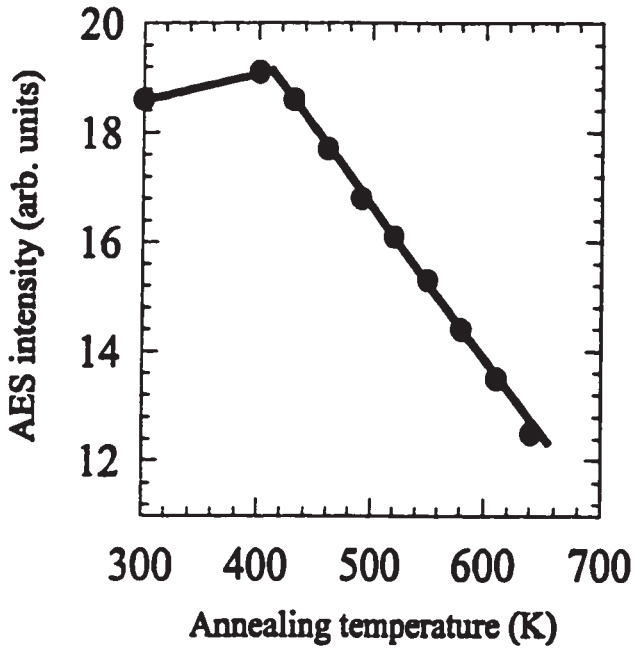

Fig. 3.11 - An annealing study shows the thermal stability of a 2 ML Co film on W(110). Annealing produces smoothing for temperatures less than 400 K, as seen by the initial rise in Co AES intensity. At higher temperatures, islands form on the stable Co ML. Note that 11 of the AES units corresponds to the signal from 1 ML.

an AES thermal stability study of a 2 ML Co film, similar to a result by Johnson *et al.*[49] The Co 40 - 60 eV AES intensity was measured after annealing to successively higher temperatures. After an initial increase in AES intensity by annealing to 400 K, the AES intensity decreased continuously. This indicates that 3D-islanding occurred above 400 K. Note that Fe, Co and Ni are known not to desorb from the W(110) surface or from annealed monolayers at temperatures below 1000 K. Also, these elements have negligible solubility in W. The AES signal is never less than the AES intensity of a 1 ML film. The decrease in AES intensity is therefore due to the change in aspect ratio of the 3D islands on the annealed monolayer.

3.1.7 Other techniques

This section contains a brief description of ARAES and STM, the two techniques used to study the growth and structure of Fe/2 ML Ni/W(110). The ARAES experiments were important for determining the local fcc stacking in the Fe/Ni layers and for quantifying interdiffusion effects. STM experiments were important for determining the film morphology on larger scales (1000's of Å).

Auger electrons emitted from surface atoms have a directional dependence that contains element-specific structural information.[47] Directional contrast is due to atomic scattering of Auger electrons as they leave the surface. If an electron wave emitted from one atom is sufficiently energetic ($\geq$ 500 eV), then its scattering amplitude for scattering from a nearby atom is strongly peaked along the line joining the atoms. Forward focusing occurs because with increasing incident energy, the electron trajectory must pass closer to the nucleus to be significantly scattered. Because the scattered wave interferes with the incident wave, diffraction effects must also be considered. We refer to the technique as *angle resolved AES* (ARAES), although Auger electron diffraction and Auger electron forward focusing are employed elsewhere. If the surface is ordered, peaks in the scattering amplitude occur at directions determined by the surface structure. A simple example of this is shown in Fig. 3.12, for FCC or HCP growth in the second layer. Note that another inequivalent domain is obtained by the left-right reflection of the one shown. To first order, topmost layer atoms emitt isotropically. Emission from atoms in the layer below is strongly focused by the top atoms along the 55° and 35° directions. The main advantage of ARAES over quantitative LEED is that the results can be

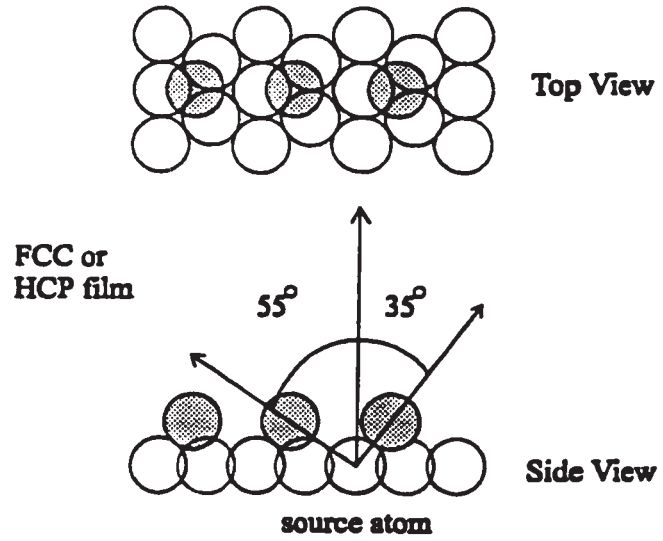

Fig. 3.12 - Auger electrons emitted from the bottom layer of a 2 ML FCC or HCP film are deflected by the atoms above them. The result is a forward-focusing of Auger electrons along the lines joining first and second layer atoms. For this film, peaks occur at 55° and 35°.

simulated within a relatively uncomplicated single-scattering formalism, as long as the films are only a few MLs thick and the Auger electrons are sufficiently energetic.

Since the results of an ARAES study are summarized in chapter 4 without the presentation of any data, a simple example is presented here. Fig. 3.13 shows the good comparison between data and theory for a 2 ML Ni /W(110) film. The data was obtained by H.L. Johnston and the electron diffraction calculation was performed by C.S. Arnold. Ni is FCC, and the scattering plane of Fig. 3.13 corresponds to that of Fig. 3.12 . Note the peaks near 55° and 35°. A detailed description of the electron scattering calculations is contained in Dr. Johnston's thesis.[40] Apart from slight shifts in the peak locations, consistent with a relaxation of the second layer away from the substrate, and a peak at low polar angles consistent with some coverage in the 3rd layer or perhaps due to second order focussing, the agreement is excellent. ARAES is most useful for identifying crystal

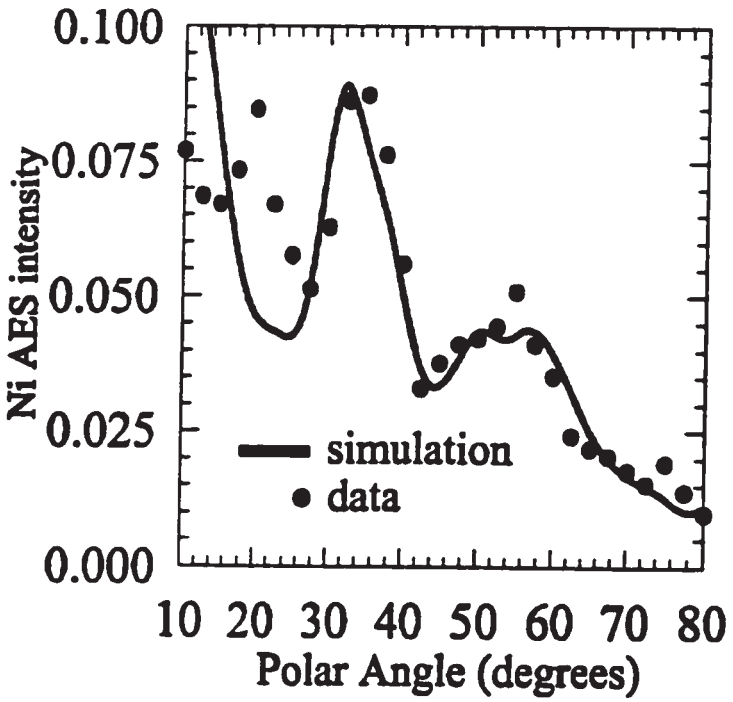

Fig. 3.13 - An angle-resolved AES scan of a 2 ML Ni film, obtained by H.L. Johnston. The direction is equivalent to that of the previous figure, although the film is not single domain. The solid line is an electron scattering calculation performed by C.S. Arnold.

structure (FCC or HCP in this case), and identifying intermixing and layer completion.

Scanning tunneling microscopy STM is now one of the most important tools in surface science.[52] Like scanning electron microscopy, STM produces a real-space image of a surface, except with much greater spatial resolution. Fig. 3.14 illustrates the operational principal of the device. A metallic tip, which is sharp on the atomic scale, is brought to within a distance d < 10 nm of the surface to be studied. If a small potential difference is applied between tip and sample, typically 10 mV - 1 V, a small current i flows between tip and sample. The current is due to the quantum mechanical tunneling through the potential energy barrier presented by the vacuum between tip and sample. Because of the exponential dependence of the tunneling current i on the tip-sample

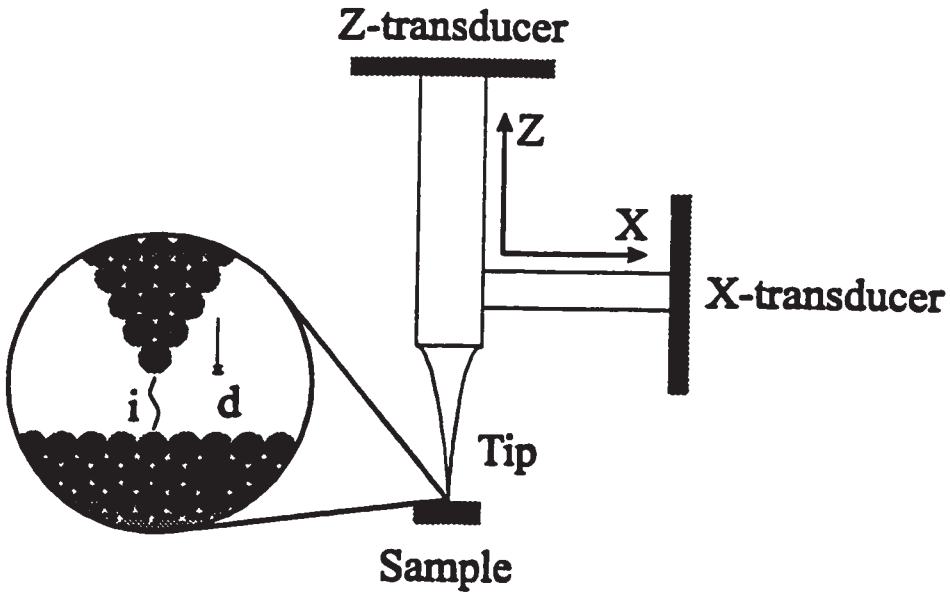

Fig. 3.14 - Scanning tunneling microscopy (STM) utilizes the quantum mechanical tunneling current between an atomically sharp tip and a sample to sense the proximity of the sample's surface. Extreme sensitivity results from the exponential dependence of the current on tip-sample separation. Piezoelectric transducers allow a rapid scanning of the surface, yielding the surface topography.

separation d, extreme positional sensitivity is achieved. Piezoelectric transducers manipulate the tip position in the X, Y (not shown) and Z directions with sub-angstrom precision. In the most common mode of operation, a constant separation d is maintained by using negative feedback on the Z-transducer to maintain a constant current i. The XY values are then rastered to scan an area and the potential applied to the Z-transducer by the feedback circuit is recorded. X, Y and Z potentials are then calibrated to give the surface height Z as a function of in-plane position X, Y. Atomic resolution is often achieved. Data obtained by C. Schmidthals and D. Venus will be presented in chapter 4 and discussed in relation to the magnetic properties of Fe/N films.

3.2 The surface magneto-optic Kerr effect (SMOKE)

The surface magneto-optic Kerr effect, which produces an optical signal proportional to magnetization, has become one of the most useful tools for the investigation of magnetism in thin and ultrathin films. Its application is responsible for significant progress in the field over the last decade,[53] especially in the areas of ultrathin film magnetic anisotropies and oscillatory exchange coupling. To a lesser degree, it has been applied to problems of magnetic ordering in 2D ultrathin film magnets. SMOKE is also technologically significant as a readout mechanism in magneto-optical drives - an application which may grow in importance in the coming years.

Although SMOKE has enormous potential for sensitivity, many experimentalists are unaware of important technical considerations for achieving a high signal-to-noise (S/N) ratio. This fact is largely due to the relatively short time that the technique has been applied to ultrathin films. For this thesis, extremely high S/N ratios were achieved. Important experimental considerations are discussed here, and some useful technical innovations are presented.

The main disadvantage of the SMOKE technique is that it does not produce measurements in absolute magnetic units. For this reason, most authors present their data in arbitrary units. This is unfortunate, since an optical calibration is straightforward and an approximate magnetic calibration is also possible. Since the technique is so new, and since uncalibrated data is usually useful, this oversight has been largely excused in the literature. In most of the experiments conducted for this thesis, polarization calibrations were conducted as thoroughly as possible.

Another consequence of the youth of SMOKE is that many obvious applications and extensions of the technique have not been developed. Measurement of the magnetic susceptibility, $\chi = \partial M/\partial H$, is one such extension. The technique is currently under development in a number of laboratories worldwide, although it is in its infancy. The development of the SMOKE susceptibility technique in our laboratory was the major technical accomplishment of this thesis.

3.2.1 Fundamental principles

The Jones-matrix formalism is very useful for describing the interaction of polarized light with matter. In the standard Jones formalism for the representation of polarized light and its interaction with optical transmitters, reflectors and absorbers, a light wave's electric field is represented by:

$$\underline{E}_k(z,t) = e^{ikz - i\omega t + \phi} \begin{bmatrix} E_x \\ E_y \end{bmatrix}, \qquad (3.1)$$

where ϕ is an absolute phase factor and the other variables have the usual meaning. The physical field is perpendicular to the z-direction and is given by the real part of 3.1. If E_x and E_y have the same complex phase, then the direction of $\underline{E}_k$ does not change in time, apart from a minus sign. $\underline{E}_k$ remains at an angle given by $\alpha = \tan^{-1}(E_y/E_x)$ and varies sinusoidally in time. This is a *linear polarization* state with azimuth α. For a fixed point z, a relative phase between E_x and E_y causes $\underline{E}_k$ to rotate with time, tracing out an ellipse. Elliptical polarization states are characterized by azimuth, which gives the orientation of the ellipse's major axis, and by the ellipticity (major axis/minor axis) of the ellipse.

Reflection from and transmission through media produce changes in polarization which are represented by matrices in the Jones formalism. A general (non-absorbing) material produces rotations in azimuth and changes the elliptical state of the incident light. These can be expressed as a complex rotation by an angle $\Phi = \theta + i\varepsilon$:

$$R(\Phi) = \begin{bmatrix} \cos(\Phi) & -\sin(\Phi) \\ \sin(\Phi) & \cos(\Phi) \end{bmatrix} \qquad (3.2)$$

$$= \begin{bmatrix} \cos(\theta) & -\sin(\theta) \\ \sin(\theta) & \cos(\theta) \end{bmatrix} \begin{bmatrix} \cosh(\varepsilon) & i\sinh(\varepsilon) \\ -i\sinh(\varepsilon) & \cosh(\varepsilon) \end{bmatrix}$$

The first matrix is a simple rotation of the electric field by θ. Operation of the second matrix on a linear state yields an elliptical state with ellipticity ε (for ε small) and does not change the azimuth. An example of the complex rotation of a linear state is illustrated in Fig. 3.15.

Reflection from a surface is usually referred to the standard polarization directions P and S where P is perpendicular to z and in the scattering plane, and S is perpendicular to both the surface normal and the scattering plane. In this notation a reflecting surface has a reflection matrix

$$\begin{bmatrix} r_{pp} & r_{ps} \\ r_{sp} & r_{ss} \end{bmatrix} . \qquad (3.3)$$

In most cases the off-diagonal components are very small or zero. S or P polarized incident light therefore retains its polarization upon reflection. Magnetic materials have small, but non-zero values of the off-diagonal components. Under these conditions, initial P-polarized light experiences a rotation upon reflection as in Eq. (3.2), giving

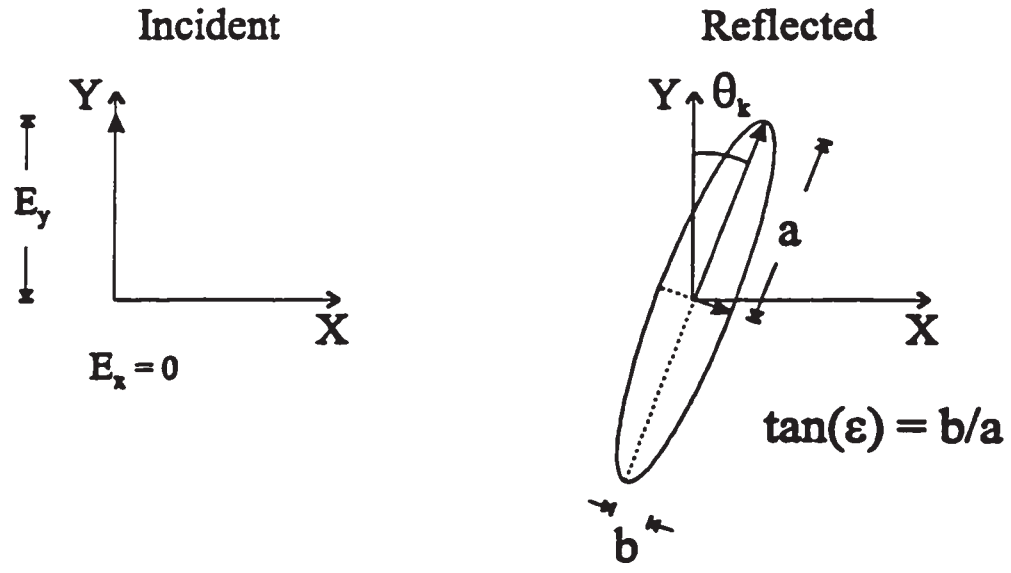

Fig. 3.15 - Light initially linearly polarized along Y is reflected into an elliptical polarization state with azimuth rotated θ from the Y axis and with ellipticity tan(ε) = b/a.

$$\theta \approx \mathrm{Re}(r_{sp}/r_{pp}) \quad \text{and} \quad \varepsilon \approx \mathrm{Im}(r_{sp}/r_{pp}) \tag{3.4}$$

This is the phenomenological origin of the Kerr effect.

Elements of the rotation matrix are determined by the dielectric constant ϵ of the material through the imposition of the boundary conditions of Maxwell's equations on the electric and magnetic fields at the material surface. In ordinary media this leads to the Fresnel reflection coefficients for r_{pp} and r_{ss}, and zero for the off-diagonal elements. Off diagonal components r_{ps} and r_{sp} are non-zero in magnetic materials because the magnetization reduces the symmetry:

$$\epsilon_M = \epsilon \begin{bmatrix} 1 & iQ & 0 \\ -iQ & 1 & 0 \\ 0 & 0 & 1 \end{bmatrix}, \tag{3.5}$$

where the magnetization is along the third vector component and Q is the Voigt

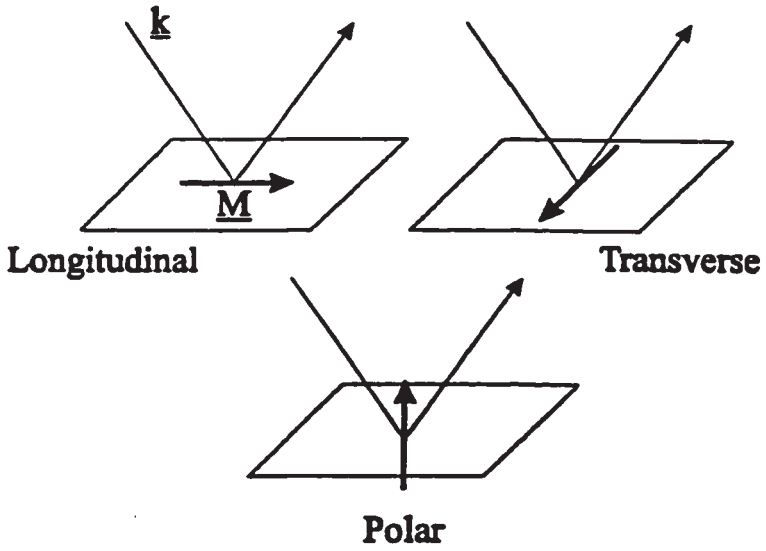

Fig. 3.16 - Three natural scattering geometries give different Kerr effects. The orientation of the magnetization M with respect to the light wavevector $\underline{k}$ and film plane determines whether the effect is longitudinal ($\underline{k} \parallel \underline{M}$), transverse ($\underline{k} \perp \underline{M}$, $\underline{M}$ in-plane) or polar ($M \perp$ film plane).

magneto-optic parameter. The eigenvectors corresponding to ϵ_M are right and left circularly polarized waves $\underline{E} = E_o(1, \pm i, 0)$ propagating along the direction of magnetization with speeds $(1 \pm Q/2)v$, where v is the speed of light in the unmagnetized medium. Materials having eigenvectors that propagate at different speeds are called *birefringent.* Because ϵ depends on the orientation of $\underline{M}$, the reflection coefficients r_{pp}, r_{ps}, r_{sp} and r_{ss} and hence the Kerr rotation, also depend on its orientation. Three natural geometries are illustrated in Fig. 3.16. In the longitudinal geometry, the moment is in-plane and in the scattering plane. In the transverse geometry, the moment is in-plane and perpendicular to $\underline{k}$. In the polar effect, the moment is perpendicular to the film.

Microscopically, dielectric birefringence in magnetic materials arises from the simultaneous presence of a net magnetic moment and spin-orbit coupling. The dielectric

constant is a measure of how an applied field separates positive and negative charge and therefore governs the speed of light in a material. A material in a light field changes its electronic charge distribution by oscillating between different electronic states through absorption and stimulated emission. In metals, the anisotropic ϵ arises from the optical conductivity σ via interband transitions. The off-diagonal part of σ, σ_{ij}, is obtained by calculating the quantum-mechanical current, or by using the Fermi golden rule:[54]

$$\sigma_{xy} = \sum_{i,f} \{ |\langle f|P_R|i\rangle|^2 - |\langle f|P_L|i\rangle|^2 \} \quad , \qquad (3.6)$$

where i and f designate initial and final electronic states, and P_R and P_L and the electric dipole operators corresponding to right and left circularly polarized light. Using a tight-binding representation, electronic states of a given wavevector k are labeled according to band index n, the orbital angular momentum l, the component of the orbital angular momentum m_l parallel to the incident light k-vector and finally the spin ($\uparrow$ or $\downarrow$). Circularly-polarized light induces transitions between states of different orbital angular momenta. The selection rules for the absorption of circularly polarized light in an electric dipole interaction (using standard notation) are $\Delta l = \pm 1$ and $\Delta m_l = -1(1)$ for right (R) and left (L) circularly polarized light. An energy level picture of one set of electric dipole transitions relevant to a 3d ferromagnet is illustrated in Fig. 3.17. In that case, the first rule is satisfied by the promotion from an d-level to a p-level, while the second rule is satisfied by the initial state having $m_l = 1$ and the final state having $m_l = 0$. On the left side of the figure, for M = 0, spin-orbit split levels are represented by an equal combination of $|3d; m_l=1; \uparrow\rangle \equiv |3d^1\uparrow\rangle$ and $|3d^{-1}\downarrow\rangle$ states for the upper level and a similar admixture of $|3d^1\downarrow\rangle$ and $|3d^{-1}\uparrow\rangle$ states for the lower level. Consider the difference in the summation of

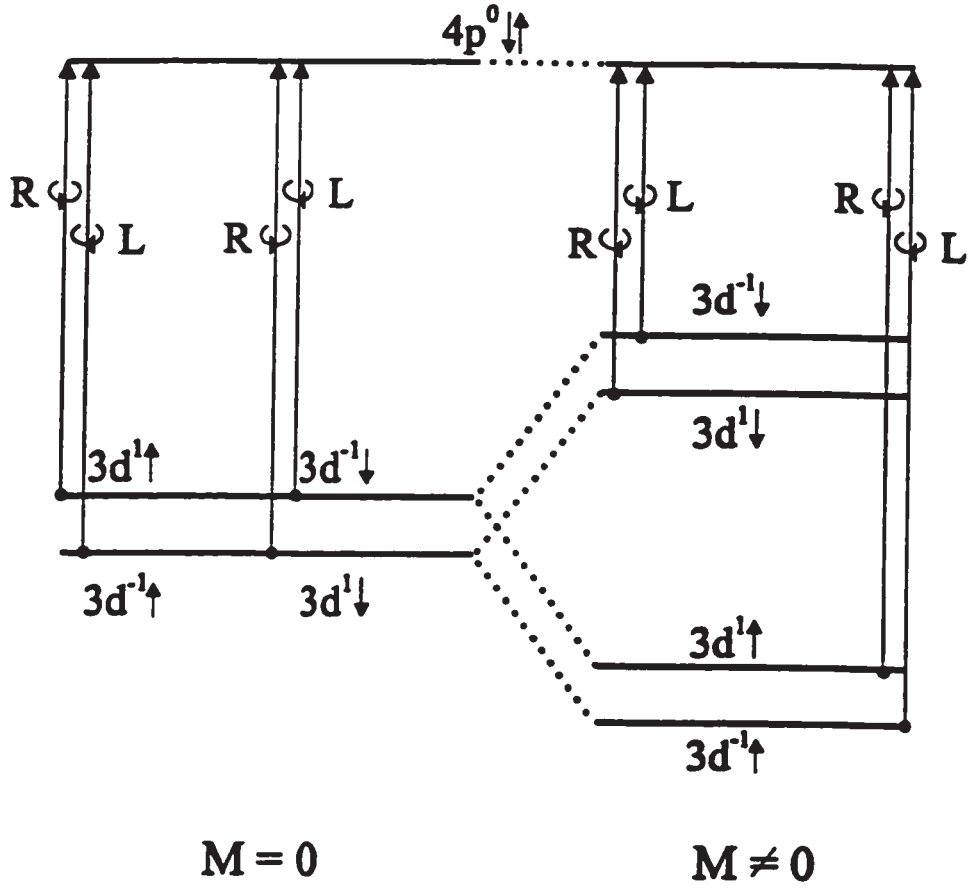

Fig. 3.17 - An atomic energy level diagram shows transitions between the 3d and 4s states, induced by left (L) and (R) circularly polarized light. On the right, only the spin-orbit splitting is present (M=0) and the matrix elements connecting the 3d and 4s levels are the same for transitions induced by L and R. Spin-splitting (M≠0) breaks the symmetry between the L and R matrix elements.

Eq. (3.6) for transitions from these levels to $|f\rangle = |4p^0 \uparrow \text{ or } \downarrow\rangle$. For M = 0 this difference is clearly zero, because $\langle f| P_L |3d^{-1} \uparrow \text{ or } \downarrow\rangle = \langle f| P_R |3d^1 \downarrow \text{ or } \uparrow\rangle$. A non-zero M is produced by an additional spin-splitting, as on the right of the figure, and results in non-zero differences in the sum (3.6). Detailed microscopic descriptions are found in the literature, although calculations for the magneto-optic properties of ultrathin films are uncommon.[54,55]

SMOKE differs from the Kerr effect because of the proximity of the substrate to the surface. Instead of imposing boundary conditions only at the surface, they must be imposed at the magnetic film/ nonmagnetic substrate as well. This considerably complicates the expressions for the rotation of the polarization. Approximate expressions for the polar and longitudinal effects are

$$\Phi_{polar} = -\frac{4\pi}{\lambda}\frac{N^2}{1-N_{sub}^2}Qt \quad and \quad \Phi_{longitudinal} = -\frac{4\pi}{\lambda}\frac{N_{sub}}{1-N_{sub}^2}\theta Qt \quad \text{s6} \qquad (3.8)$$

where N and N_{sub} are the refractive indices of the film and substrate respectively, λ is the light wavelength, t is the film thickness, θ is the (small) angle of incidence and Q is the Voigt magneto-optic parameter introduced above. Note that $\phi_{polar}/\phi_{longitudinal} = N^2/N_{sub}\theta$ which is typically greater than 10. The transverse effect (not shown) does not produce rotations as above, but does produce a difference in reflected intensity depending on the magnetization, an effect known as *magnetic dichroism.*

3.2.2 Basic measurement

The basic SMOKE measurement, using initial and analyzing optical polarizers as shown in Fig. 3.18, is made with the analyzing polarizer nearly crossed with respect to the initial polarization. If θ is the angle between the initial and analyzing polarizer axes and I_{max} is the intensity incident on the initial polarizer, then the intensity exiting the analyzer is

$$I(\theta) = I_{max}(\sin^2(\theta) + \varepsilon) \qquad (3.9)$$

where the extinction ratio ε is a measure of the polarizer's perfection. A finite ε

corresponds to an offset at $\theta = 0$ of εI_{max} and, as shall be seen, limits the sensitivity of the measurement. Fig. 3.19 demonstrates the basic method for optimizing the signal-to-noise ratio (S/N). For small rotations of the polarization Φ_K, as would be produced by SMOKE, the change in the analyzer intensity is determined by the slope at the given θ-setting

$$\delta I = 2I_{max}\sin(\theta)\cos(\theta)\,\Phi_K\,, \qquad (3.10)$$

which has a maximum at $\theta = 45°$. Since the intensity I_{max} is not perfectly stable due to a number of proportional noise sources, it is the contrast $\delta I/I$ which controls the value of θ that maximizes the S/N. The contrast is

$$\frac{\delta I}{I} = \frac{2\theta\Phi_k}{\theta^2 + \varepsilon}\,, \qquad (3.11)$$

which has a maximum at $\theta = \sqrt{\varepsilon}$, and so the extinction ratio controls the signal contrast. This setting is the standard operating point for a SMOKE measurement. A simple way to

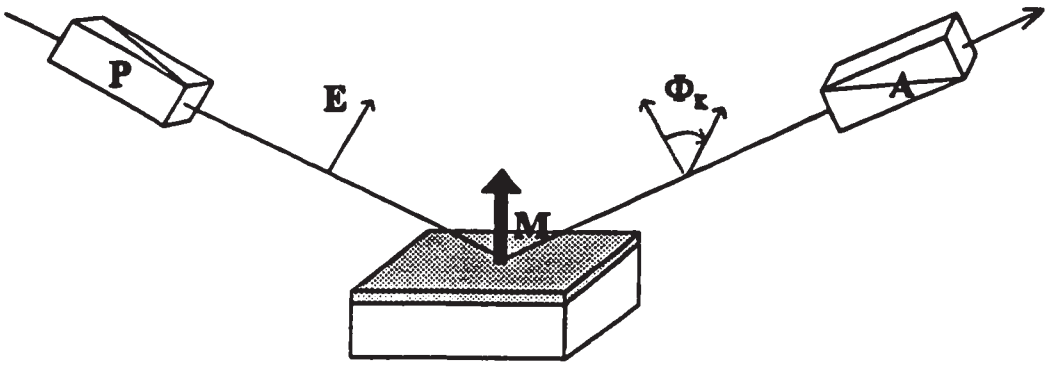

Fig. 3.18 - The basic SMOKE measurement is made using high quality polarizing crystals. An initial polarizer P prepares a highly linear initial polarization which is either S or P. Scattering from a magnetic ultrathin film produces a small polarization rotation via SMOKE. A second analyzing polarizer (or analyzer) is nearly crossed to the initial polarization. Small changes in polarization, produced by changes in M or otherwise, produce large relative changes in the transmitted intensity.

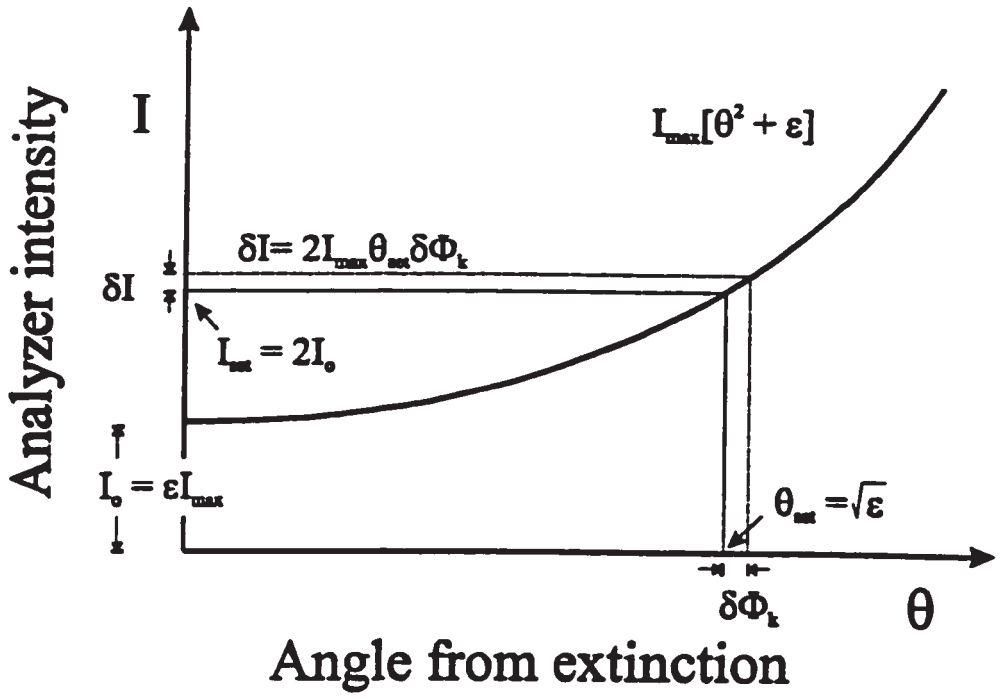

Fig. 3.19 - Near extinction, the intensity transmitted through the analyzer depends quadratically on the polarizer azimuth. A small change in polarization $\Delta\Phi_k$, due to a change in magnetization via the Kerr effect, produces an intensity change as shown in the figure. The signal contrast $\delta I/I$ is greatest when the set angle $\theta = \varepsilon^{1/2}$ is chosen.

establish the set point and measure ε is to measure $I_o \equiv I(0)$, adjust the analyzer until $I = 2\ I_o$, and use the relation

$$I(\sqrt{\varepsilon}) \equiv I_{set} = 2I_o \ . \qquad (3.12)$$

3.2.3 Window compensation

As described above, the contrast goes as $1/\sqrt{\varepsilon}$ and so reducing ε is key to improving the S/N. There are two issues which must be addressed. The first issue is the phase shift produced by the UHV optical windows. The phase shift from the windows transforms the initial linear polarization into a slightly elliptical state. This, of course, increases the effective extinction ratio of the optical system and reduces the S/N, typically by a factor of 10 to 30. Fortunately, a simple solution for this problem was developed as a part of this thesis, utilizing the phase shift from the metallic substrate. This method is 10 ~ 100 times more effective than other, more elaborate schemes described in the literature.[57] The second issue relates to the proper use of the analyzing polarizer. This information is not readily available, even from the polarizer manufacturers, and so is discussed here in detail.

The window compensation method was originally published in 1994 and is reprinted here with the permission of the editor. Some changes in notation have been made for consistency with the thesis. The paper contains a more detailed description of the apparatus, although it is still rather qualitative. This is because the apparatus is nearly as simple as the qualitative diagrams suggest. Excellent performance was achieved through matters of *procedure*, rather than elaborate apparatus. The minimum equipment requirements are discussed in the paper below. Elaboration on the subject of aperturing and collimation is provided in the section following the paper. All of the experiments, data analysis and simulations were performed by C.S. Arnold, with D. Venus playing a supervisory role. The first draft of the paper was written by C.S. Arnold, with D. Venus taking part in second and subsequent drafts.

A simple window-compensation method for improving the signal-to-noise ratio in measurements of the magneto-optic Kerr effect in ultrathin films

C. S. Arnold and D. Venus

Department of Physics and Institute for Materials Research, McMaster University, Hamilton, Ontario, L8S 4M1, Canada

Abstract

Measurements of the magnet-optical Kerr effect in magnetic ultrathin films in ultrahigh vacuum (UHV), have a signal-to-noise ratio (S/N) which is limited by the extinction ratio of the apparatus. Although polarizing crystals with excellent extinction characteristics are usually employed for *in situ* measurements of films grown in UHV, the net extinction ratio is degraded by optical windows, resulting in poor signal contrast and poor S/N. A simple procedure for canceling the effects of the windows is to slightly, but precisely, misalign the initial linear light polarization state from S or P (with respect to the sample). This technique does not require compensators or any additional optical components and is capable of an extinction ratio of 3×10^{-7}, allowing the rapid acquisition of high quality Kerr effect hysteresis loops with a very simple apparatus. The dependence of the extinction ratio on the initial light polarization is investigated and explained in terms of a Jones matrix analysis. Correcting for the windows is interpreted as a phase shift from the film substrate balancing phase shifts from the optical windows. The technique is applied to the acquisition of hysteresis loops for 4 ML Fe/W(001) films and a substantial improvement in S/N is demonstrated.

§1. Introduction

Since the pioneering work of Moog and Bader[1] nearly ten years ago, the magneto-optic Kerr effect (MOKE) has become a standard tool in the study of magnetic ultrathin films and magnetic multilayers. Magneto-optic techniques measure the change in the polarization state of linearly polarized light once it has scattered from a magnetic surface or thin film, the magnitude of the change being proportional to the magnetization. For a monolayer of a 3d ferromagnet, a rotation of the polarization vector of the order of 10^{-5} radians occurs. Rotations of this magnitude are below the range of traditional ellipsometric measurement.

A typical magneto-optic measurement is performed in UHV as follows: S or P linearly polarized laser light emerges from a Glan type polarizer, passes through an optical window and scatters from the sample. S or P initial polarizations are normally chosen because the Kerr effects for each are distinct[2] (the transverse and longitudinal effects, for example), and because only S and P polarizations are scattered from a non-magnetic metal surface without acquiring ellipticity. The reflected light passes through another (or the same) optical window, and through a second polarizer (termed the analyzer) oriented near extinction, so that only the magneto-optically rotated component of the polarization vector is transmitted. To generate a magnetic hysteresis loop, a magnetic field is applied to the sample and cycled through a range of values, so that the magnetization of the sample and transmission through the analyzer change proportionately.

To optimize the signal-to-noise ratio in the measurement, the orientation of the analyzer is chosen to maximize the relative change in the transmitted intensity when the

polarization state of the light scattered from the sample is rotated. This optimal relative response is inversely proportional to $\varepsilon^{1/2}$ where ε, the extinction ratio, is the ratio of the intensity transmitted by crossed polarizers to that transmitted by parallel polarizers.[1] Although polarizers with $\varepsilon < 10^{-6}$ are readily available, local strain in the optical windows creates birefringence and the transmitted light is elliptically polarized. The introduction of a component of the polarization vector along the minor axis of the ellipse of polarization degrades the extinction ratio of the system to typically $\varepsilon \sim 10^{-4}$. While normal incidence[3] and the use of 'strain free' windows can reduce this effect, the windows still limit the extinction ratio of the system. The resulting signal is then a small change on top of a large background, and the measurements of the Kerr effect are obscured by proportional noise sources.

In principle, averaging should allow the extraction of this small signal, but in practice a higher S/N is preferable, since it permits the short experimental times required to maintain temperature stability and cleanliness of the sample and to allow measurements during film deposition. A number of techniques can reduce the undesirable window effects and improve the extinction ratio. Moog and Bader use a Babinet compensator and report extinction ratios of order 10^{-5} using this approach.[1] They measure a change in transmitted intensity of approximately 1% for magnetic reversal in a monolayer film. Their technique also allows a separate determination of the Kerr rotation and ellipticity. Sato describes an elegant lock-in technique employing a photoelastic modulator which is effective in separating the signal from the noise,[4] and also has the advantage of measuring the magneto-optic rotation and ellipticity independently. The procedure presented here

requires no additional components and greatly improves the S/N, but does not distinguish between magneto-optic rotation and ellipticity. The important innovation is the correction for the windows by slightly, but precisely, misaligning the initial light polarization from S or P so that the ellipticity produced by scattering from the metal surface exactly cancels that produced by the windows.

§2. Apparatus and Procedure

A diagram of the apparatus is shown in Fig. 3.20. Some of the components are omitted for simplicity. Light was provided by an ordinary polarized 2 mW HeNe laser (L), with an intensity stability of ±0.2%, mounted on a small optical table which was rigidly clamped to a UHV chamber. The light was directed normally through a 45° optical port and, after scattering from the sample, the light exited through another port.

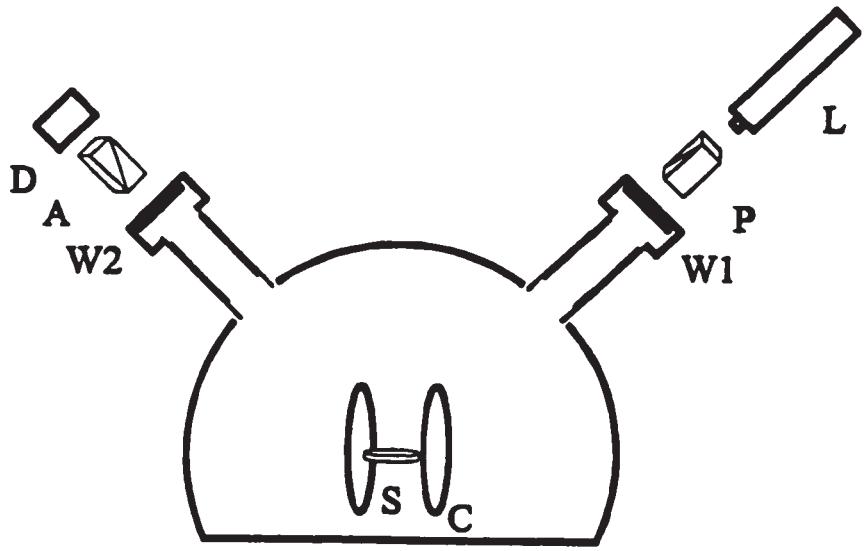

Fig. 3.20 The MOKE apparatus was built around a preexisting UHV system. Key: L - HeNe laser; P - Glan Taylor type polarizing crystal; W - ordinary quartz windows; C - Helmholtz coils with their axis in the scattering plane; S - sample; A - analyzing polarizer identical to P, D - Photodiode. P and A were mounted in rotational stages (not shown) with degree and arcminute precisions respectively.

A rotational stage with 1° precision was clamped to the flange of the entrance window (W1), and held a 5mm clear aperture Glan Taylor polarizer[5] (P) with $\varepsilon < 10^{-6}$. A higher quality rotational stage, with arcminute precision, was mounted on the exit window and held an identical (analyzing) polarizer (A). An optical head (D) with a lens, HeNe red-line 10 nm bandpass filter, photodiode and preamplifier, and adjustable apertures was mounted on a gimbal mount, which was, in turn, fixed to the rotational stage. The signal from the preamplifier was fed to a 6-pole Bessel filter with a rise time of less than 0.1 sec and to a digital-to-analog converter for computer acquisition. The windows were ordinary 2¾" MDC quartz windows.[6] A pair of Helmholtz coils (C) was mounted about the sample with the coil axis in the scattering plane for longitudinal Kerr-effect experiments. The coils were inside the chamber to avoid the Faraday effect from magnetic impurities in the windows. Films were deposited by an electron beam evaporator onto a W(001) sample (S). The UHV system and evaporator were part of a preexisting apparatus to which the MOKE apparatus was added. The MOKE apparatus was quite ordinary.

The intensity of light passing through the two polarizers obeys

$$I = I_{max} (\sin^2\theta + \varepsilon) \qquad (3.13)$$

where θ is the angle from extinction and ε is the extinction ratio. The small change in the intensity of the light transmitted by the analyzer due to a MOKE rotation is

$$\delta I/I = 2\delta\theta/\varepsilon^{1/2}, \qquad (3.14)$$

when the analyzer is set at the optimal angle $\theta = \varepsilon^{1/2}$. If there are no optical elements between the polarizers, ε is nonzero because of inefficiencies in the polarizing crystals. After the insertion of slightly birefringent optical elements, such as the windows between

the polarizers, equation (1) still holds, but the two orthogonal linear polarization components of the light undergo a relative phase shift, producing light of ellipticity e and significantly increasing the extinction ratio. In the limit of perfect polarizers, the effective extinction ratio is then given by

$$\varepsilon = \tan^2 e, \qquad (3.15)$$

The goal of compensation is to introduce additional phase shifts which cancel those produced by the windows, so that the ellipticity produced by the overall optical path vanishes. Based on the Fresnel reflection coefficients, no ellipticity is expected for the reflection of light which is S or P polarized with respect to the sample, since these are the eigenpolarizations for reflections. Nearly all other initial linear polarizations undergo phase shifts upon reflection and are scattered into elliptical polarization states. By choosing particular initial polarizations which are slightly displaced from S or P, the window phase shifts can be compensated by the sample phase shifts.

In the experiments, the compensation condition is found by a slight adjustment of the initial polarizer angle. The initial polarizer is first set to either S or P, depending on the experiment, and the analyzing polarizer is set to extinction and the extinction ratio is measured. The initial polarizer angle is then changed by a few tenths of a degree, and the analyzer is reset for extinction. If the extinction ratio improves, the process is repeated. If it degrades, the rotation is made in the opposite sense. Iteration continues until a minimum is found in the extinction ratio. At this stage in the procedure, ε is limited by the diffuse glow from the scattered light in the analyzer. Apertures prevent most of this glow from entering the detector. The lowest extinction ratios are obtained with an aperture

diameter of ~ 0.3mm, but these are difficult to position without producing noise due to the movement of the light beam introduced by vibrations of the sample. For a small price in extinction ratio, a larger aperture of 1mm diameter is found to introduce negligible vibrational noise. A fine tuning of the initial polarizer angle is required every time the sample holder is moved or laser orientation is changed, since the angles and points of incidence with the windows also changes. The correction is usually only a fraction of a degree and is performed in a few minutes.

§3. Demonstration of the Technique

The extinction ratio was measured for various settings of the initial polarizer angle and is plotted as the points in Fig. 3.21. A range of 180° is sufficient because of twofold symmetry. The origin of the initial polarizer angle coincides with S polarized light. Minima are located at 5° and 95° and maxima at 41° and 144°; ε ranged from 10^{-6} to 6 x 10^{-3}. Note that the two peaks have different heights and that the two half-widths within each peak are different. Fig. 3.22 shows another data set in close proximity to the minimum near S polarization. Extra precision for this measurement was gained by fixing a mirror on the rotational stage of the initial polarizer, and reflecting a laser from it to a scale on a wall 4m away. The extinction ratio was less than 10^{-6} over a range of 1° in the polarizer performance of the polarizers alone and demonstrates the effectiveness of the correction technique.

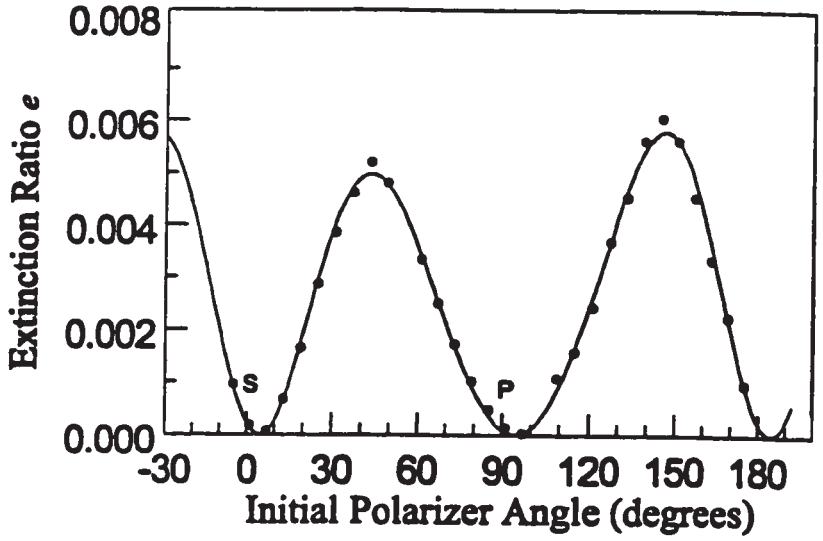

Fig. 3.21 The extinction ratio ε was measured as a function of initial polarizer angle over a range of 180°. Minima occurred at 5° from S and P polarizations, rather than at S and P. The curve was a least-squares fit based on a Jones matrix analysis which considered window ellipticity ϵ, azimuth θ and retardance δ, and Fresnel reflection from the tungsten substrate. Minima occurred for initial polarizer angles such that phase shifts from the substrate compensated the windows.

The technique can be understood quantitatively using the Jones matrix formalism.[7] A Jones vector contains two complex components which together describe the two degrees of freedom of the polarization state (azimuth and ellipticity) as well as the temporal phase and amplitude of the light field. Optical elements are represented by 2 x 2 matrices which describe the dichroic and birefringent properties of the element and the overall attenuation and phase shift. An optical path comprised of several components is represented by the product of the individual matrices and the product matrix connects the initial and final Jones vectors. The eigenpolarizations of an optical element are special in that they pass through with the same azimuth θ' and ellipticity ϵ. All other polarizations are changed upon transmission through the element because of a relative phase shift δ between the two eigenpolarizations into which the arbitrary light state is decomposed.

Linear S or P polarized light states passing through a window are unlikely to be eigenpolarizations, and so they acquire ellipticity. The compensation procedure amounts to finding an initial linear polarization which is special in that it transforms from one linear state to another linear state when passing through the entire optical system, yielding no contribution to ε from ellipticity.

The fitted curve of Fig. 3.21 was obtained from a Jones-matrix analysis. Although the real optical path is described by $\mathbf{T}_1\mathbf{R}_w\mathbf{T}_2$, where $\mathbf{T}_1$ and $\mathbf{T}_2$ are the window Jones matrices and $\mathbf{R}_w$ is the Fresnel reflection matrix for tungsten at 6328Å, an equivalent optical path is described by $\mathbf{T}_{eff}\mathbf{R}_w$, where

$$\mathbf{T}_{eff} = \mathbf{T}_1 (\mathbf{R}_w\mathbf{T}_2\mathbf{R}_w^{-1}). \qquad (16)$$

Essentially, (4) states that combined rather than individual window effects are important. Then the input and output Jones vectors, $\mathbf{E}_i$ and $\mathbf{E}_o$ respectively, are given by

$$\mathbf{E}_o = \mathbf{T}_{eff}\mathbf{R}_w\mathbf{E}_i \qquad (17)$$

Equation (5) was evaluated for the linear polarizations $\mathbf{E}_i$ corresponding to the data points, and equation (3) was used to obtain the extinction ratio from the ellipticity of the output light vector $\mathbf{E}_o$. Values for the retardance δ, ellipticity ϵ and azimuth θ' of the effective window were obtained from a least squares fit. No scaling factor was used. The curve of Fig. 3.21 corresponds to the effective window parameters of $\delta = 3.2°$, $\epsilon = -0.33°$ and $\theta' = 77°$, which are consistent with the expectation of a small effect. At S or P polarization, the calculated extinction ratio was 10^{-4}, but at the minima at 5° and 95° respectively, the fit was zero. This is due to a zero-crossing in the ellipticity as a function of initial polarization angle at the compensation point. Note how the fitted curve reproduces the

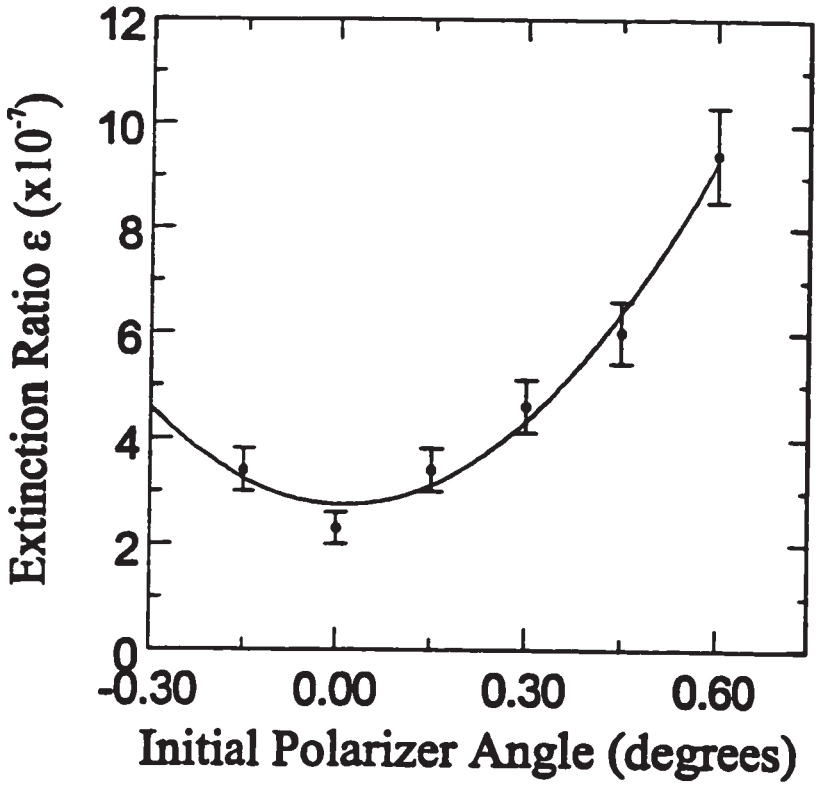

Fig. 3.22 The minimum near P initial polarization was investigated at higher resolution for conditions similar to those of Fig. 3.21. The angle measurements are relative to the minimum rather than to S or P polarizations. ε was less than 10^{-6} over a range of approximately 1° and reached a minimum value of 2×10^{-7}. At the minima, polarizing crystals limited the extinction ratio.

absolute scale, locations of maxima and minima, and half-widths of ε. The obvious goodness of fit of the curve in Fig. 3.21 and the extremely low value of ε achieved in Fig. 3.22 indicate that the windows were completely compensated and ε was determined by polarizer quality alone.

The technique was applied to the measurement of hysteresis curves for a 4 ML Fe/W(001) film, using the longitudinal Kerr effect. The field was applied along the (10) direction, the easy axis for this system.[8] The loops are shown in Fig. 3.23, each normalized to the average intensity of the loop. The extinction ratio for the

uncompensated curves in (a) and (b) was ~ 10^{-4}. Fig. 3.23 (a) was a single loop of 200 points obtained in 18 seconds. The loop was completely obscured by the noise, which was ±0.2% peak-to peak. Averaging ten such loops revealed magnetic hysteresis of ±0.3% of the total intensity, as shown in Fig. (b). With no window compensation, this MOKE signal strength is typical of magnetic films of this thickness. Fig. 3.23 (c) is a single loop acquired under the same conditions as in (a), but with compensation and an extinction ratio of ~10^{-6}. The signal-to-noise shows a dramatic improvement from. (a) because of a reduction in the strength of the background intensity. An average of ten such loops, in (d), shows a switching of ±4.5%.

The improvement in S/N demonstrated in Fig. 3.23 does not represent the full potential of this technique. The loops acquired without compensation are dominated by proportional noise with a flat power spectrum. Compensation increases the signal to such an extent that this noise is not readily visible in Fig. 3.23 (c). The noise which now dominates has a power spectrum which is measured to vary as 1/f, consistent with the low frequency components seen in the data. We believe that the 1/f noise derives from some mechanism which surface roughness converts to fluctuations in the scattered light polarization. This hypothesis is supported by three observations. First, the substrate has acquired scratches, which are obvious to the eye, due to handling since it was polished. Second, in some experiments it was possible to translate the sample to find a scattering geometry where the 1/f noise disappeared. These atypical conditions allowed the acquisition of very high quality hysteresis loops. Loops of 200 points obtained in 18 seconds from a similar 4 ML Fe/W(001) film yielded a MOKE signal of ±6% with a noise

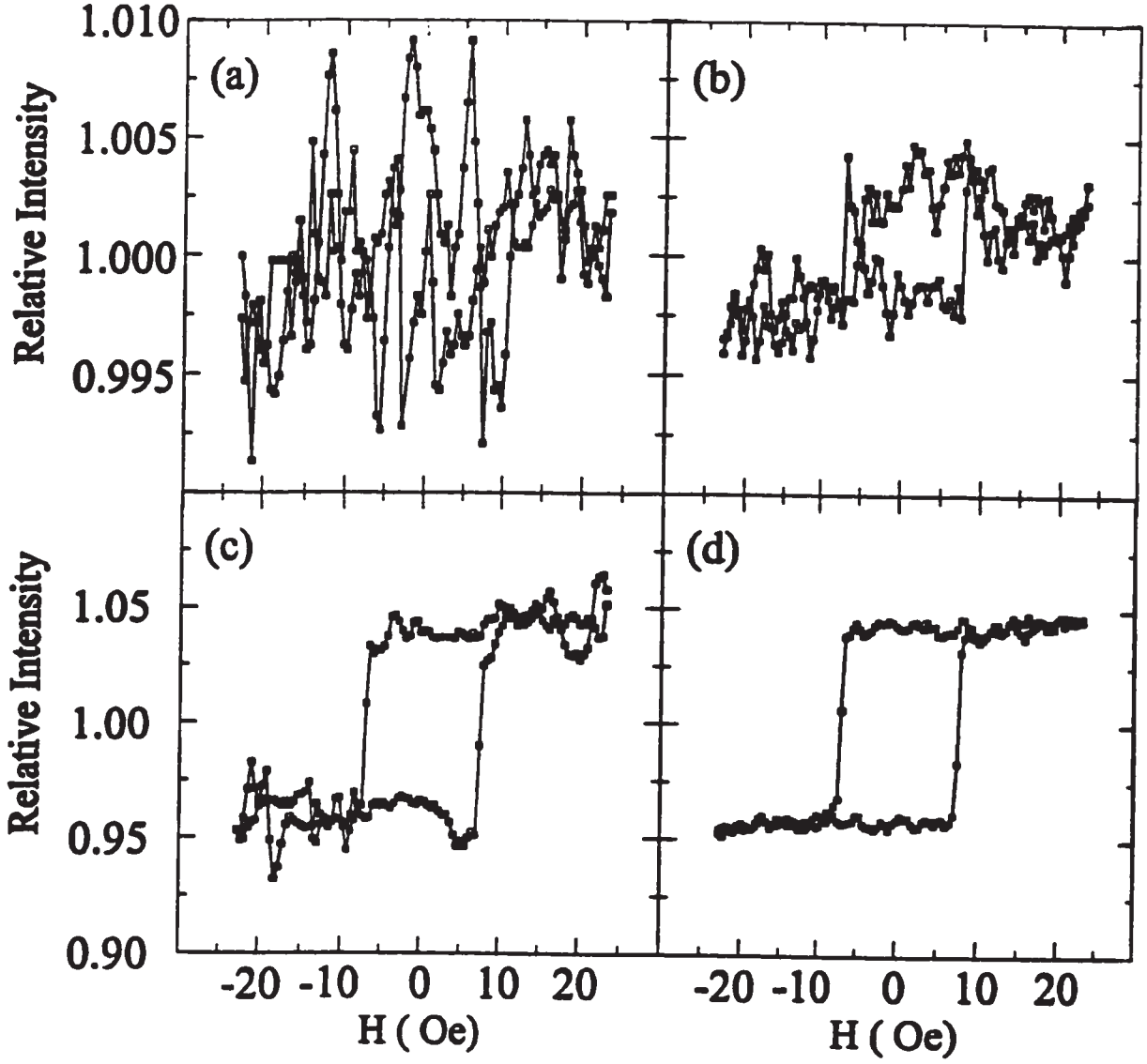

Fig. 3.23 A comparison of longitudinal hysteresis loops for 2 ML Fe/W(001) with H along (10) was made, with and without compensation. (a) For P polarized light the extinction ratio was ~ 10^{-4} and a single Kerr loops were completely obscured by noise. (b) After compensation, with $\varepsilon \sim 10^{-6}$, the loop was clearly visible. (c) and (d) are each averages of 10 loops which were obtained under the same conditions as (a) and (b) respectively, demonstrating an improvement in S/N through compensation of approximately a factor 10.

level of ±0.2%, which is equivalent to the intensity stability of the laser. Third, polarization noise would introduce noise directly into the Kerr signal. Since it would also scale as $\varepsilon^{-1/4}$, it would ultimately dominate the noise.

References

1. E. R. Moog and S. D. Bader, Superlattices and Microstructures 1 (1985) 543.

2. C. Daboo, J. A. Bland, R. J. Hicken, A. J. R. Ives and M. J. Baird, Phys. Rev. B 47 (1992) 11852.

3. J. -P. Qian and G. C. Wang, J. Vac. Sci. Technol. A 8 (1990) 4117.

4. Katsuaki Sato, Jap. J. Appl. Phys. 20 (1981) 2403.

5. Part #MGT25E, Karl Lambrect Corp., 4204N Lincoln Ave., Chicago IL, 60618 USA.

6. Part # 450020, MDC Vacuum Products Corp.23842 Cabot Blvd., Hayward CA, 94545-1651 USA.

7. R. M. A. Azzam and N. M. Bashara, Ellipsometry and Polarized Light (North-Holland, NY, 1977).

8. T. L. Jones and D. Venus, Surf. Sci. 302 (1994) 126; D. Venus and H. L. Johnston, Phys. Rev. B, 50 (1994) 15 787.

3.2.4 The proper use of polarizing crystals: collimation and apertures

In the previous section, a technique for counteracting the increase in extinction ratio due to window phase shift was presented. After performing the compensation procedure, the extinction ratio may be limited unnecessarily by diffuse scattering in and after the analyzing crystal. Without addressing this issue, ε is typically limited to 10^{-4}. This section is devoted to a more detailed description of the origin and solution to this problem than was offered in the previous section.

The operation of the Glan type polarizing crystal is demonstrated in Fig. 3.24 (b). The crystal is actually composed of two separate calcite prisms of high purity. The two hypotenuses are butted together as shown, with only a small air gap between them. Elliptically polarized light enters the polarizing crystal from the left and is incident on the interface between the two prisms. The hypotenuse angle is chosen at Brewster's angle for HeNe red-line light *in* calcite. As a result, the component of the polarization parallel to the scattering plane experiences total internal reflection (TIR), while the perpendicular component is partially transmitted. When using this type of crystal as an analyzing crystal set near extinction, almost all of the incident light intensity is therefore in the TIR component. Ideally, the TIR component terminates and does not reach the exit face on the right of the crystal. Some effort is made to ensure this. The crystal, other than the entrance and exit faces, is embedded in epoxy which is index matched to calcite and the epoxy itself is contained in a black, absorbing holder. These measures are only partially effective, however, and a fraction of the TIR component is reflected as shown at the top face of the crystal in the figure. This reflected component forms a bright lobe which is

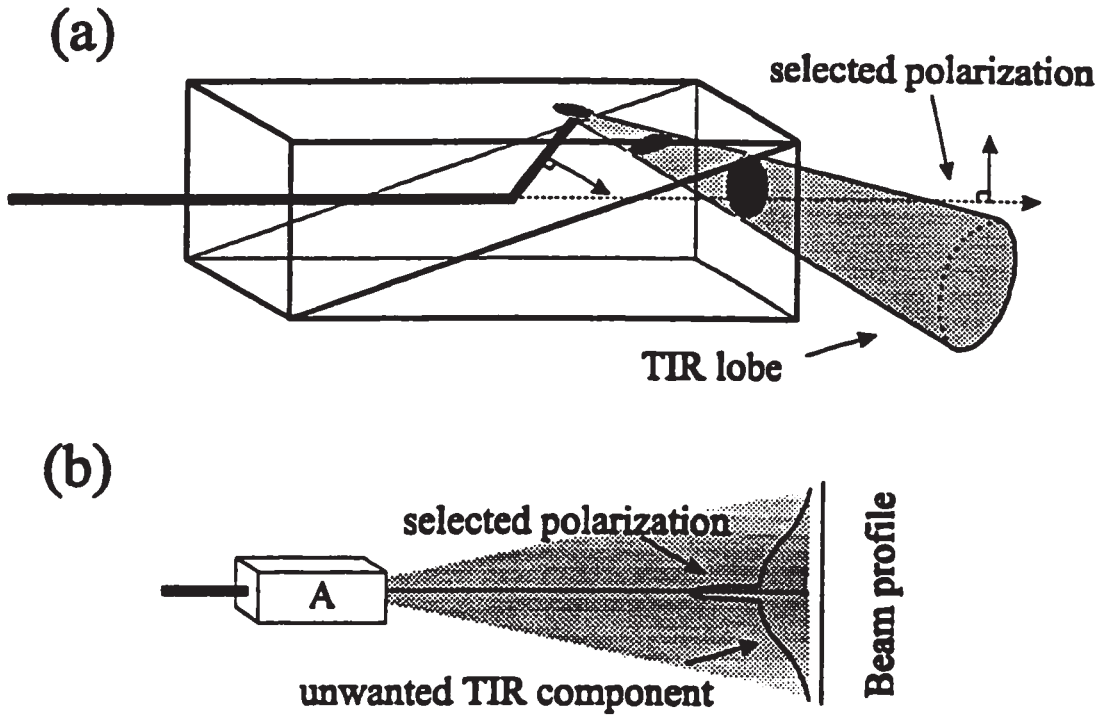

Fig. 3.24 - (a) Glan type polarizers separate polarizations by total internal reflection of one (TIR) component and partial transmission of the other (selected) component. The TIR component scatters inside the crystal and exits at an oblique angle. Multiple and diffuse scattering of this component within the crystal produce a TIR 'glow'. (b) At extinction, the light transmitted by the analyzing polarizer A has two components: the selected polarization, which has a very narrow profile and quadratic dependence on the angle from extinction, and a broad contribution from the totally-internally reflected (TIR) component which is nearly independent of the analyzer setting.

easily visible with the room lights off. The crystal dimensions are such that the lobe leaves the exit face at a strongly oblique angle. By collimating the exit light over a sufficient distance and coating any nearby surfaces with a black, absorbing carbon film, this component is completely eliminated.

Multiple and diffuse scattering of the TIR component within the crystal, leads to a

broad contribution to the transmitted intensity, as shown in Fig. 3.24 (b). The selected component is narrowly defined and quadratically dependent on the angle from extinction as described above. The broad TIR contribution does not vary near extinction, producing an offset in the $I(\theta)$ characteristic and contributing to ε. The selected component is typically less than 1 mm in diameter, and so all but this region is rejected with apertures. With apertures of 0.1 mm^2 or less extinction ratios of 3×10^{-7} are routinely achieved.

3.2.5 Performance

The performance of the SMOKE apparatus constructed for this thesis is demonstrated in Fig. 3.25. Fig. 3.25 (a) shows the parabolic dependence of $I(\theta)$ near extinction and the exploded view reveals the offset due to a finite ε, which was 1.7×10^{-6} as determined from the fit using $I_{max} = 8.6 \times 10^{-3}$. The form of Eq. (3.10) is well obeyed by the measured contrast for a 5 μradian displacement, as shown by the fit in Fig. 3.25 (b). The peak contrast is at $\theta \approx 1.2$ μradian in good agreement with the measured ε. Having established the set-point of the analyzer, a SMOKE measurement requires only the measurement of I as the magnetic field applied to the film is varied. Calibration of the magnitude of the SMOKE rotation Φ_k is achieved by consistent application of Eq. (3.11) and measurement of ε. Fig. 3.26 is a SMOKE hysteresis loop obtained from a 4 ML bcc Fe film grown on the (001) face of a tungsten single crystal. The contrast $\delta I/I$ is +/-0.06 at an extinction ratio of 3×10^{-7}, yielding a magneto-optic rotation of +/- 16 μradians.

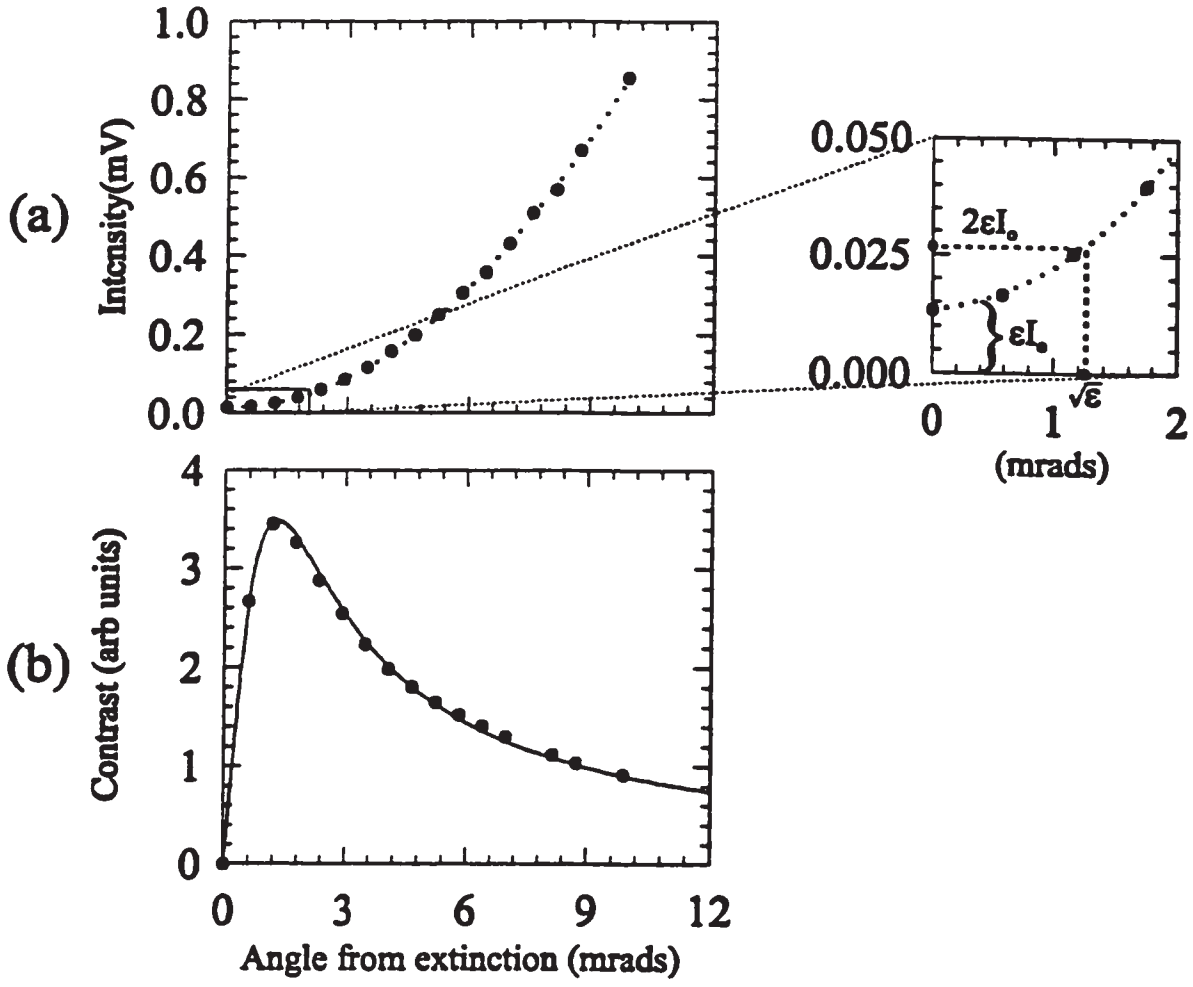

Fig. 3.25 - The SMOKE apparatus performance characteristics using 1 mm^2 apertures. Graph (a) shows the expected quadratic dependence of the analyzer intensity on the angle from extinction. The exploded view reveals an offset at the extinction point due to the finite extinction ratio ε. Graph (b) demonstrates that the contrast is maximized at 1.3 mradians from extinction, giving $\varepsilon = 1.6 \times 10^{-6}$.

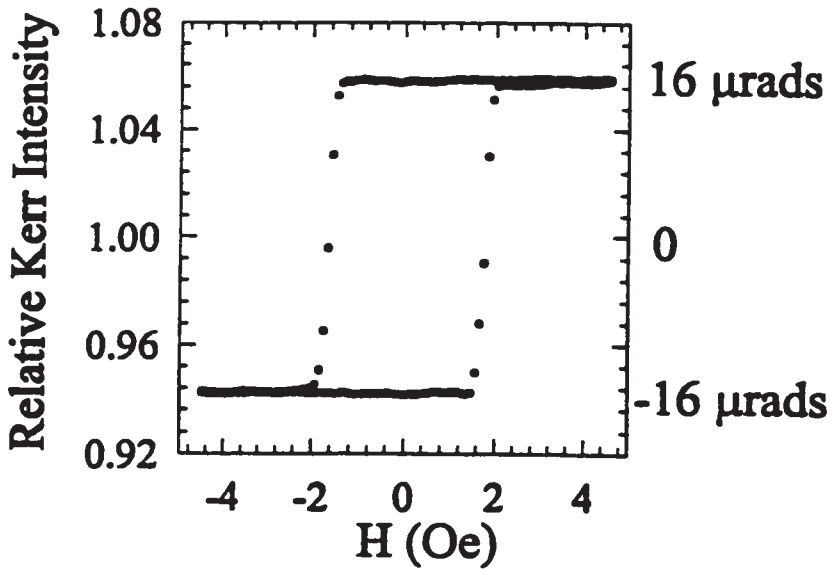

Fig. 3.26 - A Kerr loop obtained from a 4 ML Fe/W(001) ultrathin film. As indicated by the left vertical scale, the analyzer intensity switched between +/- 6% of the average transmitted laser intensity. The right hand scale, in angular units, is calibrated from the measured extinction ratio $\varepsilon = 3 \times 10^{-7}$.

3.2.6 SMOKE susceptibility measurements

The following paper is an early draft of a paper submitted to The Review of Scientific Instruments. M. Dunlavy assisted C. S. Arnold in the experiments presented. D. Venus played a supervisory role during the development of the technique. The analysis and this draft are the work of C.S. Arnold. At the time of the submission of this thesis, the latest version of this paper was in peer review.

Magnetic susceptibility measurements of ultrathin film structures using the surface magneto-optic Kerr effect: optimization of the signal-to-noise ratio

C. S. Arnold, M. Dunlavy and D. Venus

Department of Physics and Astronomy and Brockhouse Institute for Materials Research, McMaster University, 1280 Main St. West, Hamilton ON, Canada L8S 4M1

Most experimental investigations of ultrathin film magnetism via the surface magneto-optic Kerr effect (SMOKE) have relied on measurements of the magnetization in a static magnetic field. There are many ultrathin film systems in which useful magnetic information can be extracted from a measurement of the Ac susceptibility, although it is rarely measured. This is unfortunate since the susceptibility is a more appropriate probe of the magnetism in some cases and since enormous gains in signal-to-noise ratio (S/N) are achieved through lock-in detection of the SMOKE signal response to an Ac modulated field. The technique is described, with emphasis on signal-to-noise considerations. The sensitivity of the technique is demonstrated with an example of the in-plane, order-disorder transition in a 1.2 ML Fe/ 1 ML Ni/W(110) film.

1. Introduction

During the past decade, substantial progress has been made in the area of magnetic ultrathin film structures. One particularly useful technique has been the surface magneto-optic Kerr effect (SMOKE). It has contributed to the understanding of ultrathin film magnetic anisotropies,[1] oscillatory exchange coupling,[2] critical phenomena[3] and spin-

reorientation[4], as well as in other areas. The main reasons for the popularity of the technique are the ease of implementation and high sensitivity.[5]

In most cases, a signal proportional to the static magnetization is measured. This measurement is often called dc-MOKE. In a few cases, the magnetic susceptibility has been measured via SMOKE (ac-MOKE), which measures the linear response of the magnetization in an applied field.[6-8] Application of SMOKE to the ac-susceptibility is a natural experimental progression. There are many physical problems of interest in which the susceptibility is a more convenient and natural parameter to employ than the static magnetization. Examples of such problems are order-disorder[7] and spin-reorientation[8] transitions where the remanent magnetization vanishes while the susceptibility is finite or even large. In these cases, large SMOKE signals are obtained using small applied fields. The technique is therefore useful in setups with limited magnetic field capability. Furthermore, lock-in amplification provides an enormous benefit in signal-to-noise ratio, allowing for the acquisition of SMOKE rotations that are very small compared to the limits of dc-MOKE.[7,8]

Although the implementation of ac modulation to SMOKE in ultrathin films is relatively straightforward, there are some differences in signal optimization as compared to dc-MOKE. This article describes an implementation of the ac-MOKE method with an emphasis on the optimization of the S/N. A measurement of the magnetic susceptibility of a 1.2 ML Fe/ 2 ML Ni/W(110) film demonstrates the extreme sensitivity of the technique.

2. Noise considerations

The SMOKE apparatus[9] and sample holder[10] were described previously. Recent modifications to the sample holder allow for cooling to 200 K and for the application of perpendicular and in plane magnetic fields to the sample. Fig. 3.27 highlights the electronics modifications required to convert the dc-MOKE system to an ac-MOKE system. In the original setup, linearly polarized laser light scatters from the magnetic film and experiences a SMOKE rotation of its polarization state which is proportional to the magnetization. An analyzing polarizer set to an angle θ from extinction converts

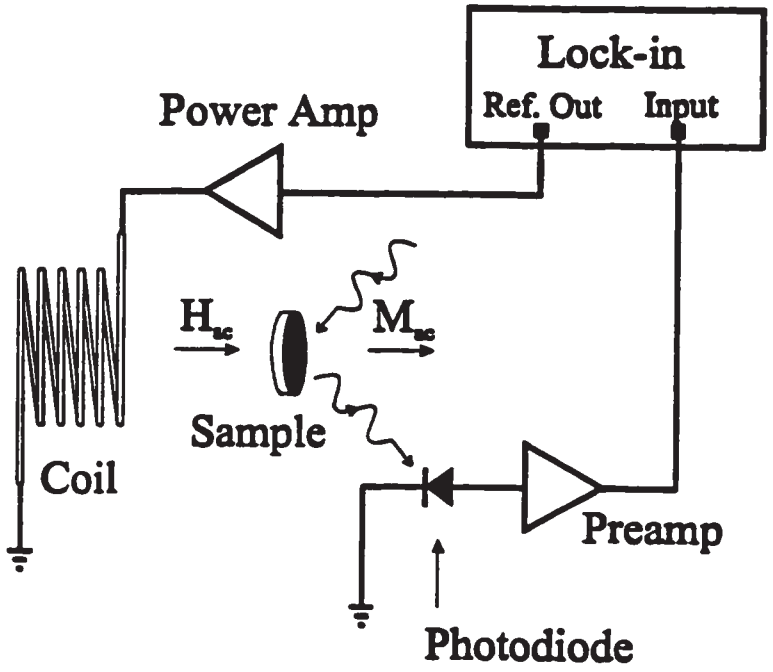

Fig. 3.27 The electrical connections employed for the modification of a dc-MOKE setup to ac-MOKE. The lock-in provides a reference signal which is buffered by a power amplifier, producing an ac applied field H_{ac}. Assuming a finite χ, a modulation M_{ac} is present. This is converted to a polarization modulation by SMOKE and then to an intensity modulation at the detector by standard dc-MOKE optics (not shown). sample, producing a field H_{ac}. This produces an ac response in the magnetization $M_{ac} = \chi H_{ac}$, where χ is the external magnetic susceptibility.

polarization changes to changes in light intensity falling on a photodiode. In the ac-modified setup, a sinusoidal reference signal is buffered by a power amplifier which supplies a magnetic coil near the sample. Then an ac modulation Φ_{ac} in the polarization angle is present, due to SMOKE, leading to an ac component in the intensity transmitted by the analyzing polarizer. For small θ, the dc intensity at the detector is

$$I(\theta) = I_{max}(\theta^2 + \varepsilon) , \qquad (3.18)$$

where I_{max} is the transmitted intensity when the analyzing polarizer has its axis parallel to the incident polarization and ε is the extinction ratio. For small θ and small Φ_{ac}, the ac component S in the transmitted intensity is proportional to the slope of Eq. (3.18) at the set-point θ_{set}

$$S = 2 I_{max} \Phi_{ac} \theta_{set} . \qquad (3.19)$$

Besides detector noise, two sources of noise enter into ac-MOKE measurements. Fluctuations in the dc level of the laser on the detector δI occur via fluctuations in the parameters I_{max}, and θ ε of Eq. (3.18), and those frequency components within $1/\tau$ (τ is the lock-in time constant) of the modulation frequency produce noise in the lock-in signal. In principle, a second way in which the noise can contribute is on the modulation itself via fluctuations in I_{max} and θ_{set} in Eq. (3.19), producing noise Δi within a bandwidth $1/\tau$ of dc. We find that those noise sources are orders of magnitude weaker than the first type of contributions. Only fluctuations δI in Eq. (3.18) are considered here. Fluctuations in I_{max} scale the entire $I(\theta)$ function changing the dc intensity, producing fluctuations δI_I. Similarly, fluctuations in the azimuth θ, due to vibrations in the sample holder, for example, produce fluctuations δI_θ. In dc-SMOKE applications detector noise δI_D is

usually not a factor and a good quality photodiode will not contribute to the noise, but in ac-SMOKE it may play a role because the other noise terms are dramatically reduced by lock-in detection. Background room light does not appear to contribute substantially to this term, probably because a HeNe 6328 Å line filter over the photodetector dramatically reduces stray light. Using Eq. (3.18), the various noise sources at the modulation frequency ω are:

$$\delta I_I = I_{max}(\theta^2 + \varepsilon)\, f_I(\omega)/\sqrt{\tau}, \qquad (3.20)$$

$$\delta I_\theta = 2\, I_{max}\, \theta\, \delta\theta(\omega)/\sqrt{\tau},$$

$$\delta I_D = N_D/\sqrt{\tau}\,.$$

Intensity noise is proportional to Eq. (3.18), giving a fraction $f_I(\omega)$ per $Hz^{1/2}$. Azimuthal fluctuations $\delta\theta(\omega)$ are absolute, rather than proportional to θ. Detector noise δI_D is a constant, independent of I_{max} and θ. It results from the resistances of the photodiode (60 MΩ) and gain resistor (100 MΩ) of the current-to-voltage converter. After the gain of 10^8 V/A, the total Johnson noise is 1.2 μV $(Hz)^{-1/2}$. Although some correlation may exist in δI_I and δI_θ, due to a vibration for example, they will be treated as statistically independent for simplicity. Summing terms in eqs. (3.20) in quadrature and grouping according to θ-dependence, the S/N is

$$S/N(\theta) = \frac{2\,\Phi_{ac}\,\theta\,\tau^{1/2}}{(A\theta^4 + B\theta^2 + C)^{1/2}} \qquad (3.21)$$

where

$$A = f_I(\omega)^2\,,$$

$$B = 2\varepsilon\, f_I(\omega)^2 + (2\delta\theta(\omega))^2\,, \qquad (3.22)$$

$$C = N_D^2/I_{max}^2 + (\varepsilon\, f_I(\omega))^2\,.$$

For $\theta \sim 0$, the divergence of S/N(θ) is limited by *C*. The S/N has a maximum at $\theta_m^4 = C/A$ and B contributes at intermediate θ values. In most discussions of dc-SMOKE, only the intensity noise terms are considered. Considering only the intensity terms here, the S/N maximum is given by the same condition as for dc-SMOKE $\theta_m = \sqrt{\varepsilon}$.[5] As is shown below, the experimental value of θ_m in ac-SMOKE is substantially greater than $\sqrt{\varepsilon}$ for our system.

Using a 0.8 ML Fe/2 ML Ni/W(110) film as a test study, the S/N(θ) characteristic was measured and is plotted in Fig. 3.28. In this range of coverage the film moment is perpendicular to the surface so the measurement was made by polar SMOKE. The susceptibility *vs.* temperature curve is very broad and was useful for measuring S/N(θ) because it was relatively easy to maintain a constant Φ_{ac}. Φ_{ac} was determined from (3.19) to be 4.6×10^{-6} radians. The magnitude of this rotation is somewhat smaller than would be produced by longitudinal SMOKE from 1 ML Fe, or more than an order of magnitude smaller than would be produced by the magnetization reversal of 1 ML of Fe as observed in the polar effect. A frequency of 210 Hz was chosen as the highest frequency below the cutoff of the photodetector electronic which was between harmonics of the line frequency. A relatively high frequency was desired in order to avoid observed $1/\omega$ type noise sources. Intensities *I* and *i* are measured in volts and conversion to power is performed using the photodiode's responsivity ~0.3 A/W and the gain 10^8 of the current-to-voltage converter. A lock-in time constant of 1 sec was employed. From the I(θ) characteristic Eq. (3.18), the dc parameters $I_{max} = 8.6 \times 10^3$ and $\varepsilon = 1.7 \times 10^{-6}$ were obtained.

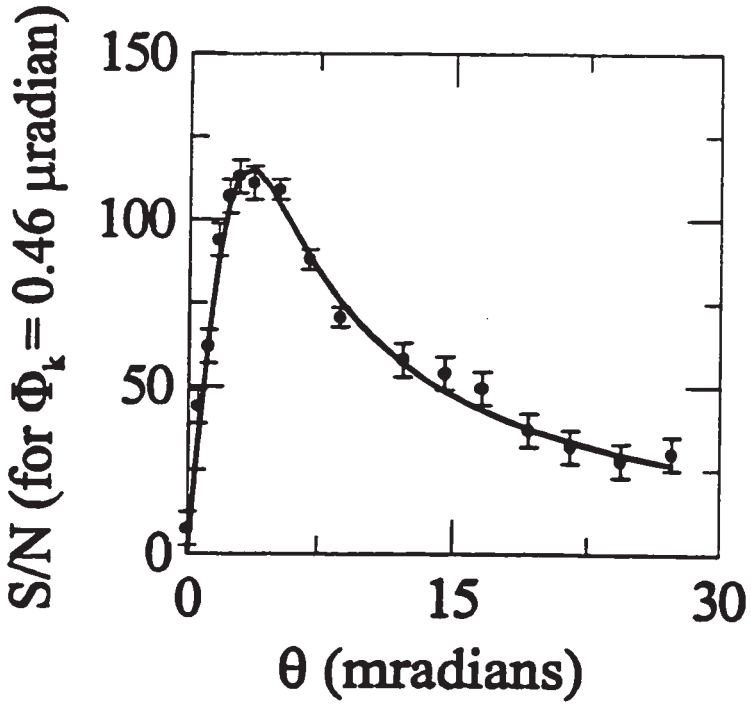

Fig. 3.28 - The measured S/N ratio as a function of analyzer setting for a 0.46 μradian polarization modulation induced by SMOKE in a 0.8 ML Fe/2 ML Ni/W(110) film. The maximum at θ = 3.5 mradians is determined by the intensity and detector noise sources.

The S/N(θ) characteristic differs from that of dc-SMOKE in two regards. Firstly, the magnitude of the S/N is much greater for ac-SMOKE because the proportional and azimuthal noise terms are much greater near dc than at the modulation frequency. In our system, the ac-SMOKE S/N is at least a few hundred times greater for ac-SMOKE than for dc-SMOKE.[9] A second difference is that θ_m = 3.5 mradians rather than $\sqrt{\varepsilon}$ = 1.3 mradians. The solid line of Fig. 3.28 is a fit of Eq. (3.21) using $A = 1.8 \times 10^{-10}$, $B = 2.8 \times 10^{-15}$ and $C = 2.6 \times 10^{-20}$, all in units of Hz^{-1}. A was fit by ignoring B and C for large θ, where the θ^4 term dominates. C was then determined by observing θ_m = 3.5 mradians and using $C = A\ \theta_m^4$. Finally, B was adjusted to minimize the least-squares error of the fit to

the data. From *A*, $f_I(\omega) = 1.3 \times 10^{-5}$, which is a few orders of magnitude smaller than the observed stability near dc. The first term of B in (3.22) is too small to account for the observed size of *B*, therefore giving $\delta\theta(\omega) \approx 24$ nradians/(Hz)$^{1/2}$. Again, this term is nearly two orders of magnitude smaller than that observed in this setup near dc. This term of the fit limits the peak value by about 15%, inferred by setting $B = 2\varepsilon f_I(\omega)^2 = 6.1 \times 10^{-16}$, which is the second largest contribution in *B*. Examining *C*, the second term is too small to explain the observed size of C, which implies that $N_D(\omega) \approx 1.4 \times 10^{-6}$ (Hz)$^{-1/2}$. N_D is in very good agreement with the Johnson noise level calculated above. Elimination of N_D results in a shift of θ_m to $\sqrt{\varepsilon}$, where the noise level is only 15% less than the value at θ_m = 3.5 mradians with N_D as above. Azimuthal noise $\delta\theta$ prevents the improvement from being greater. To summarize, lock-in detection reduces the proportional noise due to the finite extinction ratio to values substantially smaller than the detector and azimuthal noise sources. In the case of the present system, the contribution to *C* from ε remains smaller than the detector-noise contribution until $\varepsilon = 3.5 \times 10^{-5}$.

A significantly higher S/N than obtained in Fig. 3.28 is possible. In principle, the detector noise can be reduced to the shot-noise limit by using a photomultiplier. In that case ε determines θ_m as in dc-SMOKE but the S/N(θ_m) will not grow substantially until the azimuthal noise is reduced. Azimuthal noise can be reduced to considerably smaller values than in the present system. Our SMOKE apparatus is integrated into a setup which is optimized for electron measurements, and has some shortcomings as far as SMOKE is concerned, problems which would be easily overcome in a dedicated SMOKE system. The most important problem is the lack of rigidity of the sample-holder, resulting in

vibrations and drift in the sample orientation during heating and cooling cycles. In the present system, Elimination of both N_D and $\delta\theta$ results in a shift of θ_m to $\sqrt{\varepsilon}$ and a 230 % increase in S/N. Furthermore, extinction ratios < 10^{-10} are possible,[11] much lower than are commonly achieved in SMOKE. With this as the noise limit, 2 to 3 orders of magnitude improvement are possible. For many experiments, however, the present noise level is acceptable.

Another important point is the elimination of stray signals synchronous with the reference frequency. Since large currents are usually employed to provide the applied field, care must be taken to avoid ground loops. In our system, which has *in situ* magnetic coils attached to the sample holder near the sample, a less obvious problem is present. We employ Helmholtz coils for in-plane measurements and the coils are mechanically coupled when a field is applied. A slight compliance of the sample holder causes a small magnetic/mechanical transduction. Apertures, which are required to for a small ε,[12] convert this small movement into intensity contrast at the detector. Drift of the sample holder during cooling and heating cycles causes a slow drift in the reflected beam orientation which affects the phase of the erroneous ac signal via a displacement of the mean laser beam orientation in the apertures. With an applied field amplitude of 16 Oe, this effect gives a false SMOKE signal of the order of 10^{-7} radians for in-plane measurements in the present system. The out-of-plane stability is at least an order of magnitude better, since a single coil is employed in the sample plane. To put these magnitudes in context, SMOKE signals of the order of 10^{-5} radians are typical for reversal of the moment in in-plane monolayer ferromagnetic films and an ac amplitude of order 10^{-6}

radians is obtainable near the in-plane order/disorder transition.[7] Stability is enhanced by using larger apertures, at a small cost of S/N since N_D dominates C for small ε. Of course, a superior coil system and more rigid sample holder would eliminate the problem altogether. Note that SMOKE systems with the magnets outside the vacuum may not be immune from similar false signals. *Ex situ* coils could produce even greater false signals due to the Faraday effect in optical windows.

3. The in-plane, order-disorder transition of a 1.2 ML Fe/ 1 ML Ni/W(110) film

The in-plane, order-disorder transition of a 1.2 ML Fe on 1 ML Ni on W(110) is presented as an example SMOKE susceptibility measurement. Ultrathin Fe/1 ML Ni/W(110) has an in-plane moment oriented along the W($\bar{1}$10) direction, although the use of a 2 ML Ni buffer results in a perpendicular moment at low Fe coverages.[8] The data of Fig. 3.29 was obtained for an Fe coverage of 1.2 ML, via longitudinal SMOKE with $\varepsilon \sim 10^{-6}$, θ = 2.9 mradians (10 arcminutes), a modulation frequency of 210 Hz, τ = 3 sec and an applied field amplitude of 1 Oe. The peak SMOKE rotation amplitude before conversion to magnetic units was of order μradians, and so the observed noise level is consistent with the test of Fig. 3.28. For temperature dependent measurements the sample is heated radiatively by a filament behind the sample. dc heating is employed since line-harmonics do enter the photodetector signal via the filament glow, even with the HeNe 6328 Å line filter. The stray field produced by the coil is estimated to be less than 10 mOe, which is much smaller than any modulation amplitudes used. The filament therefore represents a negligibly magnetic perturbation.

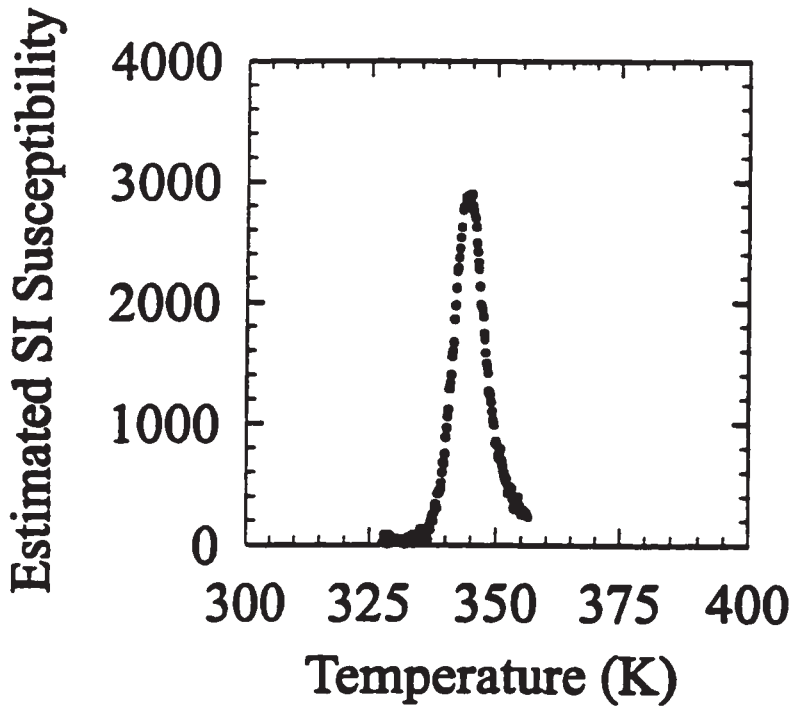

Fig. 3.29 - The magnetic susceptibility χ was measured at the order-disorder transition of a 1.2 ML Fe/1 ML Ni/W(110) film. θ was set to 10 arcminutes, the optimal setting as determined from Fig. 3.28. The peak value of χ in rotation units is of the same order as the test signal of Fig. 3.28, and the observed noise level is in agreement with that figure.

The approximate SI scale was obtained by assuming the bulk magnetization of Fe, and a saturation rotation of 10 μradians/ML, typical for a SMOKE rotation from a monolayer of Fe, and hence converting the SMOKE amplitude to susceptibility χ. Scanning tunneling microscopy, LEED and angle-resolved Auger electron spectroscopy studies indicate rather poor structural order of Fe on the 1 ML Ni buffer.[14,15] Still, the maximum value reached by χ was 3000. A reduction of the modulation amplitude did not increase the observed susceptibility, although a modest decrease of the peak width was observed. Previous experiments show that relatively large magnets (3 kOe) could not pull the moment along W(001) or out-of-plane,[14] suggesting a strong confinement of the

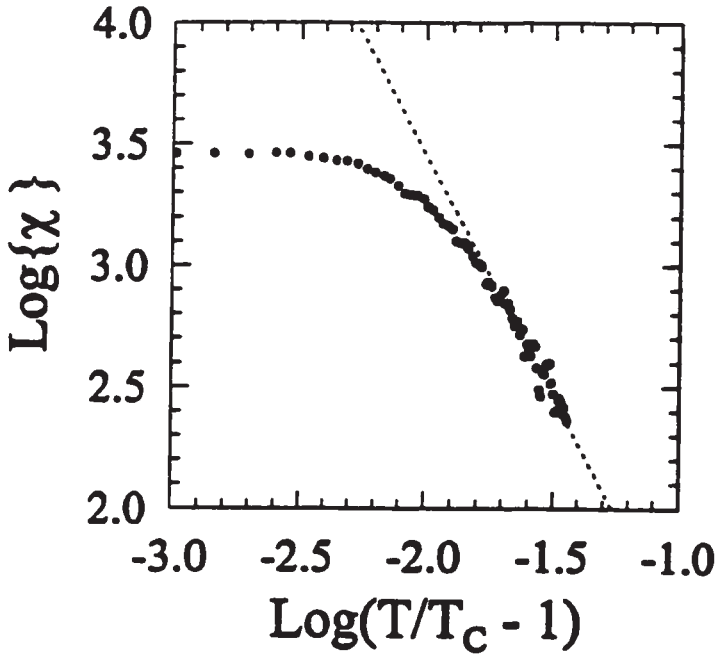

Fig. 3.30 - A log-log plot of the data of Fig. 3.29 gives $\gamma = 1.78 \pm 0.09$, which is in agreement with the 2D Ising result $\gamma = 7/4$. $T_C = 343.9$ K was determined by minimizing the statistical χ^2 of the linear fit to the data.

moment along W(110) by the magnetic anisotropy. One would therefore expect a 2-D Ising behaviour $\chi \propto (T - T_C)^{\gamma}$ in the order-disorder transition. A log-log plot of this data is presented in Fig. 3.29, using $T_C = 343.9$ K as determined by minimizing the statistical χ^2 of the linear fit to the data over a range of T_C. T_C is very close to the temperature of the peak susceptibility at 344.1 K. The resultant slope gives $\gamma = 1.78 \pm 0.09$ in agreement with expectations. Significant deviations from linearity on the log-log plot correspond to a deviation from exponential behaviour on the χ - T plot as T_C is approached from above. On the χ - T plot of Fig. 3.30, the deviation from exponential behaviour occurs at approximately 348 K, or 4 K above T_C. Since only a modest reduction of the peak-width was observed upon reduction of the applied field, it is unlikely that the applied field

amplitude was a significant factor in limiting the temperature range for which the divergent behaviour was observed. Finite-size effects due to the poor long-range structural order are a another possible explanation. The temperature range for which the exponential behaviour was observed corresponds to about 6 K, for which the change in χ was less than a factor of 10. A more accurate determination of γ would require more data on the high temperature side of T_c, not obtained in this experiment because of concern for the thermal stability of the film against intermixing. Nonetheless, this example demonstrates the extreme sensitivity achieved by the SMOKE susceptibility technique when the S/N is optimized. Even with a SMOKE apparatus of modest mechanical stability and non-negligible detector noise, as the one employed in these experiments, the determination of the critical exponent γ of monolayer ultrathin magnetic films is feasible.

This work was supported by the Natural Sciences and Engineering Research Council (NSERC) of Canada. C.S.A. gratefully acknowledges NSERC and Ontario Graduate Scholarships. The authors thank Marek Kiela for numerous technical contributions.

References

1. B. Heinrich, and J.F. Cochran, Advances in Phyics

2. S. T. Purcell, W. Folkerts, M. T. Johnson, N. W. E. McGee, K. Jager, J. Aan de Stegge, W. P. Zeper, P. Gruenberg, , Phys. Rev. Lett. 67, 907(1991).

3. Z.Q. Qiu, J. Pearson, and S.D. Bader, Phys. Rev. B 49, 8797(1994). F.O. Schumann, M.E. Buckley, and J.A.C. Bland, Phys. Rev. B 50, 16424(1994).

4. Z. Q. Qiu, J. Pearson, and S. D. Bader, Phys. Rev. Lett. 70, 1006(1993).

5. S. D. Bader, J. L. Erskine, in Ultrathin Magnetic Structures II, ed. by B. Heinrich, J. A.

C. Bland (Springer Verlag, Berlin, 1991).

6. A. Aspelmeier, M. Tischer, M. Farle, M. Russo, K. Baberschke, and D. Arvanitis, J. Magn. Magn. Mater. 146, 256(1995).

7. A. Berger, S. Knappman, H.P. Oepen, J. Appl. Phys. 75, 5598(1994).

8. C. S. Arnold, H. L. Johnston and D. Venus, to be published

9. C.S. Arnold, D. Venus, Rev. Sci. Instrum. 66, 3280(1995).

10. D. Venus, Rev. Sci. Instrum. 62, 1361(1991).

11. D. P. Shelton, Rev. Sci. Instrum. 64, 917(1993).

12. Removing the apertures following the analyzing polarizer typically results in $\varepsilon \sim 10^{-4}$, which is large enough that the intensity noise contribution in C grows larger than N_D and the S/N is depressed. Of course, the B term also grows.

13. The magnitude of the parasitic signal is comparable to the azimuthal noise density $\delta\theta(\omega)$ in a 1 Hz bandwidth, but is at low frequencies and is carried on the modulation. Whereas long time constants (> 30 s) dramatically reduce the azimuthal noise, the time scale of the drift in the erroneous signal is 10^{-7} radians in several minutes.

14. D. Sander, A. Enders, C. Schmidthals, J. Kirschner, H.L. Johnston, C.S. Arnold, and D. Venus, J. Appl. Phys.

15. H.L. Johnston, C. S. Arnold and D. Venus, to appear in Phys. Rev. B.

3.2.7 Mechanisms of magnetic contrast in χ measurements

Three types of magnetic contrast are common in magnetic susceptibility measurements. Fig. 3.31 demonstrates each mechanism. In (a), critical fluctuations grow strong near T_C. Blocks of aligned spins appear spontaneously, grow rapidly and melt. A field H applied parallel to an easy axis introduces a statistical bias favoring spins aligned with the field. Spatial averages over sufficiently large areas give a

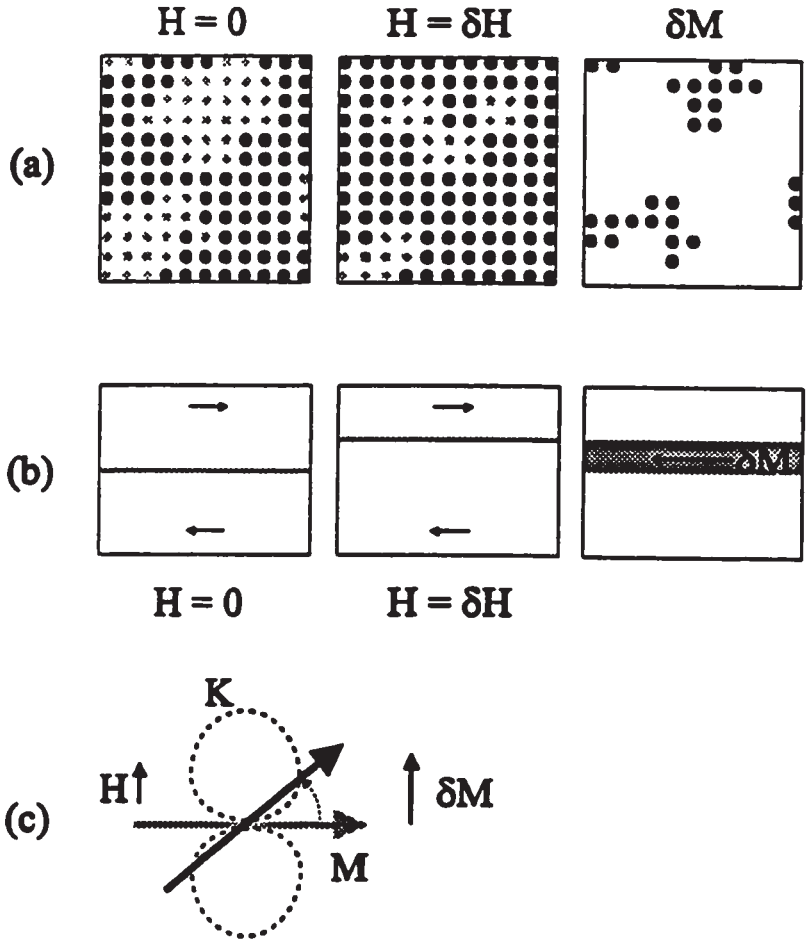

Fig. 3.31 - (a) Near an order/disorder transition an applied field produces a statistical bias for moments oriented along the field direction as in this Ising magnet example. (b) Similarly, an applied field may cause domain walls to displace, producing a net magnetic response. (c) If the field H is applied against a hard-axis anisotropy K, a response may be observed in the component of M parallel to the hard axis.

net δM proportional to the applied field. In (b), domain-wall motion has a similar description, but occurs over much greater time and length scales and occurs at lower temperatures. Finally, as shown in (c), if H is applied along a hard axis the moments can tip away from an easy-axis. This type of contrast we term anisotropy contrast.

3.2.8 Interpretation of the complex susceptibility

When the magnetic susceptibility is measured by lock-in detection, real (in-phase) and imaginary (quadrature) components are detected.[58] Lock-in amplifiers perform a finite-time Fourier transform of a measured signal, 'locking in' to the signal at the reference frequency. Typically, the input signal is amplified, multiplied by a normalized signal proportional to the reference signal, and the product is continuously integrated with a set time constant τ :

$$M(\omega) = \frac{1}{\tau} \int_{t-\infty}^{t} dt' \, e^{i\omega t - (t-t')/\tau} M(t') \quad . \tag{3.23}$$

The experimental susceptibility is

$$\chi_{ex} = M(\omega)/H_A \, , \tag{3.24}$$

where H_A is the amplitude of the applied field $H = H_A \cos(\omega t)$. The real part of the integrand ($\propto \cos(\omega t)$) is in-phase with the reference signal and the imaginary part (i $\sin(\omega t)$) is $\pi/2$ phase-shifted.

Fig. 3.32 demonstrates how the two components originate for different types of hysteresis loops. In these diagrams, an additional phase of π is added so that H starts at

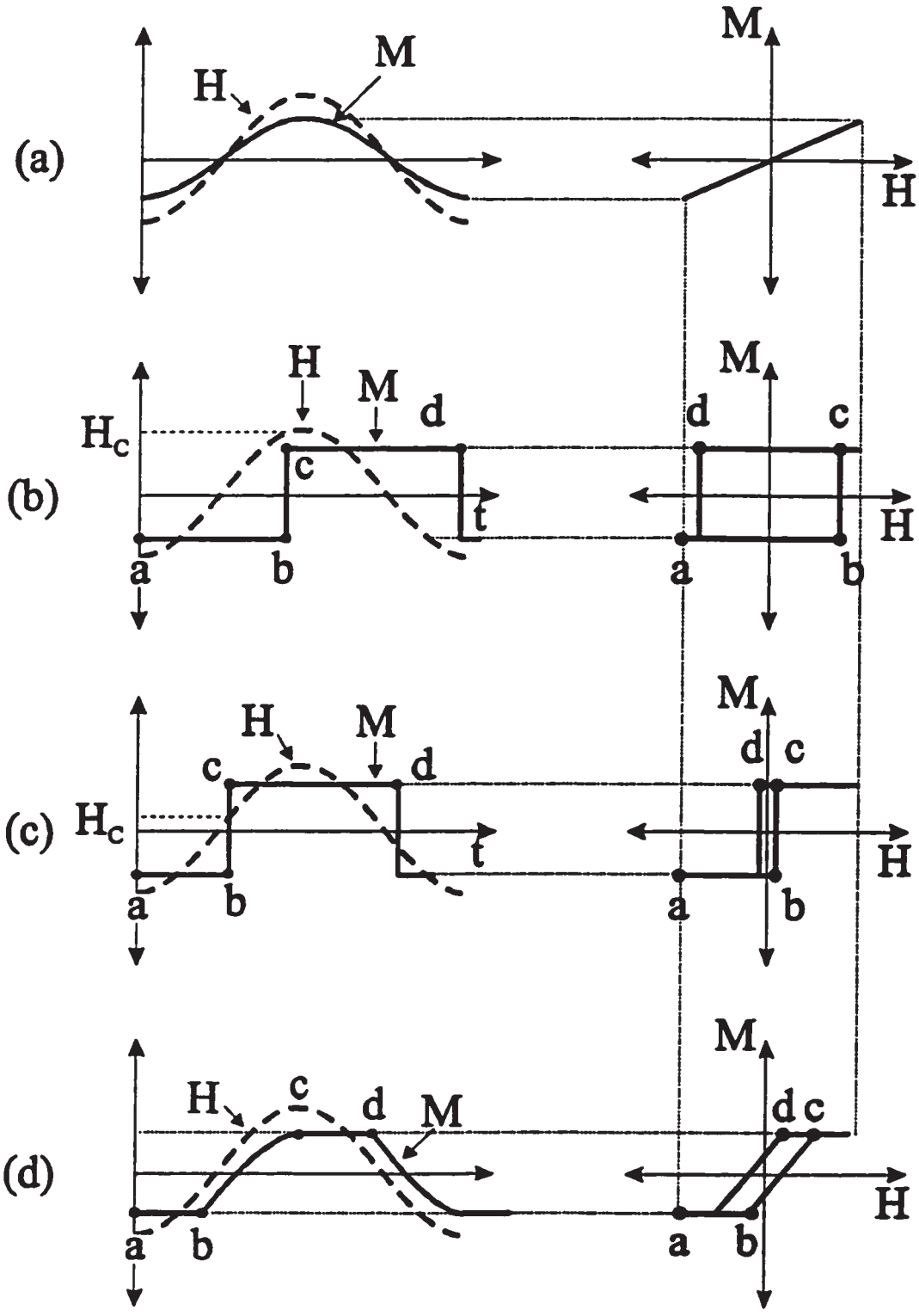

Fig. 3.32 - (a) A paramagnetic response in M is proportional to and in-phase with the applied field H. Square loops produce an M(t) which is phase shifted from H(t) by nearly $\pi/2$ for wide loops (b) and only slightly for narrow loops (c). Oblique loops (d) produce a similarly phase-shifted M(t).The coercive field H_c is labeled on (b) and (c).

its most negative value $-H_A$. M vs. H curves and hysteresis loops are shown on the right and the time records of M and H are displayed on the left. In case (a), the material is paramagnetic ($T > T_C$), and the magnetic response is simply $M(\omega) \approx \chi H_A$. Thus this signal is purely real for paramagnetic ($T > T_C$) films. *Remanence* ($M(H=0) \neq 0$) and hysteresis produce a non-zero imaginary part while a material is ferromagnetic ($T < T_C$). Square loops as in (b) and (c) give a phase-shifted square-wave response in time. In these cases the magnetic system proceeds through the points a→b→c→d as indicated on the time and M vs H plots. Wide hysteresis loops (b), for which the coercive field H_C (where switching occurs) is only slightly smaller than the applied field amplitude, result in an M(t) that is phase-shifted from H(t) by nearly $\pi/2$. Hence wide hysteresis loops produce a lock-in signal that is almost completely imaginary. A narrow loop (with a very weak coercive field) is nearly in-phase with the applied field, producing a lock-in signal that is almost completely real. Oblique loops as in (d) produce a similar, phase shifted signal. Generally, the imaginary part of the ac signal is proportional to the hysteresis loop area, which is the work done $M \cdot H$ by the applied field over one cycle of the loop. A non-zero imaginary part is therefore an indicator of ferromagnetism. Quantitative interpretation of the experimental susceptibility is generally very complicated in the ferromagnetic regime.

Fig. 3.33 illustrates the normal behaviour of the complex susceptibility at an order-disorder transition for an in-plane ultrathin film magnet. For $T > T_C$, a paramagnetic response produces a purely real susceptibility that grows according to the critical exponent γ as T_C is approached. Finite size effects preempt the divergence of χ at T_C, producing a rounding of χ and the onset of an imaginary part through the onset of remanence. As the temperature is further reduced, hysteresis loops quickly evolve to a square shape and the

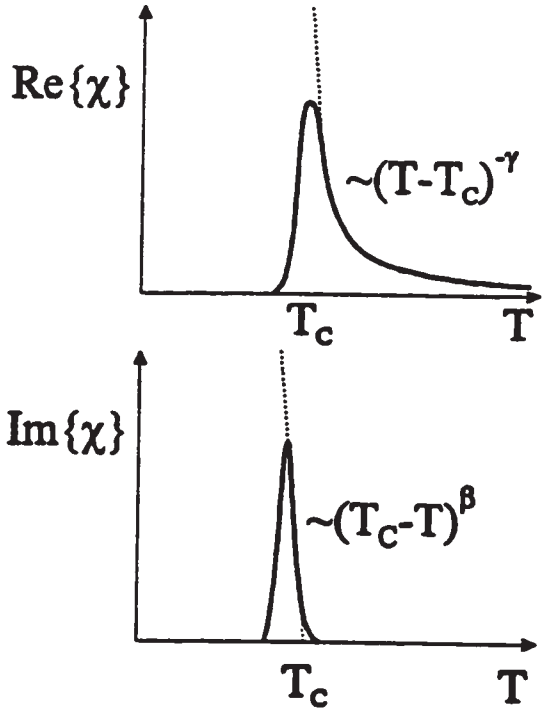

Fig. 3.33 - The real and imaginary parts of the experimental susceptibility track the fundamental susceptibility and remanent magnetization respectively.

coercive field also grows rapidly. The remanent magnetization grows with decreasing temperature according to the critical exponent β appropriate for that system. Since the modulation field is small, Im{χ} tracks the universal exponential growth only for temperatures where the applied field amplitude exceeds the coercive field. At lower temperatures Im{χ} decreases rapidly to zero.

3.2.9 Optical and magnetic calibration of χ

Optical calibration of SMOKE susceptibilities in rotation units (μradians) was performed for all susceptibility traces by a two point measurement prior to each run. Each measurement was made at a azimuthal set-point θ_{set} at 10 - 20 arcminutes (3 - 7 mradians), in order to maximize the S/N. The dc intensity on the photodiode was

measured at $\theta = 0$ and θ_{set}, and I_{max} was determined from $I(\theta=0) = \varepsilon I_{max}$ and $I(\theta_{set}) = I_{max}$ $(\theta^2_{set} + \varepsilon)$. Photodiode intensity, as amplified by the lock-in, was then converted to rotation units using the relation $\delta I = 2\, I_{max}\, \theta_{set}\, \delta\theta$. Errors in optical calibrations were largely due to mechanical drifts in the sample holder position during heating and cooling cycles which caused a small displacement of the laser beam in the apertures. These errors were minimized by periodically adjusting the apertures and θ_{set} to maintain a constant dc-level. Optical calibrations are reliable to a few percent. Because optical units are usually not very useful, more uncertain magnetic units were used to present experimental susceptibilities in this thesis.

Approximate magnetic calibrations were made by measuring the SMOKE rotation at a film thickness and temperature where a reasonable estimate of the film magnetization M was possible, and then comparing this to the observed magneto-optic rotation at other thicknesses and temperatures. From eqs. (3.8), the magneto-optic rotation for a given material on a given substrate is proportional to the magnetization M and film thickness t. A calibration constant, the magneto-optic rotation per a standard thickness and magnetization

$$q = \phi_s / M_s t_s \tag{3.25}$$

is then used to calibrate rotations $\delta\phi$ at other thicknesses t to changes in magnetization

$$\delta M_s = \delta\phi / qt \tag{3.26}$$

In the case of Fe, films were cooled to well below their T_C, where they could be prepared in a single-domain state, with an M_s similar to the $T = 0$ value. $\underline{M}$ was reversed by capacitive discharge through the field coils, producing large field pulses (1 - 3 kOe). In the polar effect, 1 ML of fcc Fe/2 ML Ni was found to produce $\Delta\theta \approx 200$ μradians of

rotation upon reversal, which is close to that obtained for bulk bcc Fe. For this reason, the fcc Fe was assumed to have the same q calibration as bcc Fe. In-plane calibrations were estimated by using the factor of 25 'rule-of-thumb' by which the polar effect exceeds the longitudinal effect. This admittedly crude approximation was used because the in-plane magnetization near the reorientation transition, subject to strong fluctuations, could not be reliably estimated.[59] Magnetic calibrations are certainly correct to within a factor of 2 or 3, but are not nearly as accurate as the less useful magneto-optic calibration.

4. MAGNETIC SUSCEPTIBILITY OBSERVATION OF A SPIN-REORIENTATION TRANSITION

Studies which apply the surface science and magneto-optic techniques to the observation of a spin-reorientation transition are described in this chapter. SMOKE susceptibility measurements prove ideal for studying this transition and addressing some fundamental aspects absent from previous experimental studies. One important result is the first observation of the region near the multicritical point of the spin reorientation transition, permitting investigation of the topology of the coverage-temperature phase diagram in this region. Another important experimental result is that the loss of magnetic order from an ultrathin film with a perpendicular moment is fundamentally different than for an in-plane magnet, even if no spin-reorientation occurs. Polar susceptibilities are well described by the domain model of Kashuba and Pokrovsky.[30] Several aspects of the results are the first experimental verifications of predictions by theorists.

This experimental study of the spin-reorientation transition is based upon recent collaborative work on fcc (face center cubic) Fe, grown on a 2 ML Ni buffer on W(110).[40-42] SMOKE hysteresis loop experiments were undertaken to survey the magnetic properties of fcc Fe, grown on a 2 ML Ni buffer on W(110). The general interest in fcc Fe is that bulk Fe is bcc at temperatures where it is magnetic and the change in structure is often associated with dramatic changes in magnetic

behavior. This system was chosen because of its (111) orientation, which differs from the (100) orientations used in previous studies.[60] (111)-oriented samples are expected to exhibit a smoother fcc to bcc transition with increasing coverage, and also to have superior long-range structural order, expectations which were verified by the structural studies. The present work was initiated by a magnetic survey of Fe/2 ML Ni/W(110). While Fe on this substrate does not exhibit exotic magnetic behaviour associated with the unusual fcc structure, it does exhibit a spin-reorientation transition.

Although the author grew almost all of the films studied for presentation in this chapter, the growth recipe and structure were previously determined by H. L. Johnston *et al.* Section 4.1 is a review of the growth and structural results, with emphasis on those details relevant to the magnetism. Polar susceptibility measurements are introduced in section 4.2. The most important results are contained in section 4.3 as an included paper, 'Magnetic susceptibility measurements near the tricritical point of the spin reorientation transition in ultrathin fcc Fe(111)/2 ML Ni/W(110) films'. Since the format of that paper is somewhat brief, its findings are augmented by further supporting data in section 4.4. As shown in section 4.5, polar susceptibilities are consistent with an exponential condensation of domains with increasing temperature. It is argued in section 4.6 that the transition to disorder from the perpendicular phase is fundamentally different than for in-plane transitions. Finally, the observed trend in the peak polar susceptibility with film thickness is presented in section 4.7.

4.1 Review of the growth and structure of x-Fe/2 ML Ni films

Metastable magnetic materials, which do not exist in the bulk, can be engineered by MBE. One such system that has been studied intensively is the Fe/Cu(100) system which is fcc at room temperature. Bulk Fe has a high temperature fcc phase, but is bcc at and below room temperature. fcc Fe exhibits interesting magnetic properties, which is reviewed below.

The Fe/Cu(100) system is, however, structurally complicated for a two main reasons.[30, 31] The first reason is that Cu and Fe intermix considerably at the interface. The second is that the fcc to bcc transition is expected to be less continuous for a fcc (100) surface than a (111) surface. H. L. Johnston proposed the use of a Ni(111)/W(110) substrate in order to avoid these complications. Less intermixing of substrate and overlayer were expected in the case of Fe and Ni, due to the relative surface free energies and, of course, Ni(111) had the desired orientation. W(110) was chosen as the substrate for the Ni because Ni grows in its fcc (111) structure on this surface.

4.1.1 Growth and structure of the Ni buffer

Kolaczkiewicz and Bauer studied the growth of Ni on W(110) in detail with LEED, AES, thermally programmed desorption (TPD) and work function measurements and the results are summarized here.[50] The growth of the first ML of Ni is similar to that of Co on the same surface, as described in sections 3.1.4 and 3.1.5. Just as in the case of Co on W(110), the density of the first layer is greater when the substrate has been heated. Ni AES uptake curves exhibit a first breakpoint at 0.65 ML for room temperature growth

and 0.76 ML for high temperature growth, where 1 ML corresponds to one close-packed (CP) ML. The corresponding LEED patterns is pseudomorphic (PS) at low coverages and then a PS→CP transition occurs before the growth of the second layer begins. As with Co,[49] the PS and CP MLs are both thermally stable until desorption above 1100 K. Second and subsequent layers tend to form islands when the film is heated. They found that the growth mode was very nearly layer-by-layer, with the third layer starting to grow while the second was 94% complete. The growth of Ni differs from that of Co in that

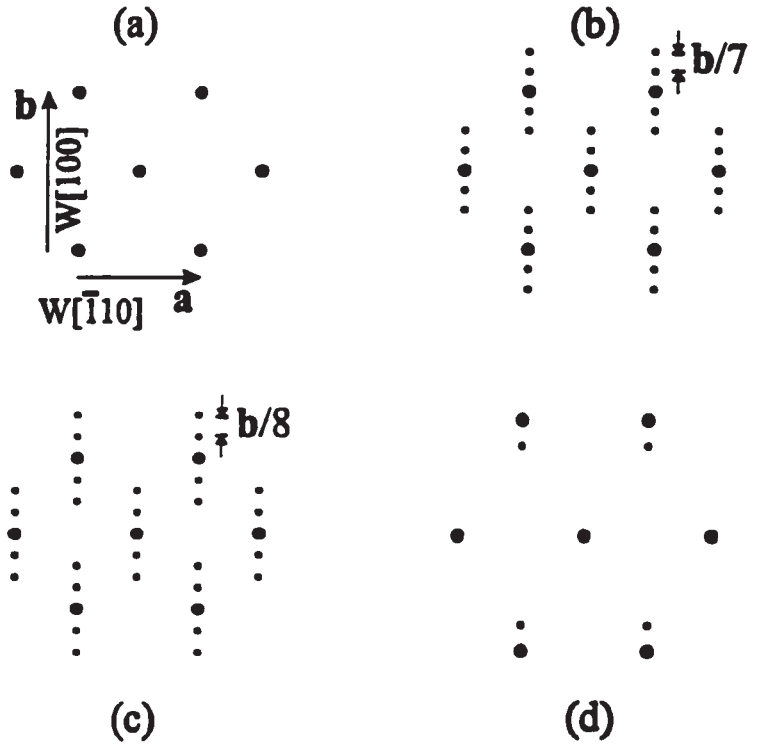

Fig. 4.1 - The LEED pattern during the growth of Ni on W[110] is PS as in (a) for low coverages, showing the same symmetry as the bcc [110] face of the substrate. At the completion of the PS ML, the LEED pattern transforms to the pattern in (b) with 1/7th of the spot spacing in that direction, indicating an increase in density. The density further increases by 2 ML (c). For thicker films, a nearly hexagonal pattern is consistent with [111] oriented fcc Ni.

additional strain is relieved as the second layer grows. The CP Ni ML exhibits satellite spots in the LEED pattern with $1/7^{th}$ of the spacing of the W pattern in that direction. As the second layer grows, the spacing between the spots decreases to $1/8^{th}$ of that of the W spots. They interpret the corresponding change in density as follows. One ML Ni/W(110) is 2.2% compressed in the $W[001]_{bcc}$ ($Ni[-110]_{fcc}$) direction and 7.4% expanded in the $W[-110]_{bcc}$ ($Ni[11-2]_{fcc}$) direction. The uniaxial distortion is decreased in the 1/7 → 1/8 strain relaxation to 3.7% compressed in the $Ni[-110]_{fcc}$ direction and 1.0% expanded in the $Ni[11-2]_{fcc}$ direction. For films of 3 or 4 MLs in Ni thickness, the pattern is very nearly hexagonal, reflecting the symmetry of the fcc Ni(111) plane. The evolution of the LEED pattern is illustrated in fig. 4.1.

STM images of the 2 ML film (fig. 4.2) support Kolaczkiewicz and Bauer's conclusions about film smoothness.[61] The approximately parallel lines which are nominally perpendicular to W(100) are atomic steps. Dark areas are voids in the 2^{nd} ML, or rather, bare 1 ML patches. The small bright areas are 3^{rd} layer growth. The 2 ML Ni is not completely flat, but has about 5% voids in that layer as determined from an examination of the 140 000 $Å^2$ trapezoidal step in the upper right corner of the image. Similarly, about 5% of the 3^{rd} layer of Ni has formed. This is nearly perfect layer-by-layer growth.

Fig. 3.13 is an ARAES scan of a 2 ML Ni/W(110) substrate, obtained by H.L. Johnston. The electron-scattering simulation of the data (performed by this author), based on 2 ML fcc Ni with the appropriate strain for the 1 x 8 structure, was in excellent agreement with the data. Two orientations of the 2^{nd} ML Ni are possible, due to the two

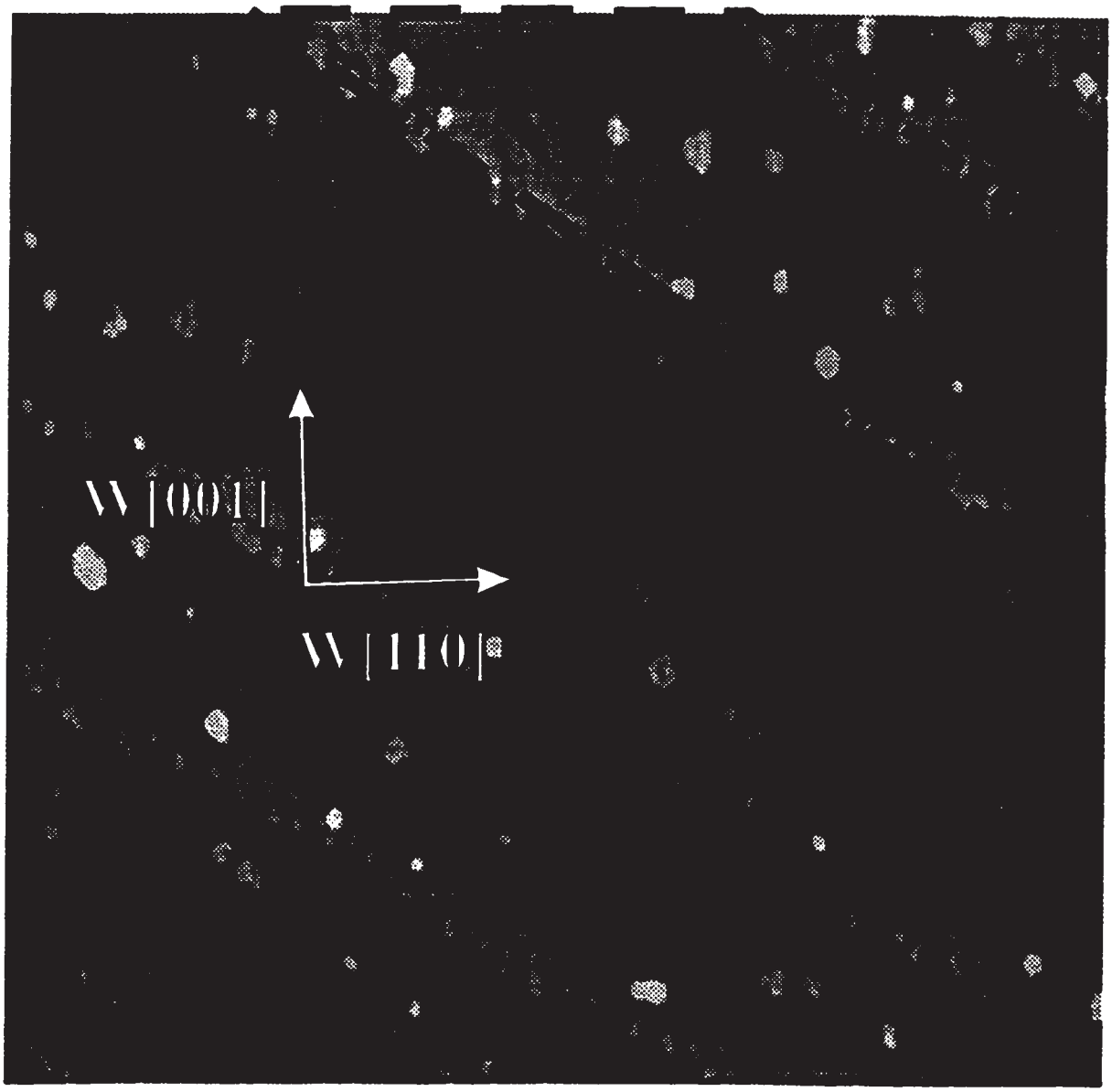

Fig. 4.2 - A 2500Å x 2500Å STM image of 2 ML Ni/W[110], obtained by C. Schmidthals and D. Venus and printed with their permission. The darker areas are bare 1 ML Ni, the white areas 3 ML and the rest is 2 ML Ni. The 2nd ML Ni grows as islands on the smooth 1st ML separated by a few hundred angstroms. They coalesce as the 2nd ML approaches completion, producing the observed void pattern. Approximately 5% of the 2nd layer is absent and 3rd layer is started, as determined from the trapezoidal area. This is much more ideal than many metal-on-metal systems.

inequivalent adsorption site types in the fcc (111) unit cell. These sites are indicated in fig. 4.3. Both site orientations were assumed in equal proportion in the electron scattering calculations. Justification for this assumption, further to the good quality-of-fit to the ARAES data, is that the 2nd layer grows as islands separated by a few hundred angstroms. The voids in fig 4.2 above are located at the edges of islands which have coalesced. Each type of site has an equal probability of being selected by each island.

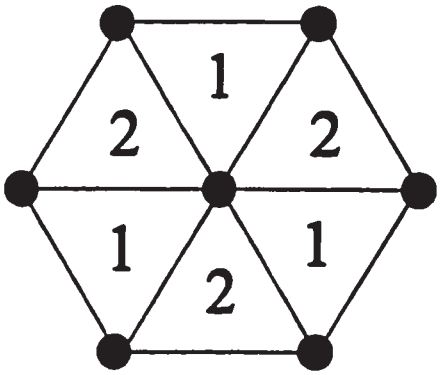

Fig. 4.3 - After the completion of the 1st fcc [111] ML of Ni, there are two possible sites (1 and 2) that the next fcc layer can choose. Both orientations are observed in the ARAES data. This is expected on the basis of the island growth mode of the 2nd ML of Ni.

4.1.2 Growth and structure of x-Fe/ 2 ML Ni/W(110)

The major conclusions of H.L. Johnston's ARAES studies are summarized here.[30] The interested reader is referred to Dr. Johnston's Ph.D. thesis for a detailed discussion.

(i) The 1 ML Ni buffer is not an adequate substrate for the growth of fcc Fe. LEED and ARAES data suggest that Fe/1 ML Ni does not grow in the fcc phase, but rather converts

immediately to bcc. This may be due to the greater strain present in the first ML as compared to the more relaxed second ML.

(ii) On thicker Ni buffers, Fe initially grows in a slightly strained fcc phase for Fe coverage x = 0 to 3 ML, and then undergoes a gradual transformation to the bcc phase which is completed by 12 ML. For x = 0 to 3 ML, the fcc Fe unit cell has the same lateral dimensions as the 2 ML Ni buffer. For future magnetic experiments, a thin Ni buffer was desired in order to minimize the *magnetic* role of the buffer. In this manner, the film magnetic properties would be dominated by the Fe. Two ML Ni buffers were therefore chosen as the standard in both structural and magnetic studies.

(iii) Both possible fcc domain orientations are seen, as would be expected since they are both present in the Ni buffer.

(iv) Intermixing of overlayer and substrate increases gradually with temperature. ARAES data, fit to electron scattering calculations, suggest that films grown at 360 K have 25% +/- 10% Fe in the 2nd Ni layer.

(vi) The first evidence of bcc growth, present in both the LEED patterns and ARAES rocking curves, occurs at x = 4 ML.

STM images of Fe/1.5 ML Ni/W(110) reveal a fundamental difference between the topologies of Fe on 1 and 2 ML Ni buffers. Fig.4.4 is a 2500 x 2500 Å^2 scan of approximately 1/10th ML Fe on 1.5 ML Ni/W(110). The second ML Ni is present in the form of islands ~100 Å in diameter, with a similar separation. These islands grow preferentially from step edges, in a mode of growth intermediate between island growth

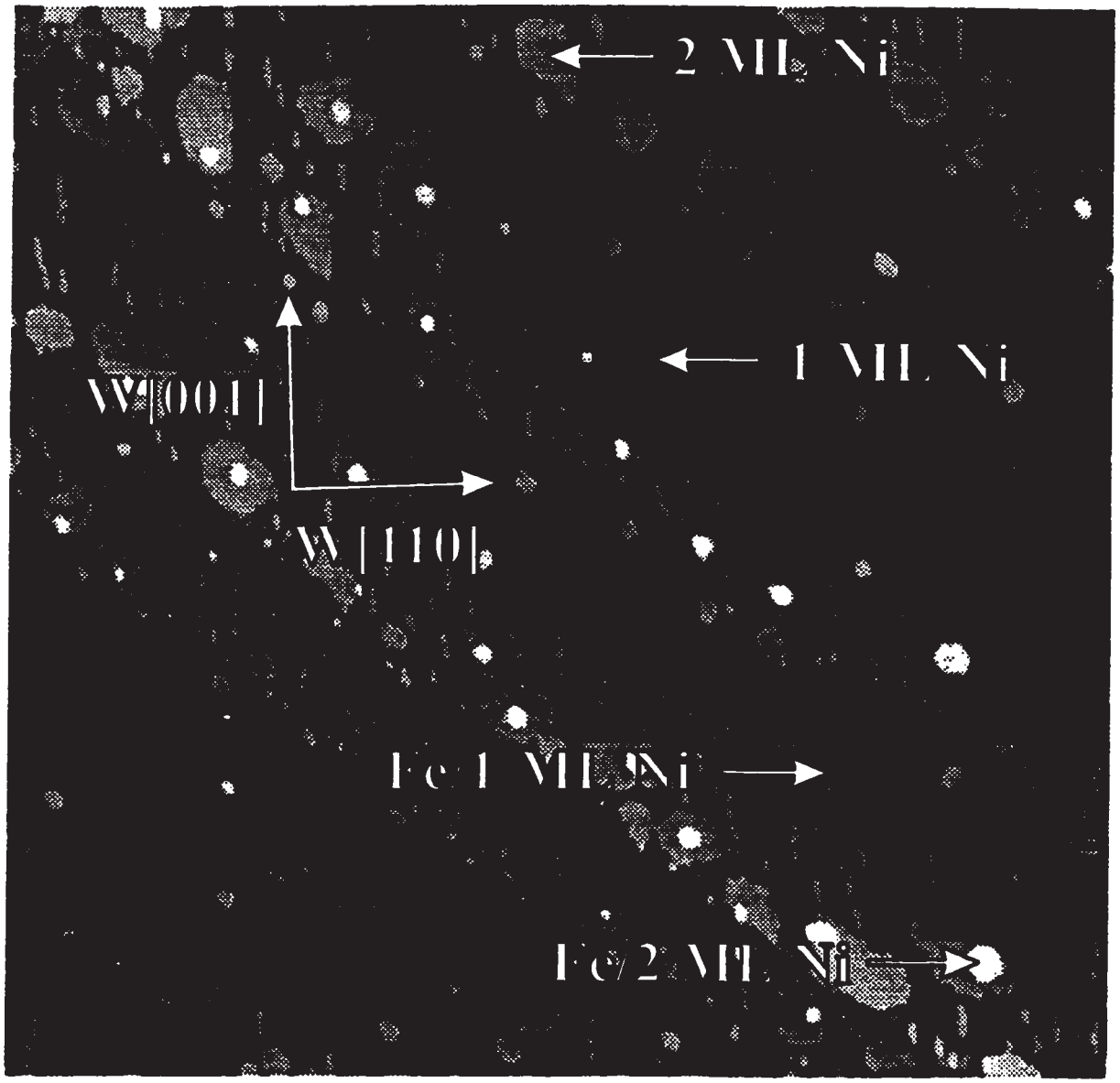

Fig. 4.4 - STM image of a 2500 x 2500 Å^2 area, showing the initial stages of growth of Fe on 1.5 ML Ni/W(110). Fe grows in circular islands on the 2 ML Ni patches, and in elongated strips on the bare 1 ML Ni.

and edge-flow growth, which is ideal type of layer-by-layer growth. Bare 1 ML Ni is therefore concentrated in the center of the steps. The small (~20 Å), white circular islands on the 2 ML Ni are Fe, known to be fcc from the ARAES studies. On the 1 ML Ni, which is exposed in the spaces between Fe islands, Fe grows in small strips (~20 x 100 $Å^2$) with the long axes preferentially oriented along W(001). Atomic resolution was not achieved in the STM studies, so the atomic arrangements could not be determined from the images.

A growth recipe based on the above work was used in the magnetic studies reported in this chapter. Prior to each film growth, the W substrate was heated in an O_2 atmosphere to over 1000 K and then flashed to 2500 K in UHV. O_2 cleaning is especially effective for removing carbon, which is the major contaminant in W. After cleaning, carbon contamination was checked by inspection of the 250 - 290 eV range of the AES spectrum which contains a carbon peak. No experiment proceeded without reducing the carbon contamination to or below the detection limit, corresponding to less than 1 % of the W area. Ni was deposited on a heated (> 500 K) substrate for the first 1 ML of growth to ensure a flat, smooth atomic layer. The 1 ML coverage was always verified by measuring the attenuation of the W AES signal in the 150 - 190 eV range, known to be 0.55 for 1 ML of Ni. Second layer growth proceeded at or below 350 K, to prevent island growth (SK mode). W attenuation was measured again to ensure that the film was at least 2 ML thick. In a few cases Ni buffers marginally thinner than 2 ML were used and unusual magnetic behaviour was observed. These cases are described later. Ni thicknesses were certain to within 5%, or 0.1 ML for the 2 ML buffer. Fe was grown on

the 2 ML Ni buffer at 350 K. Fe evaporation rates were calibrated by growing Fe/W(110) and comparing the Fe AES uptake curve with the data of Gradmann *et al.*[74] Although this method calibrated the Fe rate to within 5%, the Fe rate was calibrated with less frequency than the Ni, which was calibrated in each experiment. It was more convenient to calibrate the Ni than the Fe, since a Ni buffer on W(110) was required for each Fe/Ni film, whereas Fe/W(110) was only prepared for the explicit purpose of calibration. Because the Fe deposition rate of the electron-beam evaporators drift slowly over several experiments, some Fe thicknesses may be as much as 10% off.[63] Deposition temperatures were tightly controlled.

4.2 The magnetic susceptibility of a film with perpendicular magnetization

A magnetic susceptibility measurement of 1 ML Fe/2 ML Ni/W(110) film is presented in fig. 4.5. The configuration of this measurement is unusual (in comparison to the literature) because both the magnetization and applied field are perpendicular to the film plane. Because of this geometry, the resultant susceptibility is designated $\chi_{\perp}$. To the best of our knowledge, only one example measurement of this kind presently exists in the literature.[64] The present work is the first detailed, systematic study of this kind. A number of in-plane magnetic susceptibility measurements of order-disorder transitions exist and are very similar to that of fig. 3.29, with peak magnitudes of 10^3 to 10^4 in SI units, and half-width half-maxima (HWHM) of only a few K.[65, 55] The $\mathrm{Re}\{\chi_{\perp}\}$ in fig.

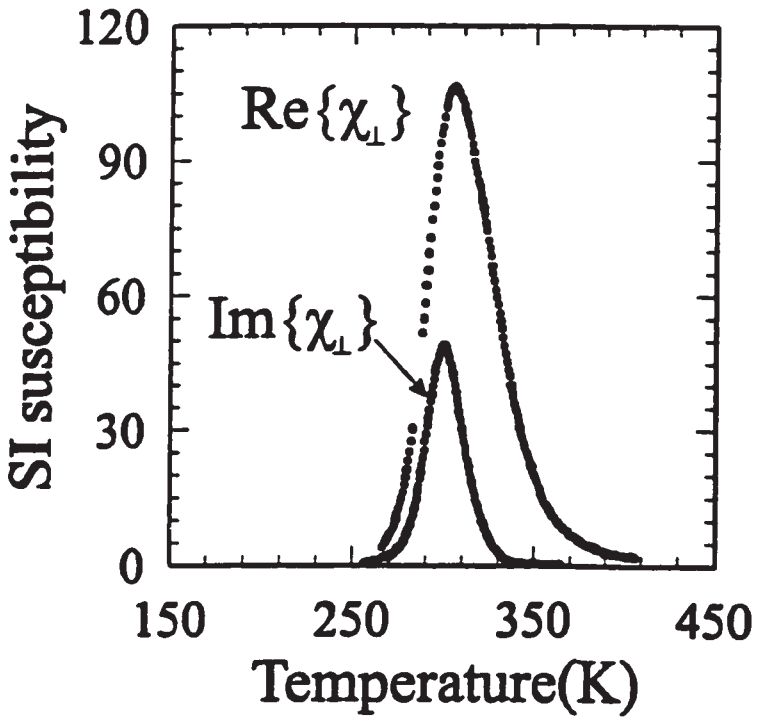

Fig. 4.5 - This susceptibility measurement of the perpendicularly magnetized film 1 ML Fe/2 ML Ni/W(110) was obtained with the applied field also perpendicular to the film. In comparison to in-plane, order-disorder susceptibilities, $Re\{\chi_\perp\}$ is more than 10 times smaller and more than 10 times broader in temperature.

4.5 differs from the $Re\{\chi\}$of in-plane order-disorder transitions in both its magnitude and temperature width. $Re\{\chi_\perp\}$ peaks at about 100 in SI and has a HWHM of about 70 K. Another difference between $\chi_\perp$ and the χ of in-plane, order disorder transitions is that the temperature where $Re\{\chi_\perp\}$ reaches its peak value is substantially higher than the lowest temperature where $Im\{\chi_\perp\}$is zero. For in-plane transitions, the corresponding temperatures approximately coincide.[58] This is a characteristic common to almost all of the $\chi_\perp$ measured in this study. In the present discussion, only the magnitude and HWHM

are analyzed. The intention is to demonstrate that the observed $Re\{\chi_\perp\}$ is not simply an order-disorder peak distorted by the large demagnetization factor associated with perpendicular geometry, a point made tersely in the included paper of section 4.3.

The $Re\{\chi_\perp\}$ of fig. 4.5 is suggestive of an order-disorder transition that has been broadened and attenuated by a large demagnetization factor. T_C is not expected to exceed 400 K for a 1 ML film of Fe,[66] and so it is not unreasonable to identify the only observed feature in this temperature range with the order-disorder transition. For now, we model the polar susceptibility on a 2-D Ising susceptibility, as observed in-plane, but with the dipolar interaction included in the demagnetization field. The total *internal* field, *external* field plus demagnetization field, is $H_{int} = H_{ext} - NM$, where N is the demagnetization factor. As a result,

$$\chi_{ext} = \chi_{int}/(1 + N\chi_{int}).^{58} \qquad (4.1)$$

Fig. 4.6 was generated using eq. (4.1) and assuming an internal susceptibility which diverged as $(T\text{-}300\ K)^{-1.75}$, for temperatures greater than 300 + 1 K, and reaching a peak value of 10 000 at 300 K. This choice of χ_{int} mimics the typical behaviour of in-plane susceptibilities, where N = 0. Demagnetization factors of N = 1, 1/10 and 1/100 were then used in eq. (4.1). Since the maximum value of (4.1), which occurs at T_C = 300 K, is 1/N, $N\chi_{ext}$ is plotted rather than χ_{ext}. A demagnetization factor of N = 1/100 in a 2-D Ising model reproduces both the observed amplitude (~100 or 1/N) and temperature half-width of the measured polar susceptibility.

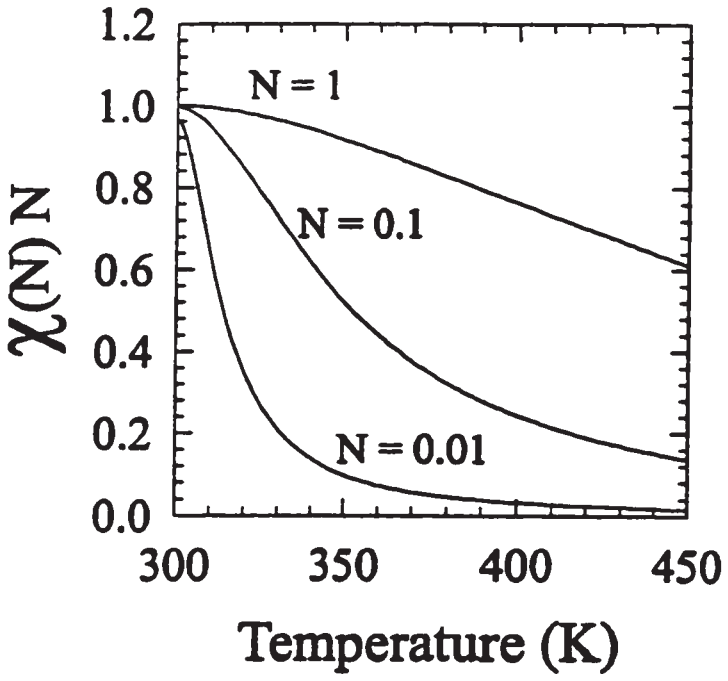

Fig. 4.6 - $\chi_\perp(N)N$ for demagnetization factor N = 1, 0.1 and 0.01, and T_C = 300 K. Demagnetization factors of order 0.01 approximately reproduce the observed amplitudes and widths of $\chi_\perp$, but are unphysically small.

A demagnetization factor N = 1/100 is, however, grossly unphysical for the perpendicular geometry for which N = 1 is expected. One might imagine that it is the demagnetization field in the vicinity of a spin-block boundary which is most relevant for determining the external susceptibility, since there is an adjacent spin block at the boundary with its spins oriented in the opposite direction, and the effective demagnetization factor could be reduced. A simple calculation shows that the reduction in H within a film thickness of a boundary, which is roughly equivalent to an atomic diameter at the ML thickness limit, is only an order of magnitude. The maximum demagnetization factor that one obtains from this type of argument is then N > 0.1, which is insufficient to explain the observed magnitude and temperature breadth of $\chi_\perp$. We will argue in the next

section and in section 4.5 in more quantitative detail, that the behaviour of $\chi_{\perp}$ is dominated by domain-wall motion.

4.3 Magnetic susceptibility measurements near the multicritical point of the spin reorientation transition in ultrathin fcc Fe(111)/2 ML Ni/W(110) films

The following is an early, shorter version of a paper submitted to *Physical Review Letters*. After the rejection of that manuscript, an even longer version was submitted to *Physical Review B* where it is expected to appear late in 1997 or early in 1998. Copyright is not yet assigned. C. S. Arnold grew most of the films, executed all of the magnetic measurements and data analysis, and wrote the first draft of the paper. H. L Johnston determined the growth modes and structure and grew some of the films for these magnetic experiments. D. Venus supervised the projects, participating in the interpretation of the data, recommending experiments and participating in second and subsequent drafts of the paper.

Magnetic susceptibility measurements near the multicritical point of the spin reorientation transition in ultrathin fcc Fe(111)/2 ML Ni/W(110) films

C. S. Arnold, H. L. Johnston, and D. Venus

Department of Physics and Astronomy and Brockhouse Institute for Materials Research
McMaster University, Hamilton, Canada L8S 4M1

Abstract

Magnetic susceptibility measurements made using the Kerr effect, are reported for ultrathin films of x ML fcc (111) Fe grown on a 2 ML Ni/W(110) substrate, and show that these films undergo a spin-reorientation transition with increasing temperature. The results give an approximate temperature *vs.* film thickness phase diagram of the spin-reorientation transition and magnetic order-disorder transition near the multicritical point where they meet. Complete spin-reorientation transitions are observed for thicker films, but at lower thicknesses the order-disorder transition proceeds directly from a perpendicularly magnetized domain phase which precedes the spin-reorientation.

The spin-reorientation transition is a fascinating magnetic ultrathin film phenomenon which depends on the interplay of perpendicular magnetic anisotropy (PMA), spin fluctuations and domain formation. Following an early prediction of Néel,[1] experiments have shown that the reduced symmetry of an ultrathin film can lead to a magnetocrystalline anisotropy favouring a perpendicular orientation of the magnetic moment, even overcoming the shape anisotropy which strongly favours an in-plane orientation. Numerous studies[2] have further shown that as the film thickness is increased at constant temperature, the shape anisotropy overcomes the magnetocrystalline anisotropy, the sign of the PMA is reversed, and the magnetic moment lies in-plane. The point where the PMA passes through zero in simple models is particularly interesting, as in the absence of a magnetic anisotropy the magnetic system is isotropic, and cannot support long-range order[3,4].

Pappas *et al.*[5] provided the first evidence that an analogous reorientation can occur for a film of a constant thickness as a function of temperature. This reorientation from perpendicular to in-plane magnetization is usually termed the "spin-reorientation transition" in ultrathin films.[6] For fcc Fe/Cu(001), Pappas *et al.* found that a temperature range $\Delta T \sim 20K$ of negligibly small remanence accompanied the reorientation, and suggested that this was due to either a loss of magnetization when the PMA was zero, or to an instability against the formation of small domains[7]. Theoretical work described this in mean-field[8] and renormalization-group theories,[9,10] and found that loss of magnetization should occur only for a temperature range of ≤ 1 K. The alternate hypothesis of a domain structure below the spin-reorientation temperature T_R, was verified by Allenspach and

Bischoff[11] using spin-polarized electron microscope images of Fe/Cu(001), in excellent agreement with calculations by Kashuba and Pokrovsky[12]. These findings were confirmed by Qiu *et al.*,[13] who studied the reorientation transition in bcc Fe/Ag(100) with the magneto-optical Kerr effect (MOKE) using standard dc techniques to measure hysteresis loops. They further plotted the magnetic order-disorder phase boundary at low thicknesses, and the spin-reorientation phase boundary at greater thicknesses, but unfortunately reported no measurements over an intermediate thickness range. Politi *et al.*[14] subsequently presented renormalization group calculations, neglecting domain effects, and predicted that this intermediate thickness regime contained both a maximum in T_R and a multicritical point where the order-disorder and spin-reorientation transition boundaries meet. Abanov *et al.*[15] calculated the domain phase diagram for this system using a continuum, mean-field theory, and found three distinct domain structures in the approach to T_R from below. Because the domains are very sensitive to fields applied perpendicular to the film plane, they recommended the use small applied fields (~1 Oe) in experiments.

In order to sort out the complicated interaction of the domain structure, the spin-reorientation transition, and the order-disorder transition, further experimental studies are urgently needed. The present paper reports such a study for ultrathin fcc Fe(111) films grown on a 2 ML Ni(111)/W(110) substrate. Use of a 2 ML Ni(111)/W(110) substrate permits the characterization of the magnetism in fcc films of Fe which exhibit better wetting and less interdiffusion than those grown on a Cu substrate.[16,17] As a result, the Fe films can be conveniently prepared at room temperature. The growth of the Ni buffer and Fe films was monitored by Auger electron spectroscopy (AES), angle resolved AES

(ARAES), and LEED. Reproducible results are obtained only if the first monolayer of the Ni buffer is grown at, or annealed at, an elevated temperature.[18] Ultrathin magnetic Ni/W(110) has been studied extensively[19], and although magnetic resonance studies[20] indicate an in-plane moment along W[001] with T_c approximately at room temperature for a 2 ML film, magnetic susceptibility measurements showed that the 2 ML Ni films used in this study were paramagnetic at temperatures above 200 K. Since the finite-size scaling trend of T_c has an extremely steep slope in this range of thickness[20], small differences in thickness calibration could account for this difference. The first 3 ML of Fe grow in a nearly layer-by-layer fashion on the 2ML Ni/W(110) substrate.[17] The propagation of strain from the bcc W(110) substrate results in a slightly strained fcc (111) lattice which has 2-fold in-plane rotational symmetry, similar to the Ni buffer.[19] At coverages $x = 4$ ML, a surface cell intermediate to fcc and bcc first appears. The Fe monolayer has perpendicular magnetization when the Ni buffer thickness is 2 or 3 ML, or perhaps for even greater Ni thicknesses.[18] Other details of growth, structure and thickness calibration are reported elsewhere.[17]

The measurements of the external magnetic susceptibility $\chi_{ext} = \partial M/\partial H_{ext}$ of ultrathin films using MOKE is new technique[21] which has not yet been applied in detail to films with perpendicular magnetization. Measurements average over the size of the laser spot, and are therefore sensitive to the domain-averaged magnetic response. For low coercive fields, the real (in-phase) part of the susceptibility measures the saturation magnetization, while the imaginary (quadrature) part measures the remanent

magnetization.[21] Both components fall off as the coercive field grows much larger than the applied field. Near an order-disorder transition, the spin correlation length diverges, and the domain structure must in any case disappear. The film therefore acts as a single domain sample, and the internal susceptibility $\chi_{int} = \partial M/\partial H_{int}$ diverges at the critical temperature. In thin films, the internal field is itself strongly influenced by the magnetization through the demagnetization field, $H_{int} = H_{ext} - NM$, where N is the demagnetization factor.[22] As a result, $\chi_{ext} = \chi_{int}/(1 + N\chi_{int})$ as in eq. (4.1).

For an infinite, flat film, $N_{\parallel}=0$ for $H_{ext}\parallel M$ in-plane, and $N_{\perp}=1$ for $H_{ext}\parallel M$ normal to the surface (polar). At an order-disorder transition where in-plane magnetization disappears, $\mathrm{Re}\{\chi_{ext}\}$ diverges, to form a narrow peak located close to the critical temperature T_c, and is limited to 10^3 - 10^4 by sample perfection and the finite field modulation.[21] The disappearance of $\mathrm{Im}\{\chi\}$ is an indicator of T_c which is not dependent on the modulation amplitude. At an order-disorder transition where perpendicular magnetization disappears, the polar susceptibility $\chi_{ext} \sim 1/N_{\perp} \approx 1$ and is insensitive to the transition. Far below an order-disorder transition, the susceptibility is primarily sensitive to changes in the domain-averaged magnetization due to domain structure and/or motion. The domain walls are perturbed by the Zeeman energy term due to the applied field, $E_Z = -H_{ext}\cdot M$, with the size of the demagnetizing field *within each domain* being unaffected. Thus the demagnetizing factor in eq.(4.1) does not play a role in the susceptibility. For perpendicular magnetization, the polar susceptibility due to domain effects does not saturate, and

therefore dominates the total signal. By contrast, for in-plane magnetization the in-plane susceptibility due to domain effects is dwarfed in the presence of a diverging critical susceptibility. The two measurements are therefore sensitive to different magnetic phenomena. The polar susceptibility should be particularly sensitive to presence of a perpendicular domain phase, and is therefore an ideal probe for the current studies.

Magnetic measurements were made via the polar and longitudinal Kerr effects, using a previously described apparatus, s-polarised HeNe laser light, and lock-in amplification techniques.[23] Stray magnetic fields, such as the Earth's field, were eliminated to order 10 mGauss by three large pairs of mutually perpendicular Helmholtz coils. *In situ* magnet coils generated a 210 Hz, ac modulated field with H oriented along one of three mutually perpendicular directions labelled with respect to the W(110) substrate, giving $\chi_{\perp}$, χ_{001} and $\chi_{\bar{1}10}$. Real and imaginary parts were measured separately with a single-phase lock-in amplifier. The effective polarization extinction ratio was 5 x 10^{-7} to 10^{-6}. The largest noise source was polarization fluctuations from the vibration of the sample holder arm, resulting in a detection limit of approximately 40 x 10^{-9} radians rms on the Kerr angle modulation. Applied field amplitudes were usually 15 Oe and 6 Oe for perpendicular and in-plane measurements respectively. Approximate SI calibrations were made by assuming the magnetization of bulk Fe and comparing the observed Kerr rotation amplitude to the rotation per monolayer in saturated hysteresis loops. Since the magneto-optical Voigt parameters for these films are not known, this absolute calibration is uncertain by as much as a factor of 2.

The magnetic susceptibility for all three field orientations, for a 2.25 ML Fe film on 2 ML Ni/W(110) are presented in fig. 4.7. Part a) shows the real parts, while b) gives the imaginary parts. The measurements are reversible so long as the temperature does not exceed 400 K. Note that the polar susceptibilities have been multiplied by a factor of 70 so that they could be viewed on the same plot as the in-plane measurements. The magnitude of $\chi_{\perp}$ is nonetheless much greater than unity, and must therefore represent domain effects. $\mathrm{Re}\{\chi_{\perp}\}$ has a broad peak at 248 K, with a tail extending to higher temperature. Remanent magnetization is detected in $\mathrm{Im}\{\chi_{\perp}\}$ and persists to 280 K, after which there is a gap from 280-322 K in which no remanent magnetization is detected in any of the Kerr signals. At higher temperatures, remanence reappears in-plane along W[001], as indicated by a peak in $\mathrm{Im}\{\chi_{001}\}$, demonstrating that the spins have reoriented along W[001], or equivalently, the $[01\bar{1}]$ direction of the fcc Fe. This shows that the strain in the films is sufficient to create a uniaxial in-plane anisotropy. There is an accompanying real response in χ_{001}, with a peak value of approximately 1200, which conforms to that expected near an in-plane order-disorder transition.[21] The considerable width (FWHM=25 K) of this peak is attributed to the large ac field of 6.0 Oe used for this particular measurement. Apparently, the in-plane magnetization is stable only for a small temperature range at this Fe film thickness. In the region of zero remanence, there is also a purely real response in $\chi_{\bar{1}10}$, which is discussed later.

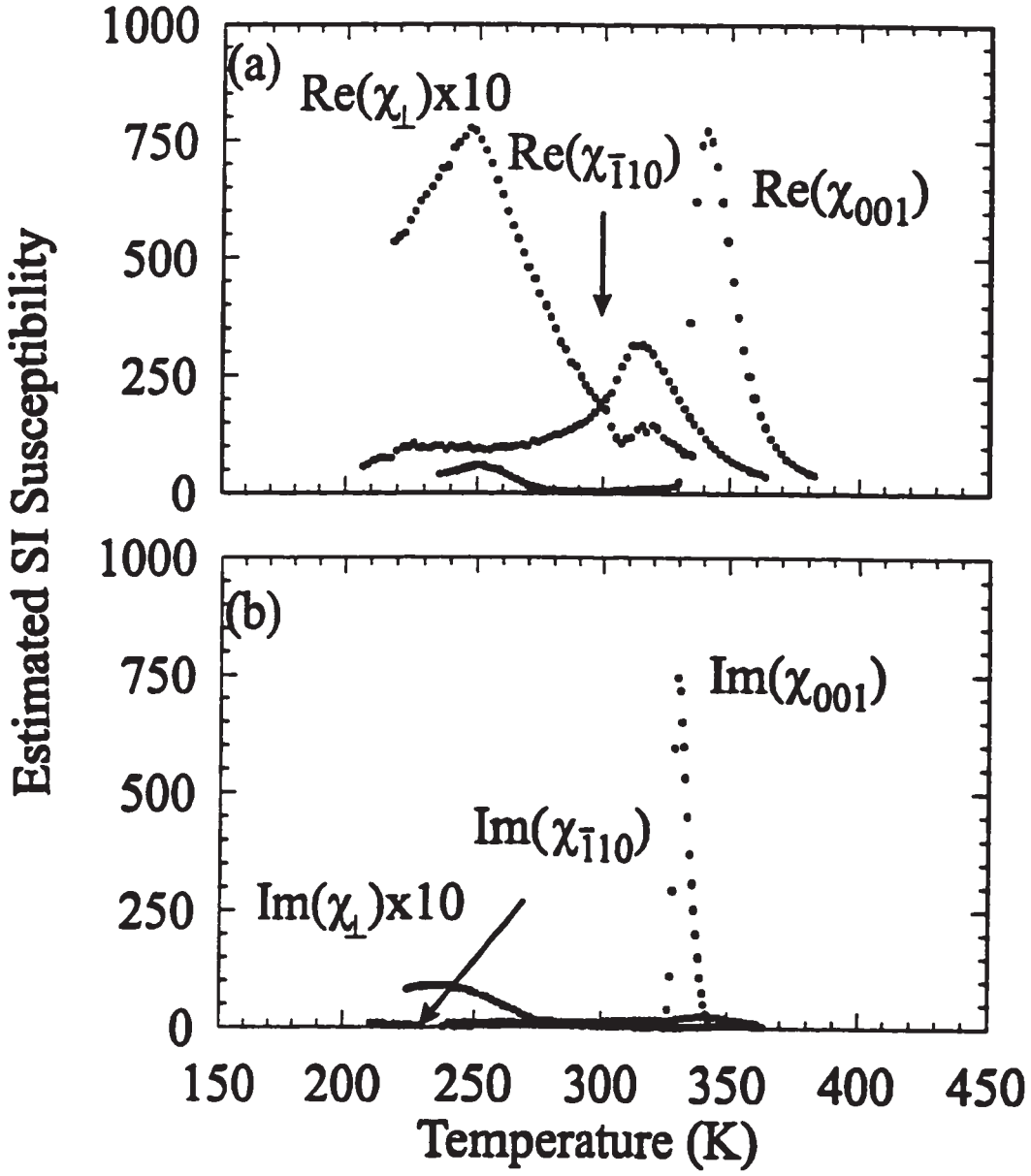

Fig. 4.7 - The magnetic susceptibility of a 2.2 ML Fe film grown on a 2 ML Ni/W(110) substrate. χ is measured using the Kerr effect for applied field orientated along three mutually perpendicular directions referred to the surface of the W substrate. The magnetization is normal to the surface at low temperatures, and in-plane along W[001] at higher temperatures. There is a gap ΔT between 280 and 328 K where no remanence is detected (for the small modulation fields used), which is interpreted as a region of complicated domains of perpendicular magnetization. See the text for a discussion of $\chi_{\bar{1}10}$.

In overview, it is clear that a spin-reorientation transition occurs. The detailed behaviour of the susceptibilities can be interpreted using the domain model of Abanov *et al.*[15] They calculated a reduced (i.e. unitless) magnetization m, which results from the difference in the spin up and down domain widths, L-δ and L+δ , of linear density n=1/L, upon the application of a reduced external magnetic field strength h. Because a (111) surface has only a very weak preference for domain wall orientation[12,24] L is interpreted in the present circumstance as a characteristic domain size rather than as a strictly ordered, stripe width. This gives a domain-averaged magnetization m = nδ, and an equilibrium magnetization in a mean-field theory of

$$m = (2/\pi) \arcsin [2h/(\Omega n^*(T))], \qquad (4.2)$$

where Ω is the dimensionless scale of the long-range magnetic dipole interaction energy, and

$$n^*(T) \sim \exp-[\pi(8\Gamma\lambda)^{1/2}/\Omega + 1] \qquad (4.3)$$

is an exponential function of the (dimensionless) exchange energy Γ, effective anisotropy energy λ and the dipolar energy. In this domain model, the external polar susceptibility in the limit of small h is

$$\chi_\perp = \partial m/\partial h = [\,(\pi/4)\,\Omega n^*(T)]^{-1} \qquad ; T < T_R. \qquad (4.4)$$

The authors show[15] that near the spin-reorientation temperature, as the effective anisotropy energy λ approaches zero, the domain linear density n*(T) grows exponentially, giving a temperature range ΔT of complicated domain patterns which

exhibit greatly reduced remanence. Fig. 4.7 gives $\Delta T \approx 40K$, in agreement with measurements on other Fe film systems.[5,11,13] Eq.(4.4) shows that $Re\{\chi_\perp\}$ decreases as the domain density increases in the approach to T_R, in agreement with fig. 4.7. At low temperatures, $Re\{\chi_\perp\}$ is governed by the coercive field, and increases with temperature. An experimental peak in $Re\{\chi_\perp\}$ is formed at the intersection of these two limiting behaviours, and should be a reliable, although approximate, indicator of the formation of the domain phase. A series of measurements of $\chi_\perp$ with the applied external field amplitude varied from 1Oe to 10 Oe, are consistent with this interpretation, as they showed increasing broadening only on the low-temperature side of the peak, where the coercive field plays a role.

The purely real response $\chi_{\bar{1}10}$ is somewhat mysterious, but is likely related to imperfections in the 2 ML Ni buffer. ARAES[17] results indicate that the Fe grown on a 1 ML Ni buffer does not grow in the fcc structure, and scanning tunnelling microscopy[25] images show that the growth morphology is similar to that seen for bcc growth directly on W(110). Fig. 4.8 (a) shows the real magnetic susceptibility measured for a 1.5 ML Fe film grown on a 1 ML Ni buffer. $Re[\chi_{\bar{1}10}]$ indicates an in-plane magnetization along $W[\bar{1}10]$, as is seen for Fe grown directly on W(110).[26] The width of the peak at the order-disorder transition at 345 K is consistent with eq.(4.1) with $N_1 \approx 0$, and the smaller ac field modulation of 2.0 Oe used in this experiment. Data taken with a modulation field of 1.1 Oe show a peak susceptibility of nearly 3000. Data for Fe grown on 1.5 ML

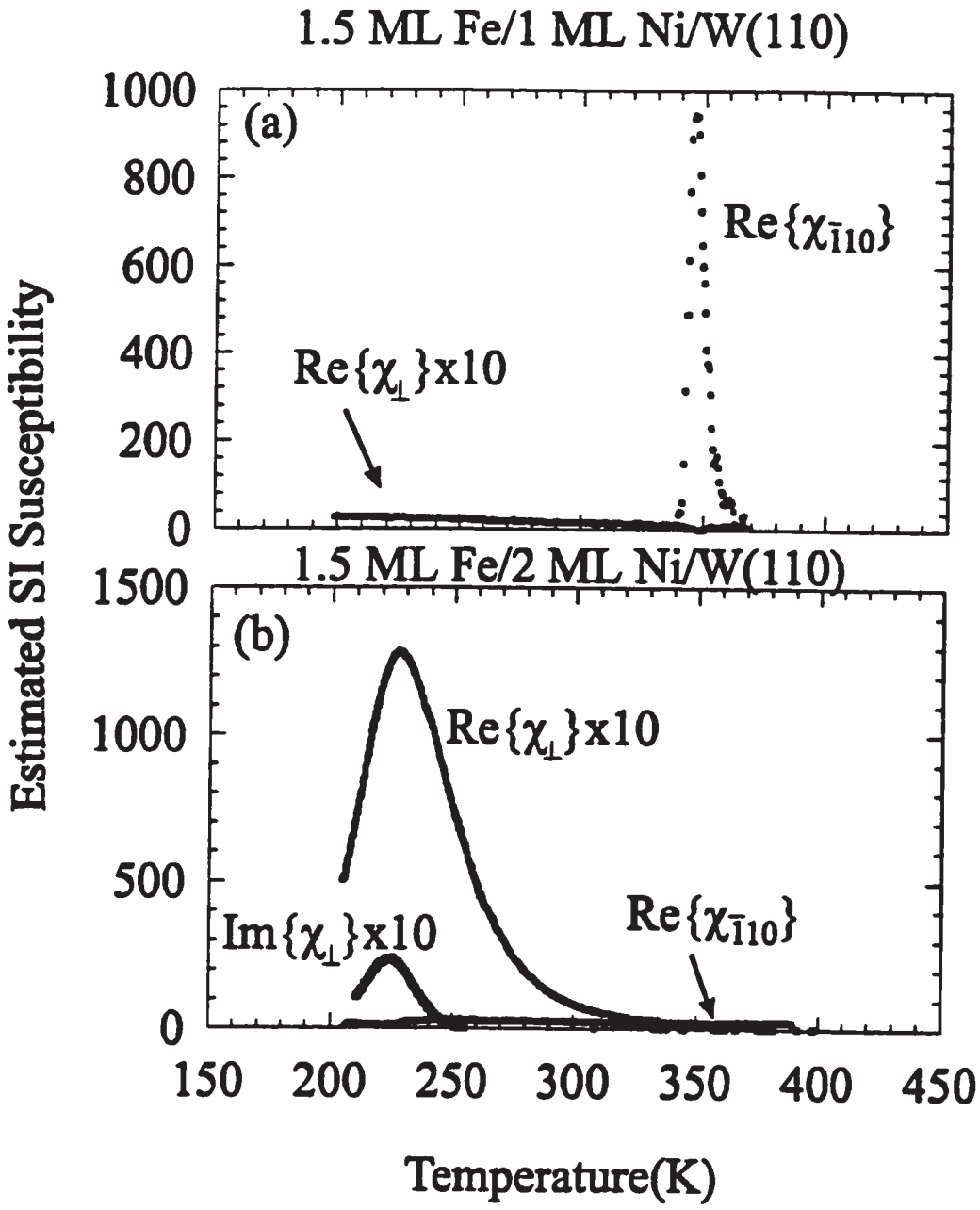

Fig. 4.8. - (a) The magnetic susceptibility of a 1.5 ML Fe/ 1 ML Ni/W(110) film indicates in-plane magnetization along W[$\bar{1}$10]. (b) The magnetic susceptibility of 1.5 ML Fe/ 2 ML Ni/W(110) indicates normal magnetization at low temperatures, and no spin-reorientation. The peak value of the susceptibility is approximately 100, and must therefore be due to domain wall motion.

Ni (not shown) reveals simultaneous remanence along the surface normal and W[$\bar{1}$10], indicating either distinct magnetic regions, or a canted moment. Although use of an ideal 2 ML Ni buffer should result in only fcc Fe, STM images[18] of a 2 ML Ni buffer shows small regions of size <10 nm of 1 and 3 ML Ni thickness, comprising about 5% of the film. We speculate that Fe grown on 1 ML Ni in these regions may continue to give a weak, non-remanent response in Re{$\chi_{\bar{1}10}$} when surrounded by the predominant fcc Fe portion of the film magnetized in another direction. As can be seen in fig. 4.7, this response displays a broad peak just below T_R in all those films showing a complete spin-reorientation transition. Apparently the properties of these small regions of the film can become influential when the surrounding fcc Fe film is in a temperature range where the direction of magnetization is not otherwise well-defined.

Fig. 4.8 (b) presents magnetic susceptibilities measurements for 1.5 ML Fe on a 2 ML Ni buffer. Comparison with fig. 4.7 shows the low-temperature peak in $\chi_{\perp}$ associated with the domains of perpendicular magnetization, but no signature of the in-plane reorientation or the order-disorder transition in χ_{001}. We conclude that the order-disorder transition in this film proceeds directly from the domain phase, and cannot be observed in the magnetic susceptibility either because of the large demagnetization factor in eq.(4.1), or because the domain phase maps continuously onto the paramagnetic phase.[27] This interpretation is supported by the systematic dependence of the magnetic susceptibility on the Fe thickness, as summarized in fig. 4.9. Detailed χ measurements (all

three applied field orientations) were performed at x = 1.5, 2.0, 2.25, 3.0 and 4.0 ML, and individual susceptibility components were measured for other thicknesses. Solid dots represent the temperatures of the peaks in Re{$\chi_\perp$} and the dashed lines connecting them are guides to the eye. Open circles represent the points where remanence vanishes or

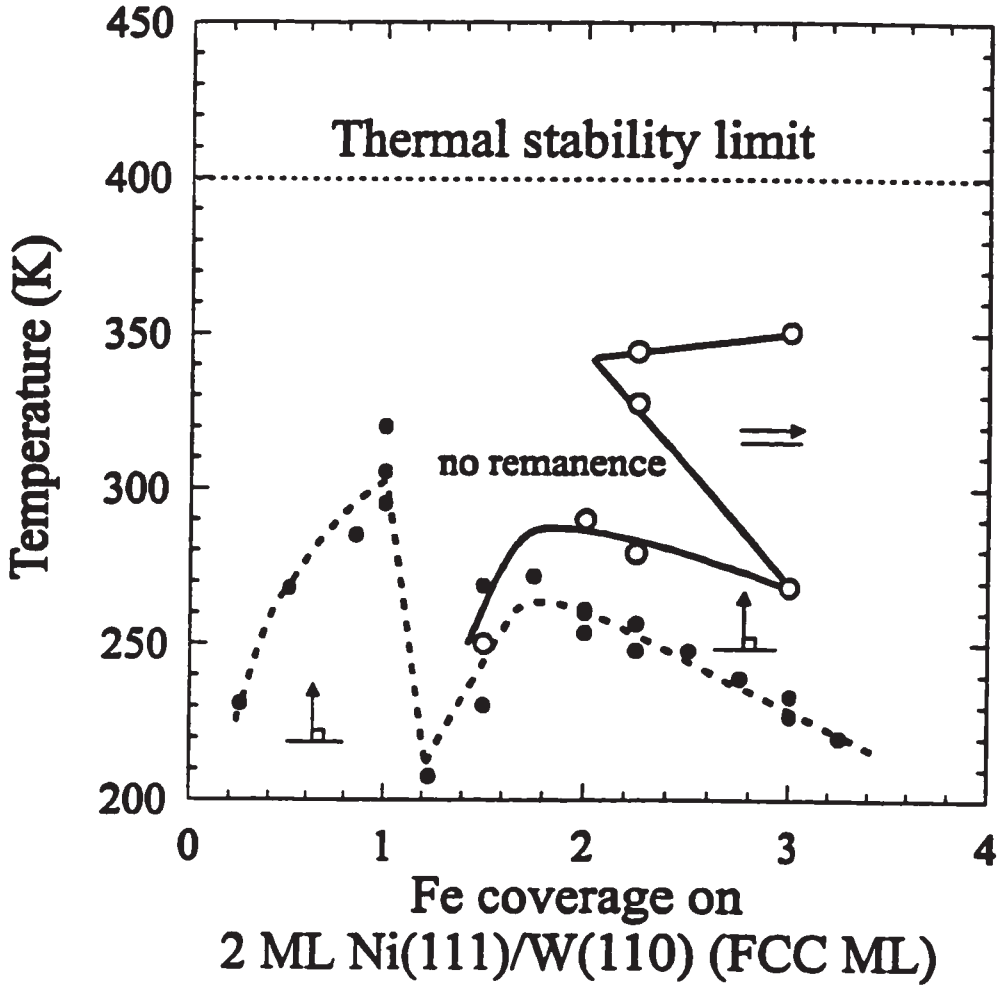

Fig. 4.9 - A partial phase diagram of the spin-reorientation transition in Fe/2 ML Ni/W(110). The solid dots connected by a dashed line are the peak positions of Re{$\chi_\perp$}. The open circles connected by a solid line are locations where the imaginary part of either the perpendicular or in-plane susceptibility becomes zero. Regions of the diagram are marked as having perpendicular, in-plane, or no remanence.

appears, and are joined by a solid line. The regions on the diagram are labelled according to whether perpendicular, in-plane, or no remanence was observed in the associated $\mathrm{Im}\{\chi\}$.

For Fe thicknesses $2<x\leq 3$ ML, $T_c>T_R$ and the order-disorder transition proceeds from the reorientated phase. Three markers of the spin-reorientation process — the temperature where in-plane remanence appears, the upper limit of perpendicular remanence, and the peak in $\mathrm{Re}\{\chi_\perp\}$— all decrease with increasing x in this regime. For $1 < x < 2$, the peak in $\mathrm{Re}\{\chi_\perp\}$,and the upper limit of perpendicular remanence increase with increasing x, reaching maxima at $x = 2$. In this regime, the critical transition from the perpendicular domain phase cannot be observed in $\chi_\perp$. Since the spin reorientation transition is not observed for $x \leq 2$, and first seen at $x = 2.25$, the multicritical point of the system must be at values intermediate to those two and at approximately 335 K. Fig. 4.7 is therefore an observation of the magnetic susceptibility in the neighbourhood of the multicritical point where the spin-reorientation transition and the order-disorder transition lines meet. It is interesting to note that this occurs at the thickness where the markers of the spin-reorientation transition have maxima, in agreement with the prediction of Politi *et al.*[14]

Films less than 1 ML thick appear to form a qualitatively distinct region where properties are determined by the formation of the Fe/Ni interface. $\mathrm{Re}[\chi_\perp]$ again has a

broad peak consistent with domain wall motion. It is clear that the films have perpendicular remanence down to a thickness at least as small as 0.25 ML Fe, and that the Ni moments in the 2 ML buffer must be actively participating in the formation of the perpendicular magnetization when the Fe islands are below the percolation limit. Upon completion of the monolayer, the sudden drop in the temperature at which the peak in $\mathrm{Re}\{\chi_\perp\}$ occurs implies significant changes in the magnetocrystalline anisotropy of the film in moving from the interface layer to the Fe bilayer.[24] The topology of fig. 4.9 suggests two interpretations. It may be that the spin-reorientation temperature in submonolayer films is very high, and that the peak in the susceptibility for submonolayer films marks a domain formation process driven *not* by a disappearance of the PMA, but by the order-disorder transition.[12,23] The mechanism driving domain formation would then be different on each side of the discontinuity at 1 ML. This would be consistent with the data of Qui *et al.*[10] on a different Fe film system, which shows order-disorder transitions at low thickness, spin-reorientation transitions at high thickness, but nothing in the region of the multicritical point, perhaps due to the lack of sensitivity of their dc MOKE technique. In the second interpretation, changes in the surface electronic structure upon completion of 1 Fe monolayer may create such a profound change that the phase boundary for the order-disorder transition also changes abruptly. Further experiments are required to examine this region of the phase diagram.

In summary, measurements of the ac magnetic susceptibility of fcc Fe/2 ML Ni/W(110) films have revealed a complicated interdependence of the spin-reorientation

transition, the formation of perpendicular domain phases, and the order-disorder transition on the film thickness. For thicker films, a full reorientation occurs, whereas for thinner films the order-disorder transition proceeds directly from the domain phase. The multicritical region where $T_R \approx T_c$ is found to coincide with the maximum in T_R. There is evidence that submonolayer Fe films form a domain phase driven not by a vanishing PMA, but by the order-disorder transition itself.

This work was supported by the Natural Sciences and Engineering Research Council (NSERC) of Canada. C.S.A. and H.L.J. gratefully acknowledge Ontario Graduate Scholarships. The authors thank C. Schmidthals, M.P.I. Halle, for STM pictures of Fe/Ni/W(110) films and Marek Kiela for numerous technical contributions.

References

1. L. Néel, J. Phys. Radium **15**, 225, (1954).

2. B.Heinrich and J.F.Cochran, Adv. in Physics **42**,523, (1993).

3. N.D. Mermin , and H. Wagner, Phys. Rev. Lett. **17**, 1133, (1966).

4. R.P. Erickson and D.L. Mills, Phys. Rev. B **43**, 11 527, (1991); M. Bander and D.L. Mills, Phys. Rev. B **38**, 12 015, (1988).

5. D. P. Pappas, K.-P. Kamper, and H. Hopster, Phys. Rev. Lett. **64**, 3179, (1990).

6. Reorientation from in-plane to perpendicular may occur due to strain. P.J. Jensen and K.H. Bennemann, Solid State Commun. **100**, 585, (1996); F. Huang, M.T. Kief, G.J. Mankey, and R.F. Willis, Phys. Rev. B **49**, 3962, (1994); B. Schulz and K. Baberschke, Phys. Rev. B **50**, 13 467, (1994).

7. Y. Yafet, and E.M. Gyorgy, Phys. Rev. B **38**, 9145, (1988).

8. P.J. Jensen, K.H. Bennemann, Phys. Rev. B **42**, 849, (1990).

9. D. Pescia, and V. L. Pokrovsky, Phys. Rev. Lett. **65**, 2599, (1990).

10. R. P. Erickson, and D. L. Mills, Phys. Rev. B **46**, 861, (1992).

11. R. Allenspach, and A. Bischof, Phys. Rev. Lett. **69**, 3385, (1992).

12. A.B. Kashuba, and V.L. Pokrovsky, Phys. Rev. B **48**, 10 335, (1993).

13. Z. Q. Qiu, J. Pearson, and S. D. Bader, Phys. Rev. Lett. **70**, 1006, (1993).

14. P. Politi, A. Rettori, M.G. Pini, and D. Pescia, J. Magn. Magn. Mater. **140-144**, 647, (1995).

15. A. Abanov, V. Kalatsky, V. L. Pokrovsky, and W. M. Saslow, Phys. Rev. B **51**, 1023, (1995).

16. D.A. Steigerwald, I. Jacob, and W. F. Egelhoff Jr., Surf. Sci. **202**, 472, (1988).

17. H.L. Johnston, C.S. Arnold and D. Venus, Phys. Rev. B, in press.

218. D. Sander, A. Enders, C. Schmidthals, J. Kirschner, H.L. Johnston, C.S. Arnold, and D.Venus, to be published in J. Appl. Phys.

19. K.-P. Kämper, W. Schmitt, G. Güntherodt and H. Kuhlenbeck, Phys. Rev. B **38**, 9451, (1988).

20. Y. Li, K. Baberschke, Phys. Rev. Lett. **68**, 1208, (1992).

21. A. Berger, S. Knappmann and H.P. Oepen, J. Appl. Phys. **75**, 5598, (1994); A. Aspelmeier, M. Tischer, M. Farle, M. Russo, K. Baberschke, and D. Arvanitis, J. Magn.Magn. Mater. **146**, 256, (1995); H.-P. Oepen, S. Knappmann, W. Wulfhekel, J. Magn. Magn. Mat. **148**, 90, (1995); G. Garreau, M. Farle, E. Beaurepaire and K. Baberschke, Phys. Rev. B **55**, 330, (1997).

22. Chikazumi, *Physics of Magnetism*, (Wiley, New York, 1986), section 2.2.

23. C.S. Arnold and D. Venus, Rev. Sci. Inst. **66**, 3283, (1995); C.S. Arnold and D. Venus, to be published.

24. R. Allenspach, M. Stampioni, and A.Bischof, Phys. Rev. Lett. **65**, 3344, (1990).

25. C. Scmidthals and D. Venus, unpublished.

26. U. Gradmann, J. Korecki and G. Waller, Appl. Phys. A **39**, 101, (1986).

27. J. Arelett, J.P. Whitehead, A.B. MacIsaac, and K. De'Bell, Phys. Rev. B **54**, 3394, (1996).

28. P. Beauvillain, A. Bounouh, C. Chappert, R. Mégy, S. Ouhd-Mahfoud, J.P. Renaud, D. Weller, and J. Corms, J. Appl. Phys. **76**, 6078, (1994); F.O. Schumann, M.E. Buckley, and J.A.C. Bland, *ibid*, **76**, 6093, (1994).

4.4 Supplementary data

4.4.1 Spin reorientation at x = 3 ML

Detailed spin-reorientation measurements were made at x =2.2, near the tricritical point and at 3 ML Fe. The 3 ML data is presented here in fig. 4.10 for completeness. The data was obtained with the same experimental parameters (e.g. applied field amplitudes, time constant, modulation frequency) as for the 2.2 ML film. A few qualitative differences

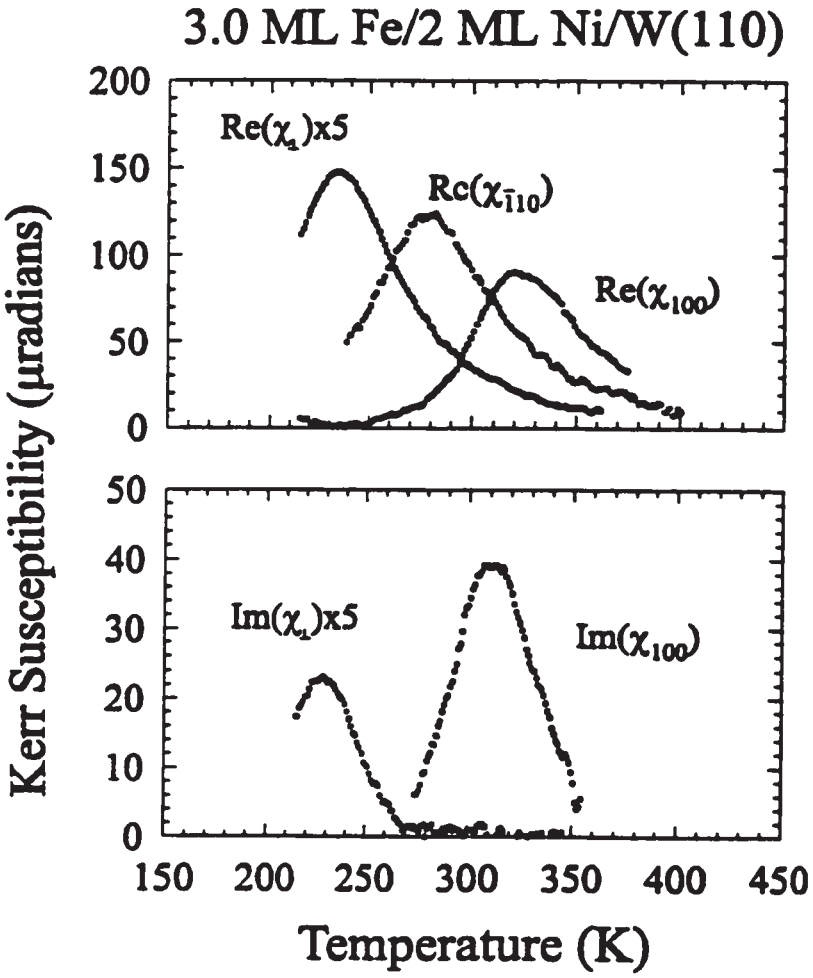

Fig. 4.10 - Spin reorientation at x = 3 ML Fe shows a few qualitative differences with that at x = 2.2 ML (fig. 4.7). One similarity is the broad, purely real signal in $\chi_{\bar{1}10}$ at intermediate temperatures.

exist between the two data sets. Firstly, the locations of the peak in Re{$\chi_\perp$}and the high temperature end of remanence in Im{$\chi_\perp$} (at 270 K) occur at lower temperatures in the x = 3 ML data than those at x = 2.2 ML. $\chi_{\bar{1}10}$ remains broad and real; the imaginary part is very small, but noisy, and is omitted from the figure. Re{χ_{001}} and Im{χ_{001}} are much broader and no longer resemble the expected form of an order/disorder transition. Re{χ_{001}} was not measured to very high temperatures, but remains much greater than zero where Im{χ_{001}} = 0. This is suggestive that the vanishing trend in Im{χ_{001}} above 300 K is not due to a coercive field that grows with increasing temperature. The loss of remanence near 350 K may be due to a loss of long range magnetic order. At this Fe coverage, the fourth layer Fe might be partially occupied, due to the uncertainty in the film thickness or perhaps non-ideal growth. The structural results of Johnston et al. show that the conversion to bcc begins with fourth layer growth.[40, 41] A change in magnetic properties starting at this thickness is therefore expected, although it is unclear how the change might manifest in the susceptibility data.

4.4.2 2 ML Fe/2 ML Ni/W(110)

The coverage x = 2 ML Fe is particularly interesting because it is the highest coverage for which no spin-reorientation is observed. Fig. 4.11 shows (a) the real parts of the susceptibility and (b) Im{ $\chi_\perp$}, obtained from a 2 ML Fe/2 ML Ni/W(110) film. Both

$Im\{\chi_{001}\}$ and $Im\{\chi_{\bar{1}10}\}$ were zero. $Re\{\chi_{\bar{1}10}\}$, noisy here because of a reduced time constant, is featureless. The imaginary part vanishes at slightly higher temperatures than the remnant point plotted on fig. 4.9. A weak, purely real peak is present in $Re\{\chi_{001}\}$

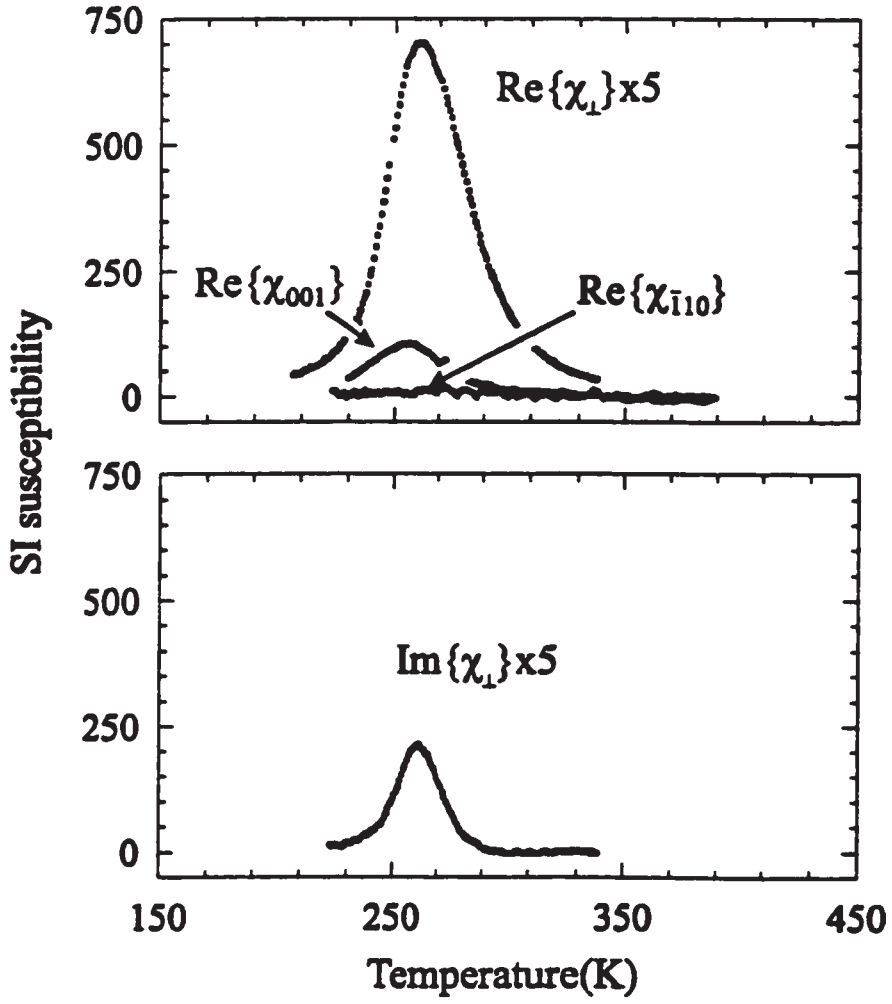

Fig. 4.11 - Data at 2 ML Fe shows evidence of the spin reorientation which occurs at slightly greater coverages (compare with fig. 4.7).

near 250 K, very similar to a feature present in the Re{ χ_{001} } data of fig. 4.7, which also showed a much larger peak at high temperatures corresponding to reorientation. This feature and the temperature of the peak in Re{ $\chi_{\perp}$ } show a continuity of behavior with the 2.2 ML data, while an abrupt reduction in magnitude of Re{ $\chi_{\perp}$ } and spin-reorientation are observed at 2.2 ML.

4.4.3 Polar hysteresis loops of an x = 2 ML Fe/2 ML Ni Film

A series of SMOKE hysteresis loops obtained for different temperatures from an *x* = 2 ML Fe/2 ML Ni/W(110) are presented in fig. 4.12 to augment the susceptibility data. The magnitudes of all of the polar susceptibility data, in rotation units, were small (< 0.25%) compared to that expected for complete magnetization reversal of perpendicularly magnetized Fe films of comparable thickness well below their Curie temperatures. SMOKE hysteresis loops were obtained with much larger fields and could saturate the film. The magnitudes of the SMOKE rotation at 215 K were 360 +/- 10 μradians, which is consistent with the expected SMOKE rotation from a saturated 2 ML bcc Fe film.[67] As the temperature of the film was increased, the saturation magnetization decreased only slightly, but the coercive field and remanent magnetization decreased dramatically. The peak of Re{ $\chi_{\perp}$ } at this coverage occurs at approximately 250 K with remanence vanishing near 260 K. The SMOKE loop at 275 K, with the saturation magnetization being much greater than the remanent value, is consistent with Re{ $\chi_{\perp}$ } >> Im{ $\chi_{\perp}$ } as observed in

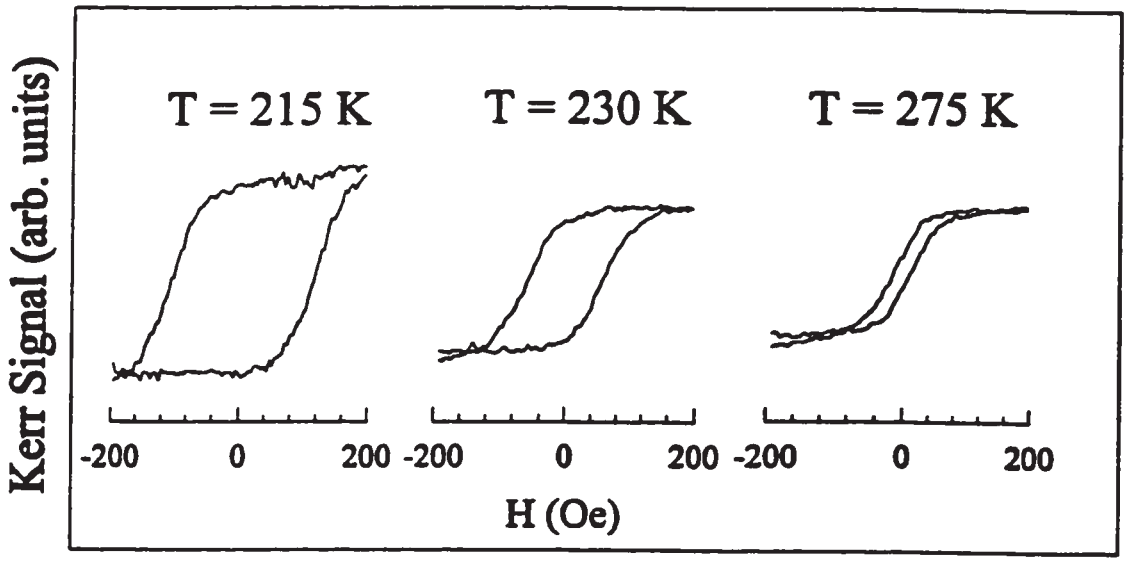

Fig. 4.12 - Polar hysteresis loops were obtained from a 2 ML Fe/2 ML Ni/W(110) film at 215 K, 230 K and 275 K. The heights of the loops are approximately 360 μradians, consistent with the saturation magnetization of 2 ML bulk Fe. Hysteresis becomes small near 275 K, consistent with the susceptibility measurements.

many susceptibility measurements. In principle, the $\arcsin(H/H_C)$ dependence of M(H) in Eq. (4.2) is testable near H_C (i.e. in the approach to saturation), where significant deviation from linearity occurs, but the S/N of fig. 4.12 is not adequate for this kind of test.[68] The loop-shapes of the data at 275 K are at least not inconsistent with measurements made by Berger et al. on stripe-domain structures, which showed the $\arcsin(H/H_C)$ dependence near H_C.[69]

4.4.4 Other examples of W($\bar{1}$10) remanence

On a few occasions substantial remanence was detected along W($\bar{1}$10) rather than W(001). In these cases the Ni substrate thickness was either marginally too thin or in error due to experimental mistakes. An example of the latter is shown in fig. 4.13 (a), for a 1.75 ML Fe film on a (dubious) 2 ML substrate. The figure shows the real and imaginary parts of the polar and W($\bar{1}$10) susceptibilities. Breaking with the convention used thus far, the polar and in-plane susceptibility data are plotted in absolute intensity units. The choice shows that the signals are very nearly the same size in rotation units. In the temperature range 280 K to 300 K, $\mathrm{Re}\{\chi_{\perp}\}$ and $\mathrm{Im}\{\chi_{\bar{1}10}\}$ are nearly equivalent. Although we can't offer an adequate explanation of this data, the very close agreement of $\mathrm{Re}\{\chi_{\perp}\}$ and $\mathrm{Im}\{\chi_{\bar{1}10}\}$ in this range seems more than coincidental. For the present purpose, we simply note that the data is anomalous and suspect the Ni substrate thickness as the reason. Fig. 4.13 (b) shows the same components for a 2.5 ML Fe/1.8 ML Ni film. $\mathrm{Im}\{\chi_{\perp}\}$ was measured only at 220 K and was zero. This purely real signal in the polar susceptibility is consistent with anisotropy contrast. The in-plane signal near 350 K is consistent with an in-plane order-disorder transition. Observations like fig. 4.13 (a) and (b), together with the ARAES and STM results, suggested that Fe/1 ML Ni was strongly in-plane, and that minority Fe/1 ML Ni patches were overpowering the majority Fe/2 ML patches because of the stronger anisotropy energy associated with the minority patches. The Fe/1 ML Ni measurements presented in sections 4.3 and 3.2.6 verified this hypothesis.

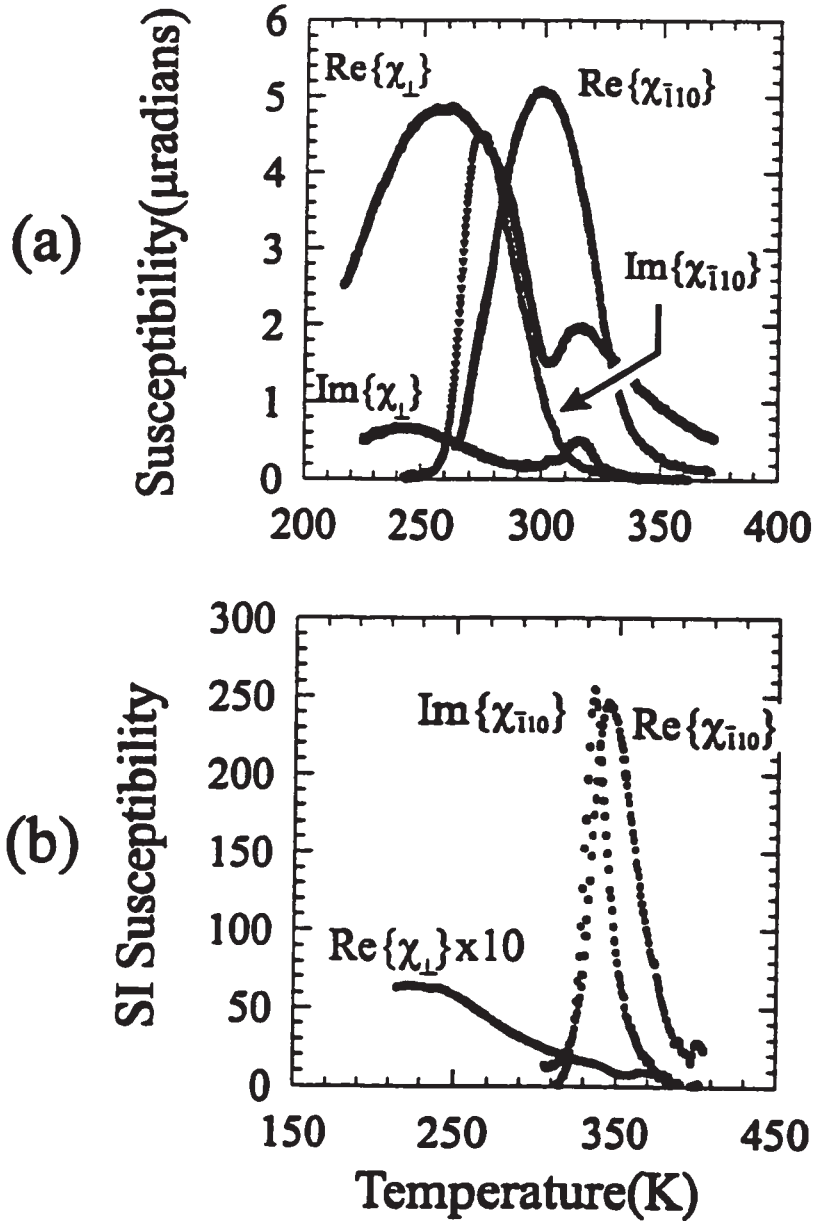

Fig. 4.13 - (a) 1.75 ML Fe grown on a Ni substrate, suspected to be less than 2 ML thick, shows perpendicular and in-plane magnetism along W(I10) coexisting in the same temperature range. An unusual feature is that polar and longitudinal SMOKE signals were nearly the same magnitude. (b) a 2.5 ML Fe film grown on a 1.8 ML Ni film behaves like an in-plane magnet, with M along W(I10) and T_C near 350 K.

4.5 Exponential decay of Re{$\chi_\perp$}

Implicit in the domain stripe model of Kashuba and Pokrovsky is the prediction that Re{$\chi_\perp$} should obey a simple exponential decrease with increasing temperature.[30] As discussed in section 4.3, Re{$\chi_\perp$} should vary with temperature according as 1/n*(T), and n*(T) depends exponentially as in Eq. (4.3) with the effective anisotropy

$$\lambda_{eff}(T) = \lambda(T) - N\,\Omega(T)/a \qquad (4.5)$$

where a is the lattice parameter, N is the number of atomic layers and $\lambda(T)$ and $\Omega(T)$ are the temperature renormalized bare anisotropy and dipolar strengths respectively. Using their expressions for the temperature dependencies, the reorientation temperature ($\lambda_{eff}(T_R) = 0$) is

$$T_R = \lambda^\circ_{eff}\, 2\pi\Gamma_\circ/\lambda_\circ\xi \qquad (4.6)$$

where $\xi = \tfrac{1}{2}\ln[\Gamma_\circ/\lambda_\circ a^2]$, $\Gamma_\circ = \Gamma(0)$, $\lambda_\circ = \lambda(0)$ and $\lambda^\circ_{eff} = \lambda_{eff}(0)$. Using the same renormalized quantities in Eq. (4.3) $n^*(T) \sim \exp-[\pi(8\Gamma(T)\lambda_{eff}(T))^{1/2}/N\Omega(T) + 1]$ and assuming $kT << \Gamma_\circ$, a simple exponential decay is obtained

$$\mathrm{Re}\{\chi_\perp\} \sim \exp(-\alpha T)\,, \qquad (4.7)$$

where

$$\alpha = \sqrt{\frac{\pi\xi}{\lambda_\circ a^2 T_R}} \qquad (4.8)$$

Using the estimated values of Abanov *et al.* for $\Gamma_\circ$, and Ωa of 480 K, and 2.6 K, and choosing T_R = 300 K for N = 2 ML determines $\lambda_\circ a^2$ via Eq. (4.6) at 6.8 K and then the decay exponent α is expected of order 0.073 K^{-1}.[35] Because T_R decreases as the

thickness (N) increases, α is expected to increase.

Most experimental $Re\{\chi_\perp\}$ decay as $\exp(-\alpha T)$ over a significant range of temperature. Fig. 4.14 is a plot of $\ln[Re\{\chi_\perp\}]$ vs. temperature for a 1.5 ML Fe/ 2 ML Ni/W(110) film. It shows a remarkably long range of temperature that $Re\{\chi_\perp\}$ decays as $\exp(-\alpha T)$. A fit to the linear portion gives $\alpha = 0.048\ K^{-1}$, in reasonable agreement with the above estimate. Interestingly, a qualitatively different behaviour is observed near the coverage of 1 ML Fe/ 2 ML Ni, where the discontinuity was observed in the approximate phase diagram of Fig. 4.9. Fig. 4.15 is a plot of $\ln[Re\{\chi_\perp\}]$ for a 1.0 ML Fe/ 2 ML Ni

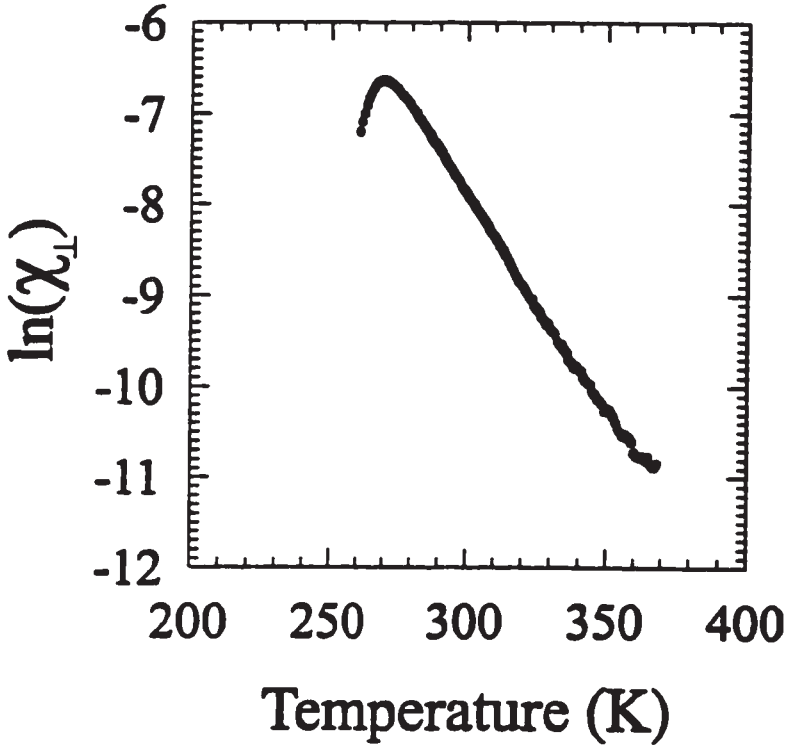

Fig. 4.14 - This 1.5 ML Fe/2 ML Ni film exhibits exponential decay over a wide range of temperature, in agreement with predictions implicit in the theoretical work of Kashuba and Pokrovsky.

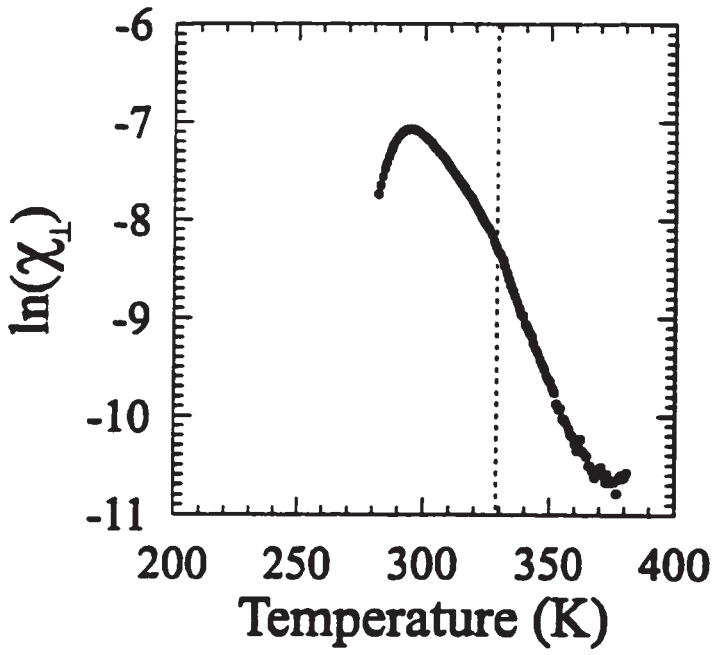

Fig. 4.15 - Films near 1 ML Fe coverage behave differently than films at other coverages, showing a change in exponential behaviour near the temperature that $\mathrm{Im}\{\chi_\perp\}$ vanishes.

film, showing a discontinuity in exponential behaviour near 330 K. For this film, 330 K is also approximately the temperature that $\mathrm{Im}\{\chi_\perp\}$ vanishes. Although all data sets at higher coverages have a non-zero imaginary part above the peak temperature of $\mathrm{Re}\{\chi_\perp\}$, this change in exponential behaviour is particular to the coverage just before the discontinuity in the phase diagram at 1 ML Fe. Fig. 4.16, summarizes the behaviour of α with increasing film thickness. As described above, α is expected to increase with increasing thickness, except for submonolayer coverages where the effective anisotropy is constant. The expectation is incorrect, as α decreases for coverages greater than 1.5 ML. The prediction may be wrong because of the assumption $kT \ll \Gamma_o$, which is a poor

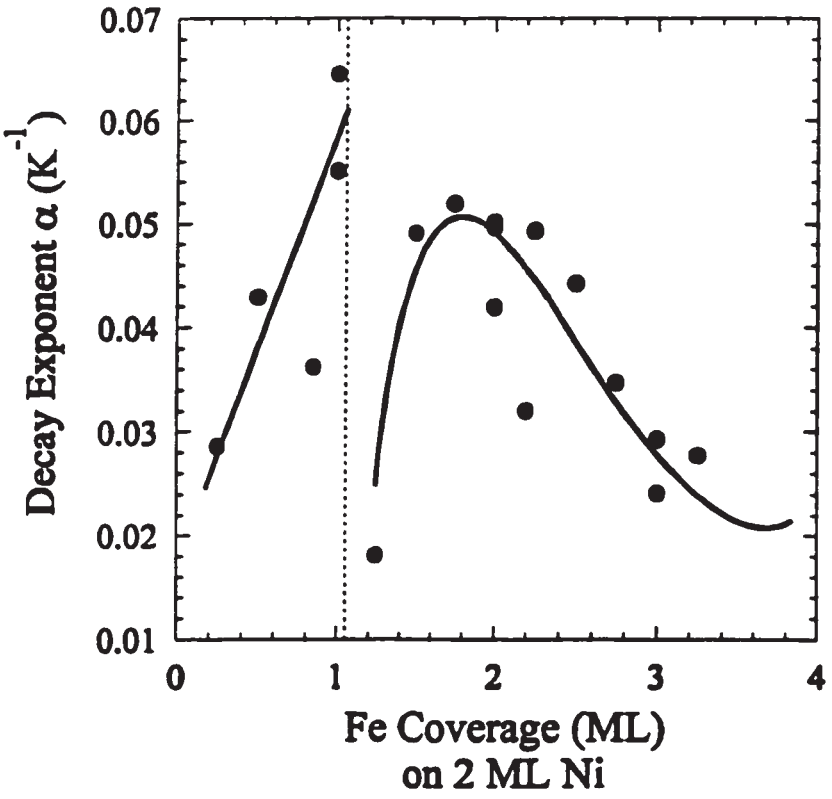

Fig. 4.16 - The decay exponent α increases in the submonolayer range and decreases for films thicker than 1.5 ML Fe.

approximation for Γ_o = 480 K.

4.6 The transition to disorder from the perpendicular phase

In this section, the possibility of a signature of the transition to disorder from the perpendicular phase is investigated in more detail. A portion of the measurement at x = 1 ML Fe/2 ML Ni of Fig. 4.5 and Fig. 4.15 is reexamined in Fig. 4.17. If a temperature T_C exists where the correlation length of critical fluctuations diverges to macroscopic length scales, then we expect $\chi_{ext} \sim 1$ because of the N = 1 demagnetization factor. Furthermore, by comparing the calculated phase diagram of Pescia and Pokrovsky[31] to the

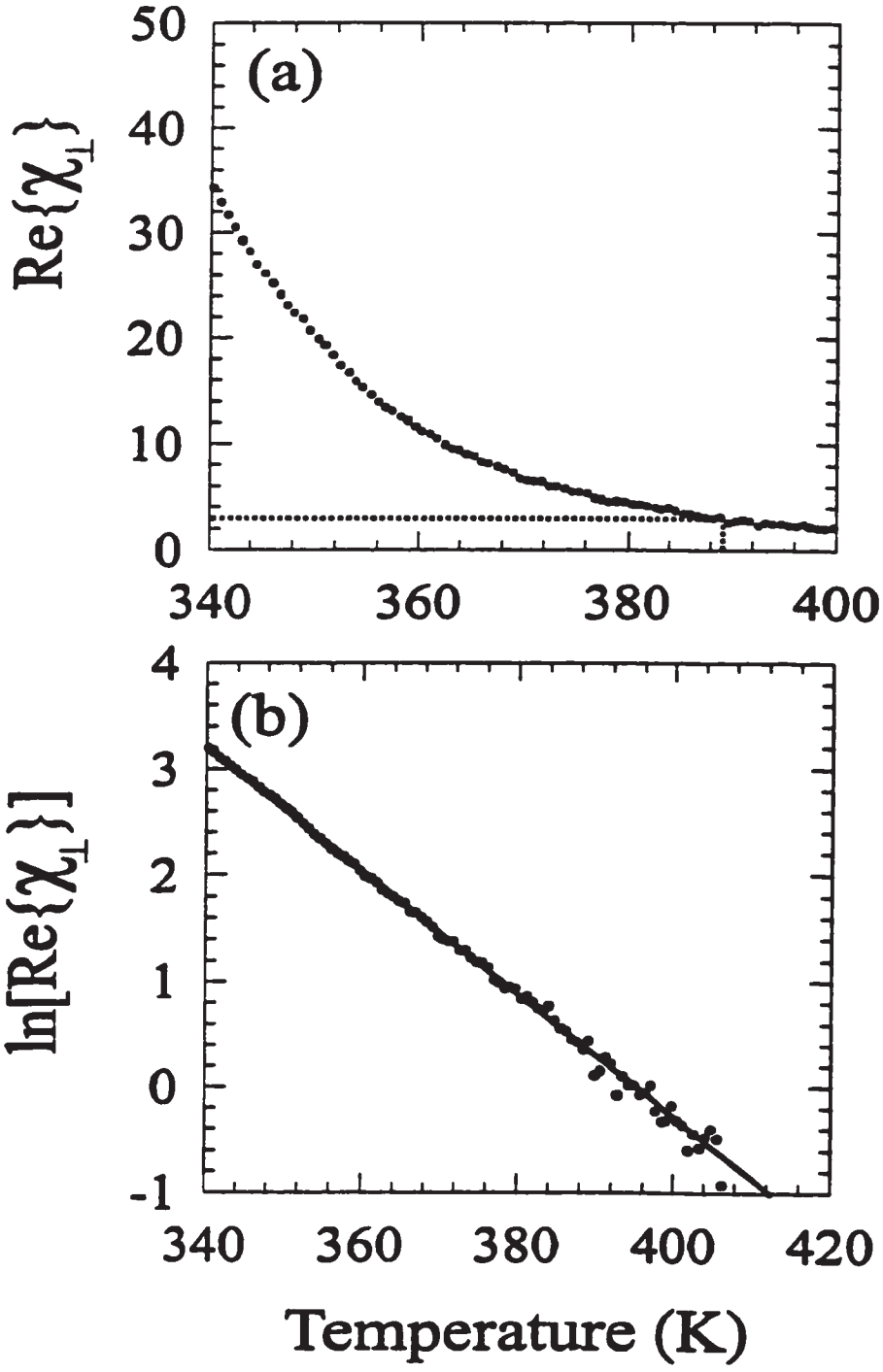

Fig. 4.17 - (a) A closer examination of the data of Fig. 4.5 and Fig. 4.15 in the range of an expected T_c reveals no evidence of this special temperature. (b) A semilog plot of the same data, which has been corrected for a small instrumental offset, shows a simple exponential decay throughout this temperature range.

schematic phase diagram of Fig. 4.9, we infer T_C must be less than 350 K for the 1 ML film of Fig. 4.17. The poor magnetic calibration is accounted for by admitting the possibility that the SI strength is out by as much as a factor of 3, *which is very unlikely*, so that $\chi_{ext} = 1 - \chi_{ext} = 3$ at T_C, in the units of Fig. 4.17. Even in the unlikely event that the calibration is that poor, $Re\{\chi_\perp\}$ remains greater than 3 until above 380 K, well above the temperature where T_C would be expected. Referring to the same data, but in the semilog plot of Fig. 4.15, a slight deviation from exponential behaviour occurs near 350 K. Hypothesizing that the deviation is due to an erroneous signal (via mechanical coupling, for example) a small constant was added to $Re\{\chi_\perp\}$ before taking the natural logarithm. An adjustment of 0.75 in SI units is sufficient to maintain linearity to beyond 400 K, as shown in on the semilog plot 4.17 (b). Magneto-mechanical coupling produces signals of this strength, when converted to the effective SI units. Of course, another possibility is that the deviation from linearity is a subtle effect of the transition to disorder, given that the size of the adjustment is of order of 1. A better quantification of the magneto-mechanical coupling is required to test this possibility. In any case, we conclude that the transition to disorder from the perpendicular phase of this film system is not characterized by a definite temperature T_C where the correlation length of critical fluctuations diverges to macroscopic length scales, as for in-plane or bulk magnets. If a related temperature exists, then the magnetic susceptibility exhibits at most a subtle signature.

The apparent absence of a T_C may be a characteristic common to all or many perpendicularly magnetized, ultrathin films which do not exhibit a spin-reorientation

transition. Monte Carlo simulations by Arlett *et al.* studied the behaviour of 2-D Ising magnets with a perpendicular orientation of the moment with both dipolar and exchange interactions.[70] Because the moments were constrained to lie perpendicular to the plane, the possibility of spin-reorientation was excluded. This situation may arise in ultrathin magnetic films with a very strong, positive perpendicular magnetic anisotropy. These simulations require a substantial computational effort, due to the large double-sums associated with the dipole field on large lattices. Although the focus of that work was the melting of the striped phase, the authors note that the transition from tetragonal liquid to paramagnetic is achieved by a continuous disintegration of the film over a broad temperature range into smaller and smaller domains. Neither a discontinuity of behaviour nor a diverging correlation length were observed at any temperature. It would be very interesting to calculate the magnetic susceptibility within a similar Monte Carlo simulation, and compare the result to the experimental polar susceptibilities presented here.

More experiments are required to study the high temperature behaviour of this and similar systems. Qiu *et al.* studied the temperature dependence of the remanent magnetization of perpendicularly magnetized Fe/Ag(100) films at coverages where no spin-reorientation occurred.[71] M(T) obeyed a universal, 2-D Ising behaviour $M(T) \propto (T_C - T)^{1/8}$ to within 10% of T_C. Remanence persisted, however, to temperatures well above (10%) the fitted value of T_C. The authors attribute the effect to finite size effects, which seems unreasonable because finite-size effects for in-plane magnets of comparable structural quality are 10 times smaller in temperature range. It would be very interesting to perform magnetic susceptibility measurements on the same system and determine

whether the persistent remanence above T_C is indeed a finite size effect, or whether there is a crossover to the liquid crystal behaviour which dominates the data presented here. Another obvious experiment is to study the remanent behaviour of the Fe/Ni(111) system. This study would require modifications of the present apparatus for the provision of larger applied fields.

4.7 The trend of the polar susceptibility magnitudes

Peak values χ_{max} for $\mathrm{Re}\{\chi_\perp\}$, obtained from many films, are plotted as the points of Fig. 4.18 and the solid line is a guide to the eye. A smoothly increasing trend is present for $x = 0$ to 1 ML. A dip occurs between $x = 1$ and 1.5 ML, as occurs in the temperature boundary of Fig. 4.9. The tremendous scatter present at 2 ML is interpreted as the uncertainty (5 to 10%) in the Fe film thickness combined with a very steep drop in the χ_{max} trend at the onset of spin reorientation. Between $x = 2$ and 3 ML Fe χ_{max} decreases very gradually. The consistency of the data in this coverage range suggests that magnitude of the susceptibility varied systematically over the whole coverage range, and that the interpretation of the scatter at $x = 2$ ML as a real feature is probably correct.

The trend of the peak value of the polar susceptibilities with coverage is similar to the boundary of Fig. 4.9 that tracks the temperatures at which the peak values occur. At present, no theory of the magnitude χ_{max} exists because none of the models include coercive field effects. The coercive field H_c scales with the effective anisotropy, which

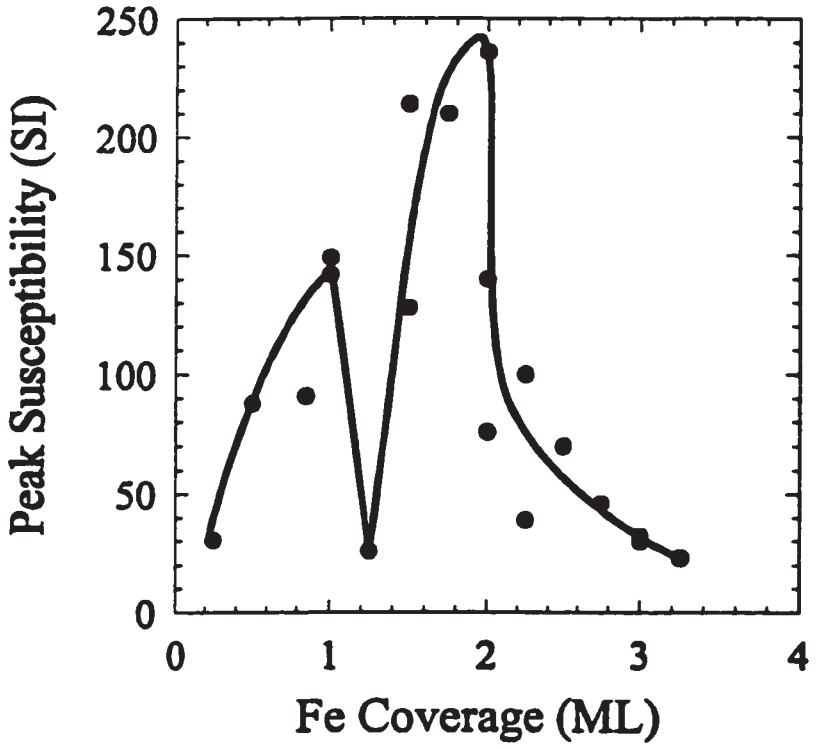

Fig. 4.18 - A summary of the observed trend in the real part of the polar susceptibility. The dots are the peak susceptibility value observed at each Fe coverage and the solid line is a guide to the eye. Discontinuities occur after 1 and 2 ML, as in the approximate phase diagram of Fig. 4.9.

increases with decreasing temperature. As the temperature is reduced H_c eventually exceeds the applied field amplitude and the exponential divergence of $\mathrm{Re}\{\chi_\perp\}$ is truncated, forming a peak in $\mathrm{Re}\{\chi_\perp\}$. The effective anisotropy, and hence H_c, also decreases as the film thickness increases from below t_R, the thickness where reorientation first occurs. Referring to figures 4.7 and 4.18, peak height χ_{max} correlates to the peak temperature of $\mathrm{Re}\{\chi_\perp\}$ through the temperature dependence of the coercive field, at least in the coverage range $x < t_R = 2.2$ ML Fe. Evidently spin-reorientation suppresses χ_{max},

as shown by the sharp discontinuity above 2 ML Fe. Whatever the detailed reason for the discontinuity at $x = 2$ ML, it seems that χ_{max} is a good marker for the onset of spin-reorientation. The abruptness of the drop at $x = 2$ ML is also evidence of good interface quality.

5. CONCLUSIONS

Magnetic measurements of ultrathin films were made via SMOKE susceptibility measurements. These measurements were permitted by refinements of the existing SMOKE technique. Extinction ratios of order 10^{-7} were routinely achieved through simple innovations in procedure. Light polarization phase shifts from optical windows were compensated by phase shifts from the substrate through a slight, but precise misalignment of the initial polarization azimuth. Also important were collimation and the use of apertures following the analyzing polarizer. Although extension of SMOKE to measuring the ac-susceptibility was straightforward in many ways, signal-to-noise optimization differed from that of dc-SMOKE because of the different relative strengths of noise sources near the modulation frequency. Many new and interesting ultrathin film phenomena await investigation with the extreme sensitivity of the SMOKE susceptibility technique.

For the first time, magnetic susceptibility measurements are reported for ultrathin films with magnetizations and applied fields perpendicular to the film plane. Ultrathin x-Fe/2 ML/ Ni(111)/W(110) possesses a perpendicular moment for coverages $x < 2.2$ ML. In this range of coverage, all polar susceptibilities exhibited greater magnitudes than could be accounted for by critical fluctuations modified by a demagnetization factor of 1. The magnitudes and temperature dependencies of the polar susceptibilities were consistent with the domain picture of Kashuba and Pokrovsky[30] in which the domain structure is very

sensitive to applied fields, and condenses and stiffens with increasing temperature. Furthermore, the susceptibilities obeyed a simple exponential decay $\exp\{-\alpha T\}$. The value of $\alpha \leq 0.05\ K^{-1}$ is in reasonable agreement with the theory of Kashuba and Pokrovsky,[30] although the expected increasing trend with increasing coverage was not observed. Instead, α decreased with increasing coverage. In those cases where the transition to disorder occurred directly from the perpendicular phase, no experimental evidence of an abrupt boundary was found, as in simulations by Arlett *et al.*[70] These measurements show that a fundamental difference exists in the order-disorder transition for this perpendicular magnet versus in-plane, ultrathin magnets. More experiments on other perpendicular magnets are required to test the possible generalization of this conclusion.

Also for the first time, a spin-reorientation transition was studied in detail near its multicritical point, on *x*-Fe/2 ML Ni(111)/W(110). Instead of studying the remanent magnetization, which is zero near the spin-reorientation transition, the magnetic susceptibility was measured using the polar and longitudinal Kerr effects. At $x = 2.2$ ML, a 50 K region of temperature was present in which the remanent magnetization was zero. In the same region of temperature, the polar susceptibility shows a real response and simple exponential decay. Above the remanent gap, the magnetization reoriented to the W(001) direction, and then appeared to undergo an order-disorder transition. Measurements at $x = 2$ ML did not show a reorientation. The measurements at $x = 2.2$ ML were therefore very near the multicritical point of the system. By tracking features of the polar and in-plane susceptibilities, a schematic temperature-coverage phase diagram was constructed. One important topological feature was that the upper bounding

temperature of the perpendicular phase reached a maximum value near the multicritical point. This was the first experimental verification of the predictions by Politi *et al.*[33] An unanticipated feature was a discontinuity in the temperature of the polar susceptibility peak after the completion of the first ML of Fe. This part of the phase diagram deserves further study. Peak values of the polar susceptibility roughly followed the topology of the temperature-coverage phase diagram. A striking difference was the abrupt drop in magnitude between 2.0 and 2.2 ML Fe, corresponding to the onset of spin-reorientation.

Imperfections in the Ni buffer layer influenced the film magnetic properties, particularly near the reorientation temperature T_R. These imperfections were incomplete patches in the second Ni monolayer. Fe grows on the 1 ML Ni patches in a different crystalline and morphological structure than on complete 2 ML Ni, with correspondingly different magnetic properties. In particular, Fe/1 ML Ni is strongly in-plane, magnetized along W($\bar{1}$10), while Fe/2 ML Ni exhibits a spin-reorientation transition from perpendicular to W(001). Though most of the film area is Fe/2 ML Ni, the minority Fe/1 ML Ni patches may influence or even dominate the magnetic anisotropy of the whole film as the anisotropy of the Fe/2 ML regions vanishes.

GENERAL REFERENCES

1. Compilation by J. G. Gay and R. Richter, in *Ultrathin Magnetic Structures II*, ed. by B. Heinrich, J. A. C. Bland (Springer Verlag, Berlin, 1991).

2. N.D. Mermin , and H. Wagner, *Phys. Rev. Lett.* **17**, 1133(1966).

3. H.J. Elmers, J. Hauschild, H. Hoche, U. Gradmann, H. Bethge, D. Heuer, and U. Kohler, *Phys. Rev. B* **73**, 898(1994); J.A.C. Bland, G. A. Gehring, B. Kaplan and C. Daboo , *J. Magn. Magn. Mat.* **113**, 173(1992); Z.Q. Qiu, J. Pearson, and S.D. Bader, *Phys. Rev. B* **49**, 8797(1994).

4. Michael Plischke, Birger Bergersen, *Equilibrium Statistical Physics*, (Prentice Hall, New Jersey, 1989).

5. Takahito Kaneyoshi, *Introduction to Surface Magnetism*, (CRC Press, Boca Raton FL, 1991).

6. Ni may differ from Fe and Co. See C. Herring in *Magnetism* **4**, ed. by G. T. Rado and H. Suhl (Academic Press, New York, 1966).

7. E.C. Stoner, *Rept. Prog. Phys.* **11**, 43(1947).

8. H. Bethe, *Handb. d. Physik* **24**, 595(1933); J. C. Slater, *Phys. Rev.* **36**, 57(1930).

9. S. Chikazumi, *Physics of Magnetism*, (John Wiley & Sons, New York, 1964).

10. Edmund C. Stoner, *Phil. Mag.* **36**, 803(1945).

11. Y. Yafet, and E.M. Gyorgy, *Phys. Rev. B* **38**, 9145(1988).

12. C. Rau, *Phys. Lett. A* **135** 227(1989).

13. G. Fabricius, and H. Dreysse, *J. Phys. Condensed Matter* **5**, A197(1993).

14. D. L. Mills in *Ultrathin Magnetic Structures I*, ed. by B. Heinrich, J. A. C. Bland (Springer Verlag, Berlin, 1991).

15. C. Kittel, *Introduction to Solid State Physics*, 6th ed. (John Wiley & Sons Inc, New York, 1986).

16. R. P. Erickson, and D.L. Mills, *Phys. Rev. B* **43**, 11527(1990); J.A.C. Bland, G. A. Gehring, B. Kaplan and C. Daboo , *J. Magn. Magn. Mat.* **113**, 173(1992).

17. B. Heinrich, S.T. Purcell, J.R. Dutcher, K.B. Urquart, J.F. Cochran, and A.S. Arrot, *Phys. Rev. B* **38**, 12879(1988).

18. D. J. Thouless in the New Physics, ed. by P. Davies (Cambridge U. Press, Cambridge, 1989).

19. F. Huang, G.J. Mankey, M.T. Kief, and R.F. Willis, *J. Appl. Phys.* **73**, 6760(1993); F. Huang, M.T. Kief, G.J. Mankey, and R.F. Willis, *Phys. Rev. B* **49**, 3962(1994); Michael E. Fisher, Michael N. Barber, *Phys. Rev. Lett.* **28**, 1516(1972).

20. Yi Li, and K. Babershke, *Phys. Rev. Lett.* **68**, 1208(1991).

21. H.J. Elmers, J. Hauschild, H. Hoche, U. Gradmann, H. Bethge, D. Heuer, and U. Kohler, *Phys. Rev. B* **73**, 898(1994).

22. L. Neel, *J. Phys. Radium* **15**, 225(1954).

23. U. Gradmann and J. Muller, *Phys. Stat. Sol.* **27**, 313 (1968). See also N. C. Koon et al., *Phys. Rev. Lett.* **59**, 2463(1987); M. Stampononi et al. *Phys. Rev. Lett.* **59**, 2483(1987).

24. S. Chikazumi, *Physics of Magnetism*, 128 (John Wiley & Sons, New York, 1964).

25. *ibid*, section 11.2.

26. Y. Yafet, and E. M. Gyorgy, *Phys. Rev. B* **38**, 9145(1988).

27. See, for example, W.J.M. de Jonge, P.J.H. Bloemen and F.J.A. den Broeder in *Ultrathin Magnetic Structures I*, ed. by B. Heinrich, J. A. C. Bland (Springer Verlag, Berlin, 1991).

28. R. P. Erickson, and D. L. Mills, *Phys. Rev. B* **46**, 861(1992).

29. H. Fritzsche, J. Kohlhepp, H. J. Elmers, and U. Gradmann, *Phys. Rev. B* **45**, 15665(1994).

30. A. B. Kashuba, and V. L. Pokrovsky, *Phys. Rev. B* **48**, 10335(1993).

31. D. Pescia, and V. L. Pokrovsky, *Phys. Rev. Lett.* **65**, 2599(1990).

32. K. De'Bell, *private communication.*

33. P. Politi, A. Rettori, M. G. Pini, and D. Pescia, *J. Magn. Magn. Mater.* **140-144**, 647(1995).

34. Z. Q. Qiu, J. Pearson, and S. D. Bader, *Phys. Rev. Lett.* **70**, 1006(1993).

35. A. Abanov, V. Kalatsky, V. L. Pokrovsky, and W. M. Saslow, *Phys. Rev. B* **51**, 1023(1995).

36. K. De'Bell, *private communication*. B. Gaulin, *private communication*.

37. D. P. Pappas, K. -P. Kamper, and H. Hopster, *Phys. Rev. Lett.* **64**, 3179(1990); D. P. Pappas, C. R. Brundle and H. Hopster, *Phys. Rev. B* **45**, 8169(1992).

38. A. Berger, H. Hopster, *Phys. Rev. Lett.* **73**, 193(1994).

39. Andrew Zangwill, *Physics at Surfaces*, (Cambridge University Press, Cambridge, 1988).

40. H. L. Johnston, *Ph. D. Thesis*, (McMaster, 1997).

41. H. L. Johnston, C. S. Arnold and D. Venus, *Phys. Rev. B*, in Press.

42. D. Sander, A. Enders, C. Schmidthals, J. Kirschner, H. L. Johnston, C. S. Arnold, and D. Venus, *J. Appl. Phys.*, in Press

43. D. Venus, *Rev. Sci. Instrum.* **62**, 1361(1991).

44. See Andrew Zangwill, *Physics at Surfaces*, 175 (Cambridge University Press, Cambridge, 1988). Activation barriers for diffusion are of order 0.1-1eV, whereas exchange energies per atom pair are typically 10 μeV.

45. M. van Hove, *Low Energy Electron Diffraction*, (Springer-Verlag, Berlin, 1986).

46. C. Argile, and G.E. Rhead, *Surf. Sci. Rep.* **10**, 277(1989).

47. W. F. Egelhoff Jr. in *Ultrathin Magnetic Structures I*, ed. by B. Heinrich, J. A. C. Bland (Springer-Verlag, Berlin, 1991).

48. M. P. Seah, *Surf. Sci.* **17**, 132(1969).

49. Byron G. Johnson, Paul J. Berlowitz, D. Wayne Goodman, and Calvin H. Bartholomew, *Surf. Sci.* **217**, 13(1989); J. G. Ociepa, Peter J. Schultz, K. Griffiths, and P. R. Norton, *Surf. Sci.* **225**, 281(1990).

50. J. Kolaczkiewicz, and E. Bauer, *Surf. Sci.* **144**, 495(1984).

51. Jan H. van der Merwe, E. Bauer, D. L. Tonsing, and P. M. Stoop, *Phys. Rev. B* **49**, 2127(1994). E. Bauer, Jan H. van der Merwe, Phys. Rev. B **33**, 3657(1996).

52. G. Binnig, and G. Rohrer, *IBM journal of Research and Development* **30**, 355-69(1986).

53. See S. D. Bader and J. L. *Erskine in Ultrathin Magnetic Structures II*, ed. by B. Heinrich, J. A. C. Bland (Springer-Verlag, Berlin, 1991).

54. P. Bruno, Y. Suzuki, and C. Chappert, *Phys. Rev. B* 53, 9214(1996). Petros N. Argyres, *Phys. Rev.* **97**, 334(1955).

55. D. Weller, J. Sticht, G.R. Harp, R. F. C. Farrow, R. F. Marks, and H. Brandle, *Mat. Res. Soc. Symp.Proc.* **313**, 501(1993). Tetuya Kusabe, Kentaro Kyuno, and Setsuro Asano, *J. Magn. Magn. Mater.* **126**, 535(1993).

56. J. Zak, E. R. Moog, C. Liu and S. D. Bader, *J. Magn. Magn. Mater.* **88**, L261(1990). C.C. Robinson, *J. Opt. Soc. Am.* **54**, 1220(1964).

57. E. R. Moog and S. D. Bader, *Superlattices and Microstructures* **1**, 543(1985)

58. A. Aspelmeier, M. Tischer, M. Farle, M. Russo, K. Baberschke, and D. Arvanitis, *J. Magn. Magn. Mater.* **146**, 256(1995).

59. A detailed magneto-optic calculation involving the three layers of the Fe/Ni/W is possible, but was not attempted. This calculation would require the assumption of a Voigt parameter of fcc Fe.

60. Ernesto J. Escorcia-Aparicio, R. K. Kawakami, and Z. Q. Qiu, *J. Appl. Phys.* **79**, 4964(1996). J. Thomassen, F. May, B. Feldmann, M. Wuttig, and H. Ibach, *Phys. Rev. Lett.* **69**, 3831(1992).

61. Obtained by C. Schmidthals and printed here with his permission.

62. U. Gradmann, G. Waller, *Surf. Sci.* **116**, 539(1982).

63. Between different charges of the Fe evaporator, a 5% change in calibration was often observed.

64. G. Garreau, E. Beaurepaire, K. Ounadjela, and M. Farle, *Phys. Rev. B* **53**, 1083(1996).

65. G. Garreau, M. Farle, E. Beaurepaire, and K. Babershke, *Phys. Rev. B* **55**, 330(1997). H. P. Oepen, S. Knappmann, W. Wulfhekel, *J. Magn. Magn. Mat.* **148**, 90(1995).

66. The highest T_C for a 1 ML film that the author is aware of from ref. 65, 1 ML hcp cobalt has a T_C of 400 K. Compare this with 1 ML Fe/W(110) (ref. 21) which has a T_C of 220 K. Better arguments for the value of T_C are provided in sections 2.3 and 2.6.

67. For bcc Fe/Ag see E. R. Moog, C. Liu, S. D. Bader and J. Zak, *Phys. Rev. B* **39**, 6949(1989); S. D. Bader, Dongqi Li, and Z. Qiu, *J. Appl. Phys.* **76**, 1994(6419). For Co/Ni(111), see M. T. Johnson, F. J. A. den Broeder, J. J. de Vries, N. W. E McGee, R. Jungblut, and J. ann de Stegge, *J. Magn. Magn. Mater.* **121**, 494(1993).

68. Despite the enormous polar signal obtained from the 2 ML Fe film sample, the cooling apparatus introduces vibrations into the sample holder arm, producing the observed noise. Signal averaging over several loops would easily resolve this problem, but the *in situ* magnet coils start to overheat and outgas after only one. This is very destructive to the film.

69. A. Berger, and H. Hopster, *J. Appl. Phys.* **79**, 5619(1996); A. Berger, and H. Hopster, *Phys. Rev. Lett.* **76**, 1996(1996).

70. J. Arlett, J. P. Whitehead, A. B. MacIsaac, and K. De'Bell, *Phys. Rev. B* **54**, 3394(1996).

71. Z. Q. Qiu, J. Pearson, and S. D. Bader, *Phys. Rev. B* **49**, 8797(1994).

72. A. M. Polykov, *Phys. Lett. B* **59**, 79(1975).

73. R. Allenspach, and A. Bischof, *Phys. Rev. Lett.* **69**, 3385(1992).

74. U. Gradmann and G. Waller, Surf. Sci. **116**, 539 (1982).

IMAGE EVALUATION
TEST TARGET (QA-3)

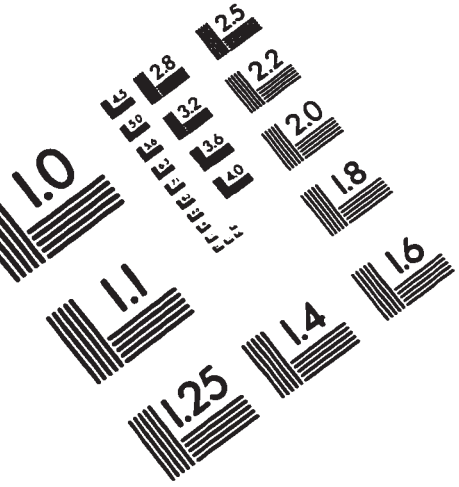

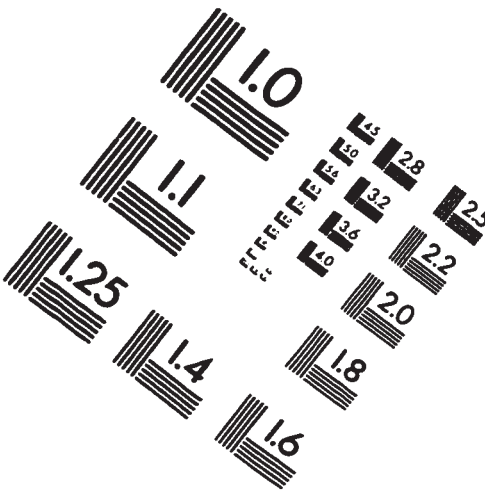

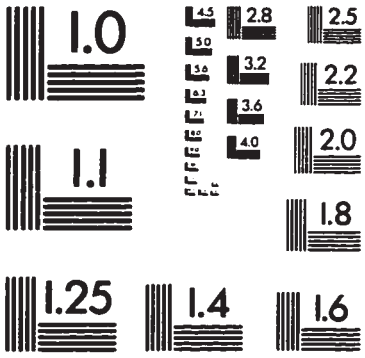

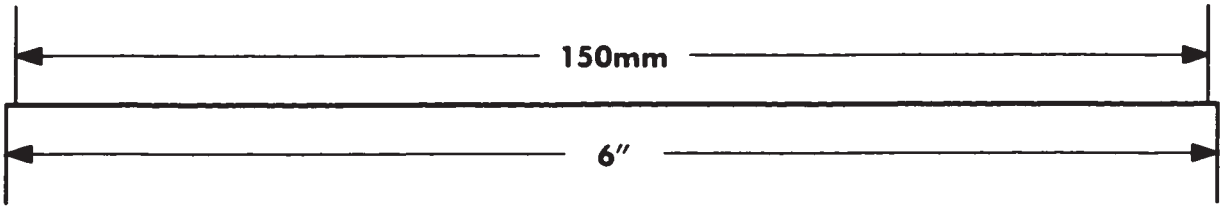

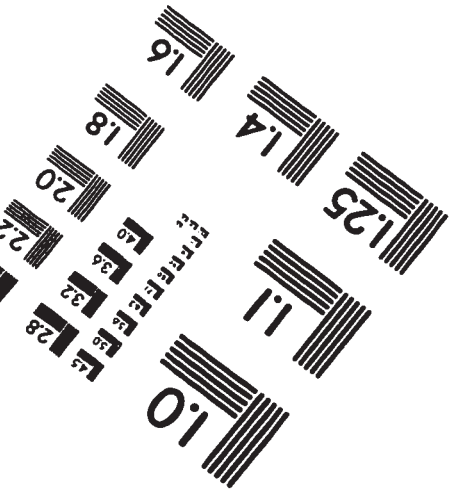

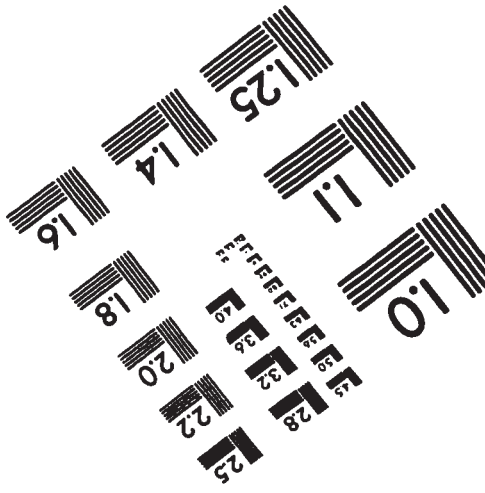

APPLIED IMAGE, Inc
1653 East Main Street
Rochester, NY 14609 USA
Phone: 716/482-0300
Fax: 716/288-5989